Improvement of Consistency, Accuracy and Interpretation of Characterisation Test Techniques for Li-ion Battery cells for Automotive Application

By

Anup Barai

A thesis submitted in partial fulfilment of the requirements for the degree of

Doctor of Philosophy in Engineering

University of Warwick, Warwick Manufacturing Group (WMG)

November 2015

Contents

List of Figures

List of Tables

Acknowledgement

The research would not have been as fascinating without the remarkable people I was introduced with along the journey. First and foremost I would like to thank my supervisors, Professor Paul Jennings and Dr. Andrew McGordon for their guidance, support, trust and 'the freedom to create'. I am indeed fortunate to have Professor Paul Jennings to supervise me about overall research, its progression and presentation. To have Dr. Andrew McGordon to guide me is a privilege not only in this doctoral experience but beyond that as well. With his technical knowledge and quick response he has been invaluable. I feel incredible and it is an honour to work with them.

I would like to thank Dr. Yue Guo, Mr. Mark Amor-Segan, Dr. Gael Chouchelamane, Dr. Chris Lyness, Dr. Kotub Uddin, Dr. James Marco and Dr. W. Dhammika Widanage for brainstorming discussions, guidance and support they provided for writing journal and conference papers.

I am thankful to other colleagues Mr. Gunwant Dhadyalla, Mr. Andrew Moore, Mr Terry Timms, Mr. John Palmer, Mr. Limhi Somerville, Mr. Sina Shojaei, Dr. Ravichandra Tangirala, Dr. James Taylor for their valuable discussion and support. I am grateful to Dr. Hillol Roy, Dr. Brahmadevan Venniyod Padma Rajan, Dr. James Mackrill, Mr. Abhishek Das, Mr. Arnab Palit for sharing their PhD experience. I will certainly have fond memories of the leisurely chats we had.

Special thanks to Rakib Raihan, Intekhab Alam, Rabeya Akther, Tapos Barai and Ayan Tarafder for their unconditional support and to give me their time when there was no lab work to do or read any research article.

I am thankful to WMG, University of Warwick for financial support, without that the journey was not possible.

My deepest appreciation goes to my parents, brother, uncles, aunties, cousins, sister in-law, parents-in law and grandparents. A special thanks to my Ma to keep me on track in all my ventures. Finally I would like to thank my wife for her patience with me during the long evening hours spent at office, encouragement, endless love, and support.

Declaration

This thesis is presented in accordance with the regulations for the degree of Doctorate of Philosophy. It has been written and complied by myself and has not been submitted anywhere else. The work in this thesis has been undertaken by me except where otherwise stated.

Signed: Date:

Anup Barai

List of Publications

Journal Publications

A. Barai, K. Uddin, W.D. Widanalage, A. McGordon and P. Jennings, “The effect of immediate cycling history on total energy of lithium-ion batteries for electric vehicles” Journal of Power Sources, 2016. 303(0): p. 81-85.

A. Barai, W. Dhammika Widanage, J. Marco, A. McGordon and P. Jennings, “A study of the open circuit voltage characterisation technique and hysteresis assessment of lithium-ion cells”, Journal of Power Sources, 2015. 295(0): p. 99-107.

A. Barai, G. H. Chouchelamane, Y. Guo, A. McGordon and P. Jennings, “A study on the impact of lithium-ion cell relaxation on electrochemical impedance spectroscopy” Journal of Power Sources, 2015. 280(0): p. 74-80.

A. Barai, G. H. Chouchelamane, A. McGordon and P. Jennings, “Impact of lithium-ion cell relaxation on electrical impedance spectroscopy – effect of SoC, temperature and discharge C-rate” Draft version, will be submitted in relevant journal.

Conference Proceedings

A. Barai, A. McGordon and P. Jennings, “A study of the effect of short-term relaxation on the EIS test technique for EV battery cells” International Workshop on Impedance Spectroscopy, Chemnitz, Germany, 23-25 September 2015.

A. Barai, Y. Guo, A. McGordon and P. Jennings, “An exploration of Li-ion cell relaxation using EIS” FISITA World Automotive Congress, Maastricht, Netherlands, 2-6 Jun 2014.

A. Barai, Y. Guo, A. McGordon and P. Jennings, “A study of the effects of external pressure on the electrical performance of a lithium-ion pouch cell” Connected Vehicles and Expo (ICCVE), 2013 International Conference on , pp.295-299, 2-6 Dec. 2013.

A. Barai, W. Dhammika Widanage, J. Marco, A. McGordon and P. Jennings, “The influence of temperature and charge/discharge rate on open circuit voltage hysteresis of Li-ion battery” Submitted: IEEE Transportation Electrification Conference, Detroit USA, 27-29 June 2016.

Abstract

Equivalent circuit models (ECM) are required to provide an on-board model of battery behaviour by battery management systems (BMS). The performance of ECMs is dependent on characterisation test results. The components of the ECM are commonly parameterised using electrochemical impedance spectroscopy (EIS) results, open circuit voltage (OCV) test results, and capacity test results. Therefore, these three tests are important for ECM parameterisation. Although the test procedures for these characterisation tests exist to test Li-ion cells for a range of applications e.g. portable electronic devices, they fail to provide essential information for automotive application due to the different requirements of vehicles (e.g. high power and energy, wide operating environment, long service life). This thesis reports research to improve consistency, accuracy and interpretation of characterisation test techniques for Li-ion battery cells for automotive application.

The capacity of the battery pack is a vital parameter required for an ECM to estimate driving range. Existing techniques for predicting the driving range of an electric vehicle use the capacity value in Amp-hours, measured by existing capacity test techniques. In this thesis, experimental evidence that establishes the advantages of using capacity in Watt-hours instead of the capacity in Amp-hours as per the standard test is presented for the first time. Moreover, it is reported that measured battery capacity can vary by up to 5.0 % depending on the length of intermediate rest period.

The OCV is another crucial parameter of ECM. The path dependence of OCV is a distinctive characteristic of Li-ion batteries which is known as OCV hysteresis. OCV test procedures used previously do not consider the initial conditions of the cells and capacity variations that show a change in OCV, leading to an apparent increase in, or erroneous, hysteresis. Using a new methodology which addresses issues mentioned above, OCV and OCV hysteresis has been quantified for different Li-ion cells for the first time. The test results show that a battery's OCV is directly related to the discharge capacity, not the more commonly used SoC. The maximum hysteresis was found in a $LiFePO_4$ (LFP) cell and lowest in a LTO cell, although still measurable. A dynamic hysteresis model is used to show how better OCV prediction accuracy can be achieved by a BMS when hysteresis voltage is a function of SoC instead of assuming it to be a constant, as traditionally done.

EIS is commonly used to parameterise an ECM. For the first time this thesis reports that the time period between the removal of an electrical load and an EIS measurement affects the results. The study of five commercially available cells of varying capacities and electrode chemistries show that, regardless of the cell type, the maximum impedance change takes place within the first 4 hours of the relaxation period. Therefore a standardised relaxation period of minimum 4 hours should be allowed before performing EIS test. In addition to ECM parameterisation, EIS has been considered for online measurement, integrated with a BMS. This thesis concluded that the use of EIS as a fast measurement tool will be unreliable because of the relaxation effect.

The flaws with capacity, EIS and OCV tests for automotive applications have been discussed. Through experimental evidence and electrochemical explanation it has been demonstrated that these tests can be made more consistent (e.g. by allowing fixed relaxation period in EIS test), have improved accuracy (e.g. incorporating hysteresis as a function of SoC) and better interpretation of test results (e.g. Watt-hours instead of Amp-hours in capacity test) are possible. Therefore, the overall contributions of this thesis to the scientific community are better consistency, accuracy and interpretation of these three tests. With the use of a case study, it has been shown that this new knowledge will improve performance of ECM, and thus BMS. This is not only for automotive but also more general applications through adopting the proposed new methodologies.

Abbreviations

AC	Alternating Current
BEV	Battery Electric Vehicle
BMS	Battery Management System
CAFE	Corporate Average Fuel Economy
CC	Constant current
CO_2	Carbon-di-Oxide
CPE	Constant Phase Element
CV	Constant Voltage
DCR	Direct Current Resistance
DEC	Diethyl Carbonate
DMC	Dimethyl Carbonate
DoD	Depth of Discharge
DoE	Department of Energy
EC	Ethylene Carbonate
ECM	Equivalent Circuit Model
EIS	Electrical Impedance Spectroscopy
EMC	Ethyl Methyl Carbonate
EoL	End of Life
EV	Electric Vehicle
FBE	Full Battery Energy
HEV	Hybrid Electric Vehicle
HPPC	Hybrid Pulse Power Characterisation
ICE	Internal Combustion Engine

IEC	International Electrochemical Commission
ISO	International Standardisation Organization
LCO	Lithium Cobalt Oxide
LFP	Lithium Iron Phosphate
LMO	Lithium Manganese Oxide
LTO	Lithium Titanate Oxide
MW	Mega Watt
NMC	Lithium - Nickel Manganese Cobalt
Ni-Cd	Nickel-Cadmium
Ni-MH	Nickel-Metal-Hydride
OCV	Open Circuit Voltage
ODE	Ordinary Differential Equation
OEM	Original Equipment Manufacturer
PC	Propylene Carbonate
PPC	Pulse Power Characterisation
RBE	Remaining Battery Energy
RDR	Remaining Driving Range
PHEV	Plug-in Hybrid Electric Vehicle
SAC	Standardisation Organization of China
SEI	Solid Electrolyte Interface
SoC	State of Charge
SoE	Sate of Energy
SoH	State of Health
UPS	Uninterruptable Power Supply
USABC	United States Automotive Battery Consortium

1. Introduction

One of the main challenges to success of electric vehicles is having the correct energy storage system. Since their introduction, lithium-ion (li-ion) secondary batteries are of great interest as an energy storage solution for electric vehicles. The primary challenge in design of a Li-ion battery pack for electric vehicles is understanding Li-ion cell behaviour. Characterisation tests provide insight into the behaviour of the cell. However, these characterisation tests have received little attention from an automotive perspective. This thesis addresses the issues with existing characterisation tests in a systematic manner. To begin, this chapter provides an introduction to the applied research of characterisation test techniques for Li-ion battery cells in an automotive context.

1.1 An introduction to the recent trends in the automotive industry

Technological advancement and increase in comfort of living in past two centuries have been largely derived from exploitation of non-renewable fossil fuel. The fossil fuel like coal, natural gas, oil is created over millions of years, and we are on the course of consuming these within hundreds of years. Burning fossil fuel creates CO_2 which largely contributes to the warm-up our planet Earth [1, 2]. Although, medium to long term implication of burning these fossil fuels and CO_2 emission on our warming planet is not clear yet, however, it is decisively clear that the scientific community, government bodies and general public are attempting to reduce CO_2 emission levels.

A large portion of global CO_2 emission is generated by transport system; which is mainly dominated by road transport system [1]. Therefore, to reduce CO_2 emission level by road transport system, different legislative authorities set the global CO_2 emission fleet average targets to OEMs [3, 4]. These targets are a key driver for the recent trend in automotive industry (vehicles with reduced CO_2 emission level). The European Union passed legislation in April 2009 targeting to reach average fleet CO_2 emission of 95 grams per kilometre by 2020 [4]. In the United States, the Corporate Average Fuel Economy (CAFE), standards sets a target to OEMs of passenger cars and light trucks to achieve an average fuel economy of 6.75 litres per 100 kilometres (42 mpg, approximately 150 grams per kilometre) by 2020 [5]. Other countries such as China are also imposing environmental regulations to the automotive OEMs. Heavy fines are imposed on OEMs who fails to show progress to comply with the regulation.

To meet the target CO_2 emission level, introduction of vehicles with smaller internal combustion engine (ICE) size can be an option to OEMs. Smaller engine size typically has lower CO_2 emission level. It can offset higher end premium vehicles with higher CO_2 emission level. One good example of use of reduced engine size is 'Volkswagen Golf Mk7' which is gone through a significant reduction of engine size compared to previous models (e.g. Mk 4 or earlier). However, only reduction of the engine size is not an option for OEMs when minimum performance cannot be compromised (e.g. premium vehicle manufacturers). In addition, future CO_2 emission targets are likely to be more stringent, potentially requiring other solutions.

One solution to meet the CO_2 emission target without compromising power capability of the vehicle is to introduce an electric powertrain to the vehicle [6]. Hybridisation of conventional powertrain (ICE) with electric powertrain allows use of smaller engine size whilst maintaining power capability of the vehicle. All-electric vehicles with 0 gram per kilometre can dramatically improve fleet average CO_2 emissions.

Even before these legislations were imposed, OEMs were trying to increase fuel efficiency of their vehicles further, and hence, introduce electric powertrain. It was mainly derived by the continuous increase in oil price since 1970s [7]. Several classes of electric vehicles (EV) (hybrid electric vehicle (HEV), plug-in hybrid electric vehicle (PHEV), battery electric vehicle (BEV) etc.) have since been developed and co-exist as an integral part of OEM respective fleets. These vehicles are now slowly increasing their market share thanks to the likes of the Nissan LEAF, GM Volt, Toyota Prius and Tesla model S [8].

1.2 An introduction to EV operation

The basic operation of an electric powertrain is shown in Figure 1. A BEV is powered by an electric motor instead of a gasoline engine. Electric energy is delivered to motor from the controller and controller receives energy from battery pack installed in the vehicle. One advantage of having a motor is, it can work as a generator during slowing down or stopping a vehicle i.e. when brake pedal of a vehicle is used, recovering kinetic energy of the vehicle. This energy recovery mechanism is known as regenerative breaking and not possible in ICE vehicle.

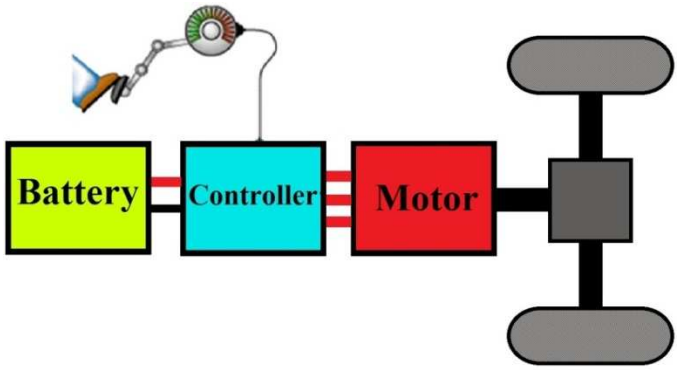

Figure 1: Basic operation of electric powertrain of BEV.

In a pure EV (BEV) vehicle only electric powertrain is used and vehicle movement is created solely by electric power supplied by battery as shown in Figure 1. In a hybrid electric vehicle (HEV), the electric powertrain works alongside the ICE powertrain. There are different complex mechanisms how two different powertrains work in a hybrid vehicle; which mainly grouped as parallel hybrid and series hybrid.

In a parallel hybrid vehicle a downsized ICE works alongside an electric motor, which is powered by battery pack. Figure 2 shows basic block diagram of the parallel hybrid vehicle. The ICE and the motor are independently connected to the transmission and can move the vehicle independently. This setup allows using either system in an operating condition, whichever is most efficient, i.e. motor at lower speed and ICE at higher speed.

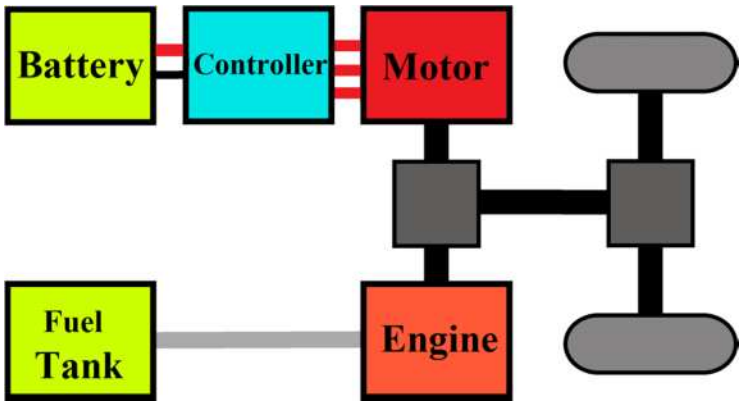

Figure 2: Basic operation of a parallel hybrid powertrain.

In a series hybrid vehicle both powertrains are connected in a single line like series connection as shown in Figure 3. In this setup only electric motor drives the vehicle. A downsized ICE is used exclusively for electricity generation when battery pack is close to fully discharged. The electricity is used either to power the motor or charge the battery. In this setup the ICE can operate at maximum efficiency region, since it is decoupled from the vehicle demand.

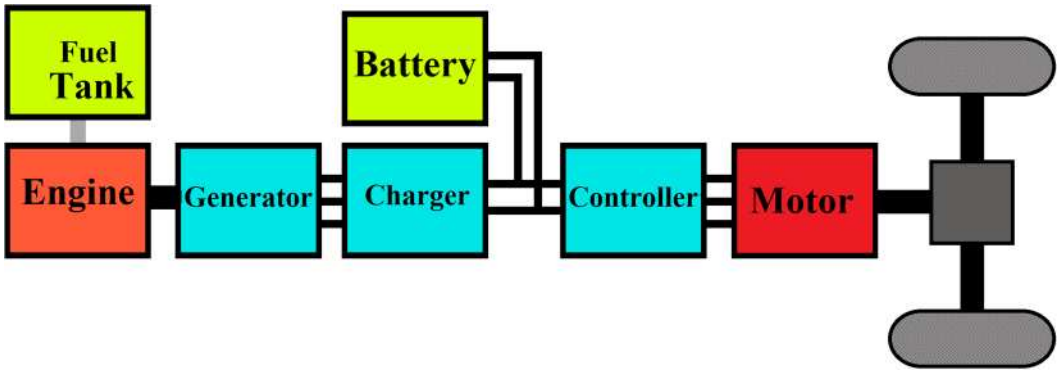

Figure 3: Basic operation of a series hybrid powertrain.

In these EV powertrain arrangements the vehicle moves or can move solely by motor, which helps to reduce CO_2 emission level. The motor gets its electricity supply mainly from battery. A key component of the electrified powertrain is the

battery, which at the advent of hybrid and electric vehicle was relatively little studied.

1.3 An introduction to EV battery

1.3.1 EV requirements from battery

EVs need a minimum power capability to accelerate to and maintain its maximum speed. They also need minimum energy storage system for its maximum driving range. These two characteristics are commonly known as power and range capability of a vehicle. Respectively, for internal combustion engine (ICE) vehicles, power capability depends on the engine size and range depends on the size of the gasoline tank. On the other hand, for EV, not only range but also power capability is directly related to the battery pack. Maximum power can be delivered from battery to motor, and range depends on battery technology and capacity of the battery pack. Moreover, EVs are expected to have similar lifetime and operate at similar climatic conditions as ICE vehicles. Thus, batteries need to be rechargeable with higher cycle life (number of times battery can be charged and discharged from 0% to 100%) and wide operating temperature range. Also, recharge capability at higher rate is desirable to capture regenerative braking energy [9].

1.3.2 Battery chemistries

From OEMs to user it is expected that new generation EVs would have similar power and range capability of ICE vehicle. Therefore, new generation EV batteries will need to meet the demand of high power and energy capability. Power and energy capability of a battery cell are typically measured as per kilogram of battery

mass. A comparison among battery technologies has been done by *Kalhammer et al* which is shown in Figure 4 [10]. Power density is plotted against energy density of in-production rechargeable battery technologies i.e. lead-acid, nickel-cadmium (Ni-Cd), nickel-metal-hydride (Ni-MH), molten salt (ZEBRA) and Li-ion battery technology. It is noticeable that the batteries designed to provide high power have considerably lower energy density compared to similar battery technology.

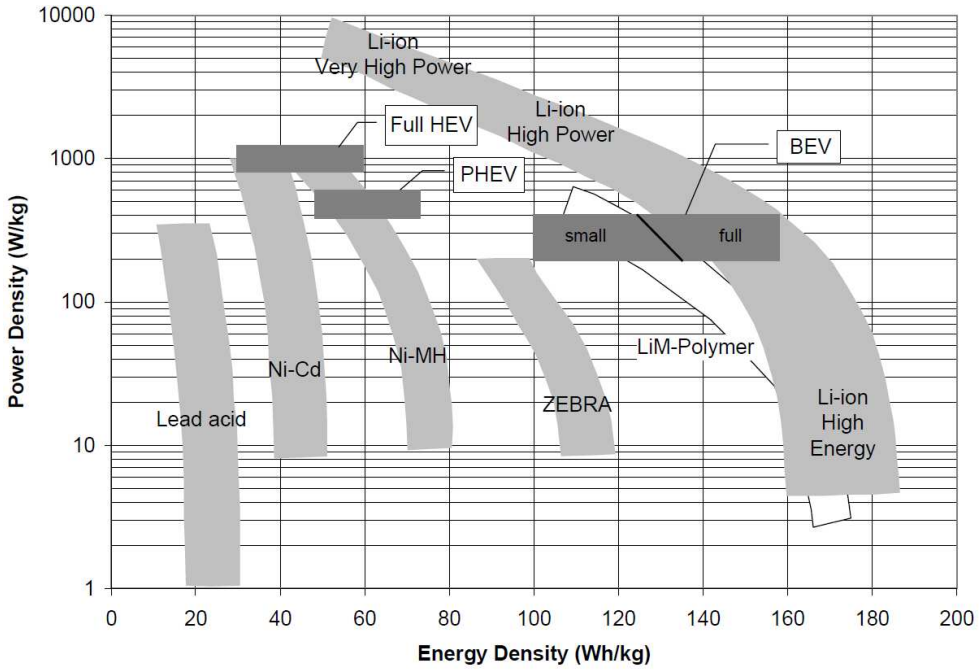

Figure 4: Comparison of battery technologies in terms of energy density and power density [10].

The rectangular domains in Figure 4 represent the approximate power and energy requirement of average EV types. All variants of lead-acid batteries have lower energy and power density as required by any kind of EV. Due to toxicity of cadmium, Ni-Cd batteries are banned from general purpose use [11] and ZEBRA batteries works at high temperature which previously identified as unsuitable for EV [10]. Therefore, practically Ni-MH and Li-ion can meet the energy and power

requirement of HEV and PHEV, and, for BEV li-ion is the only option. Previously HEVs and PHEVs with Ni-MH battery pack has been introduced e.g. *Toyota Prius V*. However, currently Li-ion is considered for automotive application as it is the only option for all types of EVs.

Li-ion batteries also have higher cycle life compared to the other battery chemistries and wide operating temperature range [9]. Higher charging efficiency and lower self-discharge rate make Li-ion batteries environment friendly and ensure they can retain charge for longer duration. Although, they are prone to overcharge and over-discharge, a battery management system (BMS) is commonly used to protect Li-ion batteries. These advantages of Li-ion battery over other battery chemistries put them into main focus for automotive use and thus are considered exclusively in this thesis.

1.3.3 Current concern with Li-ion battery

Sales of EVs have increased by 40% over last decade [12]. It is predicted the sales figure of EV during 2013, will be doubled in 2016 and more than tripled in 2020 [8, 13]. Technological advancement of Li-ion battery and development of next generation testing strategy will play a major role behind this market boom. Despite increased market share of EV, several recent incidents reveal that current testing can't provide the accurate knowledge of their performance in real world. Discrepancy of driving range shown on EV dashboard and actual distance travelled is a common issue with EV [14]. Battery capacity loss of Nissan Leaf reported in 2012, in several states in USA can be another good example [15]. Battery capacity available dropped well below the prediction (i.e. tested for). In another case GM recalled about 8000 Chevy Volts because of a battery issue (to prevent battery fire

after a crash) [16]. The most disturbing example can be the battery fire issue of BYD taxi in China, UPS Airlines Flight 6 crash due to Li-ion battery and Boeing 787 Dreamliner battery pack fire issue [17, 18]. All these incidents points to the inadequate testing of the Li-ion batteries for the application. Therefore, battery testing standards/legislations/ procedures need to be researched to propose any improvements necessary.

1.4 An introduction to testing requirements of EV batteries

OEMs need to evaluate battery performance, lifetime and safety accurately, for overall EV design, ensuring occupants safety and estimate battery warranty and performance. Batteries need to pass through different steps of evaluation process before they can be used for EV. The evaluation process starts with the battery datasheet supplied by the manufacturers. Like any datasheet, a battery datasheet provides key information of the battery. An example datasheet of Li-ion cell is shown in Figure 5.

Item	Specification
Nominal Capacity	20 Ah
Nominal Voltage	3.65 V
Standard Charge Method	CC(constant current) : 10 A and CV(constant voltage) : 4.15 V to 1 A
Rapid Charge Method	CC(constant current) : 20 A and CV(constant voltage) : 4.15V to 1 A
Standard Discharge Method	CC(constant current) : 10 A to 3.0 V
Continuous Discharge Current	≤ 100 A
Pulse Discharge Current (10sec)	≤ 200 A
Cell Dimension	Thickness : 7.2±0.2 mm (Fully charged state)
	Width : 129±0.5 mm
	Length : 216±1.0 mm
Operation Temperature	Charge : 0 to 40℃
	Discharge : -30 to 55℃
Storage Temperature	1 year : -30~25℃
	3 months : -30~45℃
	1 month : -30~55℃
Weight	425 ± 3 g

Figure 5: Datasheet of a Li-ion battery cell [19].

A datasheet provides important basic information on the battery cell such as capacity, voltage, maximum charge-discharge current, operating temperature, dimensions, weight etc. This information is helpful for preliminary selection of the battery. This information can be directly compared with EV requirements. However, it does not give insight into the battery performance over the entire operating conditions of EV. For example, nominal capacity does not promise that capacity will be retained either over the operating temperature range or at all charge-discharge rates. Generally, nominal capacity is measured at 25^{o}C with low C rate discharge, or at a temperature and C rate selected by the manufacturer. Automotive OEMs need to know the actual battery capacity over its operating temperature range and at different C rates. Similarly, maximum charge-discharge rates are not guaranteed for all temperature and at all SoC. There is no information about SoC vs open circuit voltage (OCV), internal impedance and electrical equivalent circuit of the cell. These are critical information for BMS to ensure reliable and safe operation of an EV battery pack.

As the battery datasheet lacks information needed for EV battery and powertrain design, automotive OEMs have need of testing batteries to gather the information they need. Characterisation tests are used to evaluate battery performance like energy density, power capability, open circuit voltage (OCV), internal resistance, AC impedance, for different operating scenarios.

1.5 Research problem

Since their introduction by Sony in the early 1990 [20], Li-ion batteries have been widely used as the main energy storage devices in portable consumer electronics.

They have gone through extensive amount of testing. However, these numerous tests were aimed mainly at the consumer electronics market. By nature, consumer electronics operate in a narrow temperature band close to room temperature and need only low power capability. Accurate estimation of remaining battery capacity although welcomed, is not a strict requirement. In contrast, an EV needs to operate in a wide temperature band and requires high power capability and needs to estimate remaining capacity, and thus remaining driving range, accurately. Therefore, characterisation tests designed aiming to characterise the batteries for consumer electronics applications are not suitable for EV application. Also, consumer electronics have relatively a short lifetime compared to a vehicle [21]. Long term performance of a battery is not a major issue for this application area as the product reaches end of life (EoL) well before the battery. However, it is a major concern for EVs, where long lifespan is desirable and minimum of 5 years battery warranty is required by legislation [22].

To assist the development process of Li-ion batteries for EV applications, different standardization body/organization published different test procedures/standard [23-27]. The common characterisation tests among these standards are capacity test, pulse power test and OCV test. In addition to these standard characterisation tests, researchers introduced other characterisation tests like electrical impedance spectroscopy (EIS) to gain insight into the electrochemical processes within the cell.

These characterisation tests are mainly adapted from the test procedure used for Li-ion batteries for consumer electronics and other battery chemistries for high power/energy applications. Although in extensive use, limited attention has been

given towards understanding these tests from an automotive perspective. Battery safety related test standards already have been identified as inappropriate for automotive applications and an attempt has been made to update them [28]. Although the battery characteristics important from an automotive perspective and thus the characterisation tests which measure these characteristics is known; however, the methodologies of the tests have not been investigated. In particular, accuracy and reproducibility of the characterisation tests from an automotive perspective and any additional parameters that needs to be introduced to the test procedure due to nature of automotive application have largely being ignored. Also, the test data might require a different interpretation for automotive (and similar) application compared to consumer electronics.

To ensure accuracy and reproducibility it is crucial to develop suitable test protocols which minimize uncertainties and introduce any parameter significant for automotive application. Also, test procedures need to be concise but record all cell behaviours (e.g. hysteresis of cell voltage), which are not significant for consumer electronics, but important for automotive application and not yet been considered.

1.6 Research question

The aims of this research are “how to improve accuracy, consistency and interpretation of characterisation test techniques for Li-ion battery cells for automotive applications”.

The following objectives will be pursued to reach the goal of the research mentioned above:

- Define requirements of automotive application
- Determine relevant characterisation tests for further investigation
- Evaluate existing test procedures/standards against automotive requirement
- Propose any improvements necessary to existing test procedures to ensure accuracy and reproducibility of test results
- Propose introduction of any new parameter to testing which are significant for automotive application
- Propose any requirement of different interpretation of test results
- Validate effect of these improvements

1.7 Thesis Outline

The thesis mainly comprises of three main parts. Chapters 2 to 4 cover Li-ion battery operation, testing requirements, limitations and identification of gap in knowledge. Chapter 5 is about proposed methodologies of research and evaluation of the methodologies. Chapters 6, 7 and 8 present experimental evidence along with discussion with the results. In Chapter 9 and 10 overall discussion, future extension and conclusions are presented.

Chapter 2 starts with an introduction about EV battery pack architecture. Construction and operating procedure of the cell have been discussed; which is followed by the explanation of how electrochemical procedures are represented with electrical equivalent circuit model. This chapter will provide baseline knowledge of Li-ion cell for the remaining chapters.

Current characterisation test procedures used by researchers and outlined in standards are reviewed in Chapter 3. The test procedures are discussed along with the theoretical background. Along with Chapter 2, this chapter aids to understand the gap between test procedures, Li-ion cell operation and automotive requirements.

An autopsy of current test procedures along with automotive requirements is reported in Chapter 4. The gap in knowledge with the characterisation tests are pin pointed in this chapter. This chapter end with a summary of gap in knowledge and research requirements of current characterisation tests.

The research approach to bridge the identified gaps with the characterisation tests is discussed in Chapter 5. The approach selected in this thesis provides a comprehensive perspective to the research problem and contributions to the research community.

In Chapter 6 presents experimental evidence that establishes the advantages of measuring battery capacity as Watt-hours instead of Amp-hours as per standard characterisation test. Also, proposal and evaluation of introduction of current de-rating as used by EVs to the capacity testing is discussed.

The repeatability and reproducibility of EIS test results are researched in Chapter 7. In this study relaxation which was not considered before for an EIS test has been researched and a minimum relaxation period is proposed.

OCV, a fundamental characteristic of Li-ion cell, is not measured as part of existing standard test procedures. In Chapter 8 an OCV test procedure is proposed and evaluated. The OCV hysteresis of different chemistry cells also measured using proposed methodology.

In last part of this thesis, an overall discussion and interconnectivity of contributions toward different characterisation techniques are included in Chapter 9. Also the significance of the contributions in contrast to the existing knowledge are discussed, which followed by natural extension of this work in future.

Finally, Chapter 10 presents the overall conclusions of the overall contributions made in this thesis.

2. A Review of Li-ion Battery Technology for Automotive Applications

Li-ion batteries have been widely used as main energy storage devices in portable consumer electronics and renewable energy storage [9, 29, 30]; however, it is only recently that Li-ion batteries have reached a degree of development that enabled their use in stringent automotive applications e.g. Tesla roadster began production in 2008 [31] and Nissan LEAF in 2010 [32]. Li-ion battery chemistries have always been of great interest due to their intrinsic properties such as (a) higher operating voltage, (b) higher energy density (c) longer cycle life and (d) lower self-discharge rate, compared to other commercially available battery chemistries [9, 10]. The introduction of Li-ion batteries in the automotive market has been the result of significant improvements in gravimetric & volumetric energy density [10, 33], cycle life [34, 35], cost [30, 36], manufacturing capability and manufacturing quality since their commercialisation in early 1990's [9, 10].

2.1 Essential parts of automotive battery

An EV battery pack is formed by a number of modules, and modules are formed from a number of cells as shown in Figure 6. The number of modules in a pack is not limited; it can vary from a single digit number to double digit number. Depending on the requirements, all the modules can be connected in series within the pack to have higher pack voltage. High pack voltage (several hundred volts) is essential as EV has high power demand. Relationship of power P, of battery pack with pack voltage V, and current I, is shown in Equation (1).

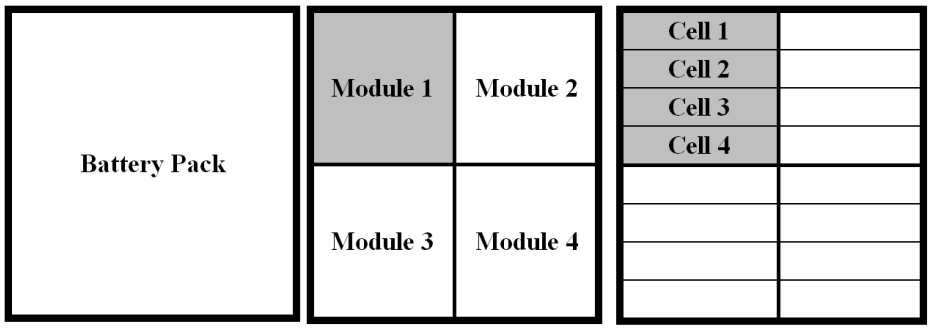

Figure 6: Basic structure of an EV battery pack

$$P = VI \tag{1}$$

The same amount of power can be supplied with higher voltage and lower current. Figure 7 shows an example of current and voltage combination for different output power. Lower current enables use of thinner current carrying conductors which reduces weight and cost of battery pack. Also, it reduces copper loss (I^2R) within current carrying conductors. However, use of very high voltage require higher degree of insulation and has its own set of problems. Commonly, pack voltage within the region of 300-600V is preferable for EV applications [23]. Module voltage can vary from less than 10V to higher than 100V depending on the design.

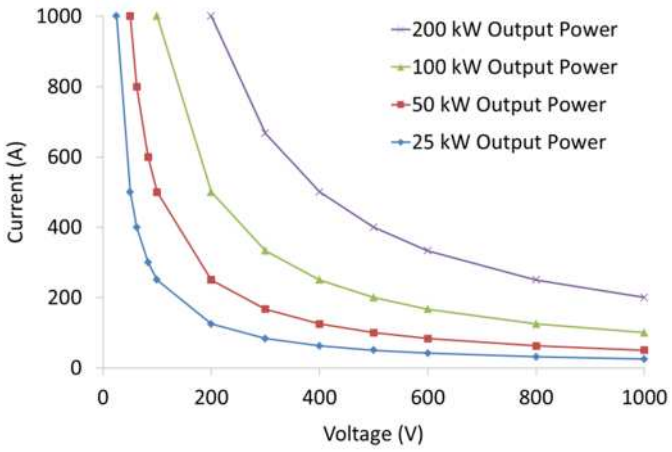

Figure 7: current and voltage relationship for different output power.

The number of cells in a module can vary depending on the voltage and capacity requirement. Cells in a module are connected in series or parallel or combination of series parallel combination. Series connection is used to achieve higher voltage and parallel connection to achieve higher current capability.

In an automotive battery pack, in addition to modules and cells, there are several components like bus-bars, battery management system (BMS), sensors, switches, cooling system, housing etc.; an example is shown in Figure 8.

Figure 8: Different components of an automotive battery pack. Photo courtesy: WMG centre HVM Catapult

The BMS has four main objectives, maintain the battery in a working state, protect the battery from damage, prolong lifetime of the battery, and communicate with the vehicle/host application. To achieve its objectives the BMS monitors several parameters e.g. voltage, current, temperature, coolant flow, SoC/DoD amongst

others. It also controls several parameters like charge-discharge process of the battery to give protection against over/under voltage, over current, over/under temperature etc.

The external power connector makes physical connection between battery pack and traction system of the vehicle. It also has another interface to communicate between vehicle and BMS. Bus-bars connect all the modules together and make connection between modules and external power connectors. During operation of batteries heat is produced due to I^2R loses arising from the internal resistance of the battery. A cooling system is used to maintain battery temperature close to target operating temperature. All the battery pack components are housed within a casing which also provides mechanical stability of the pack and protects the component from damage by external environment.

The price breakdown of a 25kWh EV pack is shown in Figure 9. A large portion of battery pack cost is attributed to cells cost; which is around 60% of total cost of the battery pack [37]. This makes cells most important component of a battery pack, as well as being least understood! Cells will be further reviewed in next Section.

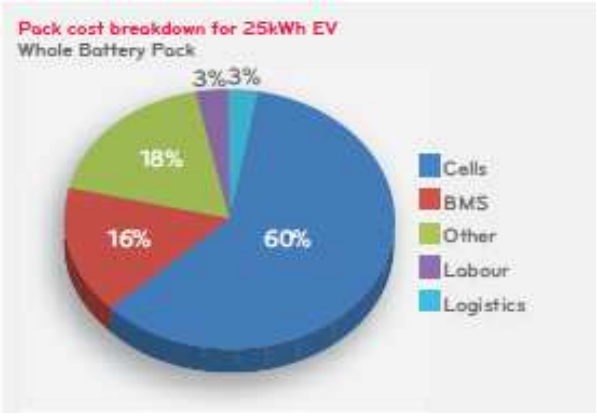

Figure 9: Material cost breakdown of a 25kWh EV battery pack [37].

2.2 Li-ion battery cell construction and material

2.2.1 Components of Li-ion battery cell

Like any other battery cells, Li-ion batteries also have four main components, anode, cathode, electrolyte and separator. The basic construction of a Li-ion cell is shown in Figure 10. The negative electrode is referred to as anode and the positive electrode as the cathode (while being discharged). Electrical charges are carried by lithium ions inside the cell from one electrode to another. From electrode, electrical charges are collected by current collector, which then taken to the external circuit. Electrolyte provides the medium for lithium ion transfer and separator mainly provides a physical barrier between electrodes, while allowing lithium ions to pass through.

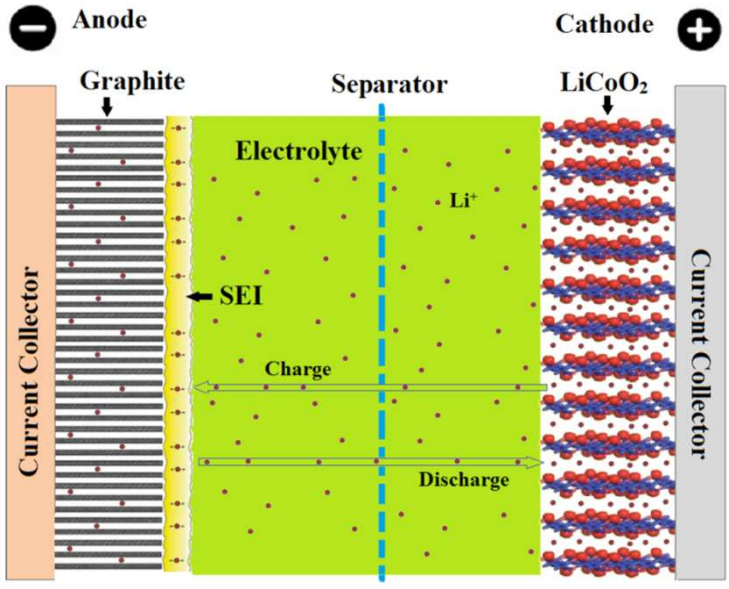

Figure 10: Basic construction and operation of a Li-ion battery cell.

2.2.2 Cathode

The fundamental requirements of electrodes are they should react with lithium in a reversible manner without changing the basic electrode structure and in order to

achieve higher energy and power capability they should have high electronic and ionic conductivities. Furthermore, the cathode should contain a readily reducible ion, like a transition metal. Moreover, it is expected that the cathode material should have a high free energy of reaction with lithium (energy released in an electrochemical reaction) to maximize energy density of the cell. Another important requirement is the electrode potential (electrode potential appears at the interface between an electrode and electrolyte due to the transfer of charged species across the interface) should be below the maximum stable potential of electrolyte.

Cell chemistries are generally named based on the cathode material. The cathode chemistries of commercially available cell chemistries in last decade and present days are listed in Table 1 with performance of the cells.

Table 1: Comparison between different Li-ion cell cathode chemistry and performance of respective cell with carbon anode.

Cathode Chemistry	Energy Density Wh/Kg	Maximum power C-rate	Cell Voltage Volt	Discharge temperature ^{o}C	Cycle life at 25^{o}C (approximate)	Thermal Runaway ^{o}C
Lithium Cobalt Oxide (LCO)	170-185	1-3	3.6	-20 to 60	1000	170
Lithium Manganese Oxide (LMO)	90-110	3-5	3.8	-20 to 50	>1000	255
Lithium Nickel Cobalt Manganese (NMC)	150-180	5-30	3.7	-30 to 60	1500	215
Lithium Iron Phosphate (LFP)	80-125	10-30	3.2	-30 to 60	2000	270

The first commercialized Li-ion batteries used Lithium Cobalt Oxide - $LiCoO_2$ (LCO) as the cathode material [38]. This type of battery has been widely used in 1990's, 2000's and also in present days. It is the cheapest chemistry Li-ion cell

available in the market because of their high volume production [30]. $LiCoO_2$ is very thermodynamically stable which makes fabrication process easier and have high energy density (Table 1). Although, it has lower maximum current capability but it has moderate cycle life (~1000 cycle) and high cell voltage. However, cobalt is toxic when exposed to environment and can catch fire under aggressive conditions like overcharge, piercing, puncture [30].

Spinel Lithium Manganese Oxide - $LiMn_2O_4$ (LMO) has different atomic structure compared to LCO [39]. Use of manganese makes cathode materials very low cost and use of this chemistry overcomes some of the problems of LCO cells. They offer higher thermal runway temperature and manganese is less toxic compared to cobalt. They also have higher cell voltage than LCO cell and slightly higher cycle life. But all these advantages come at a cost of lower energy density.

Lithium Nickel Manganese Cobalt - $LiNi_xMn_zCo_yO_2$ (NMC) cells blend the advantages from LCO and LMO cells. They have almost similar energy density as LCO cells, much higher power capability and cycle life compared to LCO and LMO cells, and improved safety characteristics compared to LCO cells. Also, they are cheaper than LMO cells.

Since 2000s Lithium Iron Phosphate - $LiFePO_4$ (LFP) has been considered as a promising cathode material for the cells for EV and other high power applications due to their higher maximum current capability and better safety characteristics compared to the LCO, LMO and NMC cells. They are less prone to catch fire under aggressive conditions as there is no release of oxygen [36]. They also have much

higher cycle life compared to the three chemistries discussed above [35]. The drawbacks of these cells are they have lower energy density and lower cell voltage.

2.2.3 Anode materials

In Li-ion batteries the simpler anode material is metallic lithium. However, risk of internal short circuit due to lithium dendrite growth limits its use in commercial cells. Numbers of anode materials have been proposed including variations of carbon, silicon, tin, titanium and alloys of these materials. However, for commercial cells graphite, hard and soft carbons are mainly used as anode material [38, 40-43].

Carbon based anodes comply with most of the electrochemical selection criteria and are available in large quantities at a very low cost [43, 44]. Carbon is available in various forms like graphite, soft carbon, and hard carbon; however, their lithium insertion reaction is the same:

$$xLi + 6C \rightleftharpoons Li_xC_6 \quad (2)$$

In the Equation, the value of x depends on type of carbon and it is within 0 to 1 [20]. In the case of graphite, lithium can diffuse between the graphene planes quickly and maximum number of lithium can diffuse (theoretically LiC_6 [44]). Therefore, graphite has the maximum specific capacity among carbon variants and has endured as main anode material.

The use of Lithium Titanate Oxide – $Li_4Ti_5O_{12}$ (LTO) as an anode material provides a unique advantage compared to carbon. Lithium intercalation into the LTO does not make much change to the atomic dimensions of LTO [45]. Therefore, with cycling, mechanical degradation of this anode material is minimal which is reflected as high

cycle capability of this material [46]. The main disadvantages of this material are it has low capacity compared to carbon and LTO has high working voltage vs lithium which significantly reduces cell voltage i.e. further reduction of energy density. However, higher working voltage eliminates any passivation layer on anode surface (explained later in Section 2.3) which enables higher power capability, superior thermal and chemical stability, and also very high cycle capability.

2.2.4 Electrolyte

Electrolytes have little flexible requirements compared to electrodes. Electrolyte is an ionic conductive material which has good insulating properties for electrons. Ideally it is chemically inactive material; provide a medium for ion transfer between two electrodes.

Although, ideally electrolyte is chemically inactive, however, the power density of the cell depends on the electrolyte. The properties of electrolyte limit how fast ions can move. There are two types of electrolytes namely non-aqueous organic liquids and polymer electrolytes are commonly used in commercial Li-ion battery cells.

The organic liquids consist of lithium salt dissolved were the earliest electrolyte for Li-ion cells which are still being used. Carbonates like propylene carbonate (PC), ethylene carbonate (EC), diethyl carbonate (DEC), dimethyl carbonate (DMC), ethylemethyl carbonate (EMC) or any mixture of two or more are previously proposed and used [47]. These carbonates have high oxidization potential vs lithium and low reduction potential vs lithium, which indicate that the electrolyte will be chemically inactive within a large voltage window. Within that voltage window

other electrode reactions can take place. The main problem with carbonates is they are highly flammable which pose significant safety hazard.

Polymer electrolytes are polymeric materials containing metal salt. This type of electrolyte not only works as solvent for the salt but also maintain separation of the electrodes. Polymer electrolytes are mainly two types, gel polymer electrolytes and solid polymer electrolytes. Gel polymers contain a polymer which is gelled with organic solvent. These types of electrolytes are currently being used for Li-ion cells. Solid polymer electrolytes use ether based polymers like polyethylene oxide, polypropylene oxide, containing dissolved lithium salt. Main issue of these types of electrolytes are low ionic conductivity. However, they offer flexible cell design and elimination of separator and most importantly improved safety by removing highly flammable carbonates. Therefore, they have received a major research focus [47]. The cells used for this research mainly use EC and EMC as electrolyte.

2.2.5 Separator and current collector

The separator within the cell is a porous membrane which provides a physical barrier to the anode and cathode, while allowing ion transfer between the electrodes. The separator itself is inactive material but its properties and structure considerably define power capability of the cell, energy density, cycle life and most importantly safety. The most critical parameters for Li-ion battery separator are thickness, pore size and porosity. Thinner the separator is lower the thickness of the battery and lower the ion transfer resistance. However, thinner separators have less mechanical stability and are prone to puncturing; hence, a balance is usually made. Commercially available Li-ion batteries mostly use different form of polyolefin e.g.

polyethylene, polypropylene, microporous thin (<30 μm) separator [48]. They have good mechanical and chemical stability, and are cheap to manufacture.

Current collector is used to collect electrical current generated within an electrode material and deliver it to an external circuit; in other electrode this current from external circuit is then distributed within electrode material. Current collectors need to have high electrical conductivity and they should be chemically inactive in the presence of electrode and electrolyte materials. The electrode materials are actually coated on the current collector. Usually aluminium and copper foils are used as current collector. Aluminium is less prone to corrosion vs lithium at higher operating voltage of cathode and copper is less prone to corrosion at lower operating voltage of anode [49]. Therefore, commercial cells mostly use aluminium foil as cathode current collector and copper foil as anode current collector.

2.2.6 Production and types of commercial Li-ion cell

The fabrication process of Li-ion cell is highly automated and uses sophisticated technology. The anode, cathode and separator of Li-ion cell is prepared like thin sheet of tapes and rolled on reels like tape. Using automated winding machines these tapes are cut into the proper size, made into a sandwich of anode-separator-cathode and rolled to produce a tight ‘jellyroll’ construction. The jellyroll is then loaded into a cell casing and electrolyte is added and finally sealed. Li-ion cells are packaged in different casing, mainly categorized into three types, cylindrical, pouch and prismatic. Basic construction and example of these cells are shown in Figure 11.

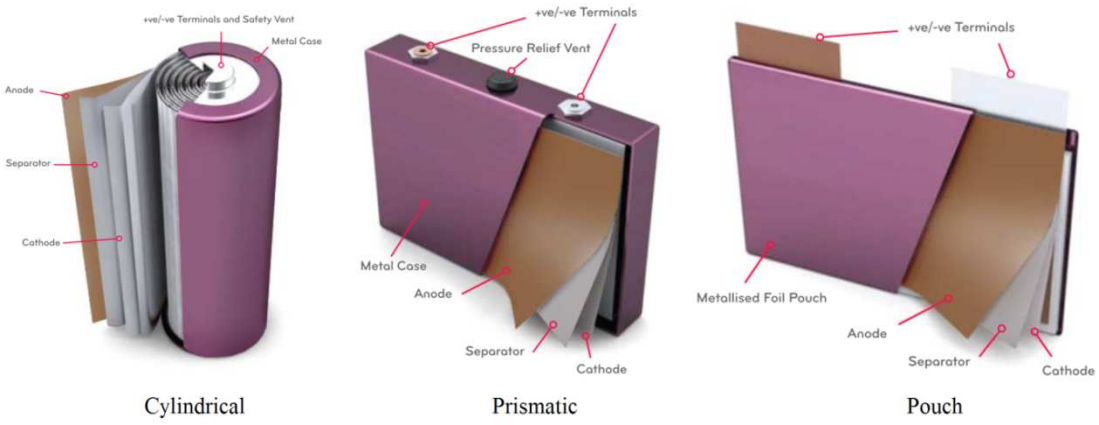

Figure 11: Construction of cylindrical, prismatic and pouch Li-ion cell [37].

Cylindrical cells are packed in a cylindrical shaped metal can. Cylindrical cells are one of the high volume production cells. The 18650 cell (18 mm diameter, 65 mm long) standard cells are commonly used in laptops and other consumer electronics. Box shaped aluminium or steel cans are sometimes used to house Li-ion cell. These types of cells are called prismatic cell. Pouch cells are normally rectangular shaped cells where instead of using metallic housing thin layer of plastic is used to seal the cell from external environment. Because of the absence of metallic housing they have higher energy density, higher power density and higher packaging efficiency compared to other two formats. This type of cell can be made in any size and shape and are not bound by standard sizes.

2.3 Operation of a Li-ion battery cell

A Li-ion battery cell operates following a simple process; it converts electrical energy into chemical energy during the charge process and converts stored chemical energy into electrical energy during discharge. Electrical equivalent circuit of a cell during charge and discharge are shown in Figure 12 (a) and Figure 12 (b)

respectively. Inside the cell energy conversion and storage is done by lithium ion, shuttling between electrodes during charge and discharge. This process was presented in Figure 10. During discharge, cathode is positive terminal and anode is negative terminal, which is reversed during charge, and cathode works as negative and anode as positive terminal.

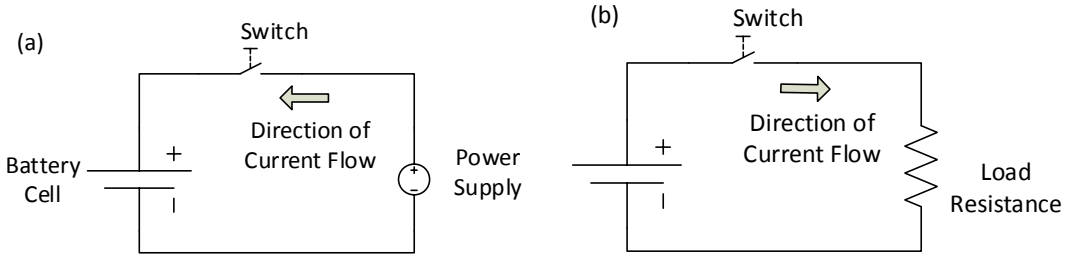

Figure 12: Electrical circuit diagram of a cell during (a) charge and (b) discharge.

While charging, at the cathode, a lithium atom gives up an electron and becomes a lithium ion. This lithium ion travels to the anode through electrolyte and electron also travels to the anode through external circuit. At the anode the lithium ion accepts an electron and becomes a lithium metal. This process is known as intercalation. During discharge, the opposite reaction happens, lithium gives-up an electron at anode and move to cathode, where it becomes lithium metal again by accepting electron. This process is known as de-intercalation. For example, the reactions for lithium cobalt oxide ($LiCoO_2$) cathode and graphite anode are shown below:

Cathode half reaction is:

$$LiCoO_2 \leftrightarrow Li_{1-x}CoO_2 + xLi^+ + xe^- \quad (3)$$

Anode half reaction is:

$$xLi^+ + xe^- + xC_6 \leftrightarrow xLiC_6 \quad (4)$$

2.3.1 Origin of cell voltage and capacity

When a reaction occurs, there is a release or absorption of energy which is commonly known as a decrease of free energy of the system and expressed as:

$$\Delta G^o = -nFE_e^o \tag{5}$$

Where, F is the Faraday constant (value: $9.65 \times 10^4\ C\ mol^{-1}$), n is the number of moles of electrons transferred in the reaction and E_e^o is the electrode potential for reaction. The difference in the free energy in the two electrode reactions is the energy supplied to/from the external circuit. In the absence of any current flow, electrode potential vs ions in the solution i.e. Li^+ can be measured experimentally using a reference electrode and high impedance voltmeter, and also can be calculated from Nernst equation (Equation (6) [50].

$$E_e = E_e^o + \frac{2.3RT}{nF}\log\frac{C_o}{C_R} \tag{6}$$

Where, R is the universal gas constant (value, $8.31\ JK^{-1}mol^{-1}$), T is the absolute temperature (K), and C is the chemical activity of ions, where C_o is the oxidant and C_R is the reductant.

Figure 13 shows the equilibrium potential of the electrode materials (used for Li-ion cell) vs lithium ion and the operating region of carbonate electrolyte. Lithiated graphite anode has an equilibrium potential of 0.05 V and LTO anode has approximately 1.5 V vs lithium ion [30, 51]. Depending on the variant, delithiated cathode has a voltage of around 4V except LFP which has a voltage around 3.3V [30, 52].

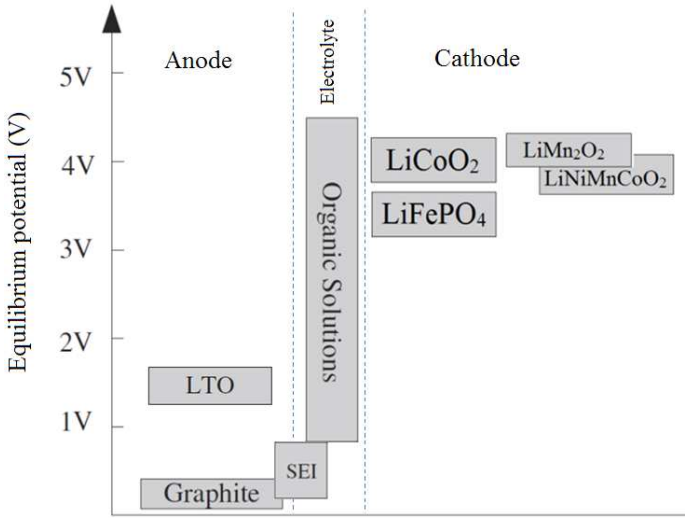

Figure 13: Stable working voltage of different cell material vs Li/Li^+.

The cell voltage is simply the difference of the equilibrium potential of the electrodes:

$$E_{cell} = E_c^e - E_a^e \tag{7}$$

Where, E_c^e and E_a^e are the equilibrium potential of the cathode and anode respectively. Therefore, when NMC cathode is used with graphite cathode the cell voltage is approximately 4V at fully charged state. When graphite anode is replaced with LTO the cell voltage will become around 2.5V at fully charged state.

Capacity of the cell depends on the total amount of lithium ion which can shuttle between two electrodes. These lithium ions are commonly known as active lithium or cycle-able lithium. The amount of cycle-able lithium at the anode defines the SoC of the cell [20, 52]. When all the active lithium is at the anode it is called 100% SoC i.e. fully charged. When there is no active lithium at anode it is called 0% SoC i.e. fully discharged. Electrode potential changes when lithium concentration at the

electrodes changes. Because of this, cell voltage changes with SoC. As an analogy of the operation of Li-ion cell and change of cell voltage, a simple water tank model shown in Figure 14, can be used which was originally proposed by *Han et al.* [52].

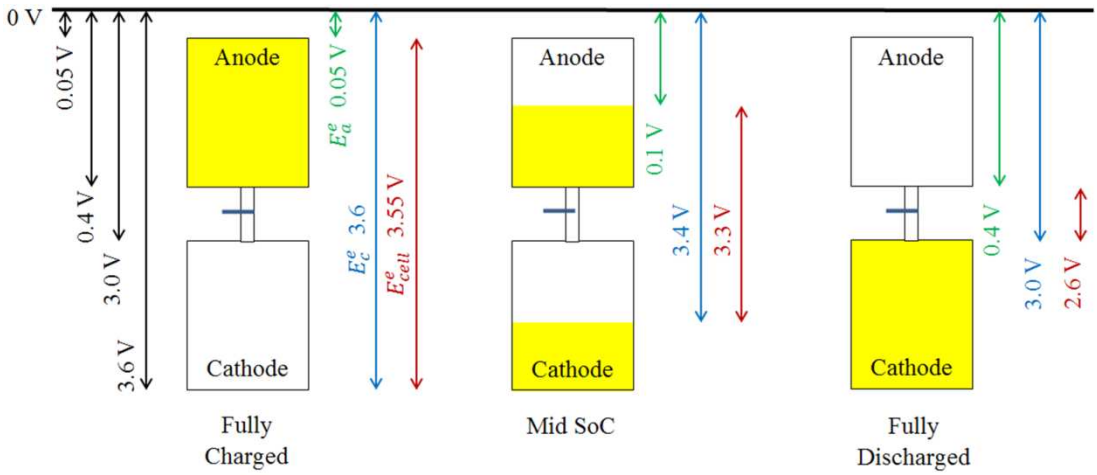

Figure 14: Simple water tank model of Li-ion cell with example data of graphite anode and LFP cathode. Yellow shaded area shows the percentage of lithiated electrode. Figure adopted from [52].

Here two tanks are connected and lithium can be transferred from one tank to another representing charge-discharge. The yellow shaded area shows the percentage of the lithiated region of the electrode. When fully charged, all cycle-able lithium is at anode. At this point considering a graphite anode and LFP cathode they will approximately have equilibrium potential of 0.05 V and 3.6 V respectively and hence the cell voltage will be 3.55 V. When the cell is discharged to mid SoC, about half of the cycle-able lithium will move to cathode, causing decrease in cathode's equilibrium potential and increase in anode's equilibrium potential, which will reduce cell voltage. Finally, when cell is fully discharged, all the cycle-able lithium will be at cathode, causing further reduction of cell voltage. This model is a simple

illustration of the complex process. Therefore, actual capacity of the electrodes and equilibrium potential may vary. The change of OCV of a Li-ion cell with LFP cathode and graphite anode is shown in Figure 15. It is clear that rate of change of cell voltage is not the same for the cell from fully discharged state to fully charged state. This OCV is the cell voltage when cell is at electrochemical equilibrium, which is different compared to cell under load (being charged or discharged), further explained in Section 3.4.

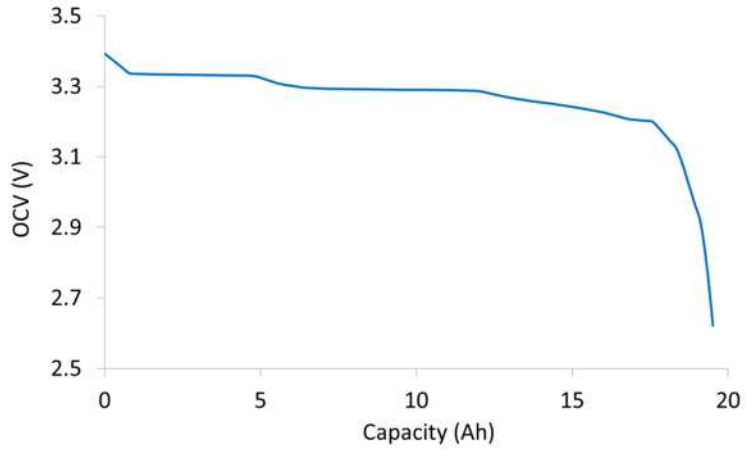

Figure 15: Open circuit voltage of a Li-ion cell with LFP cathode and graphite anode.

2.3.2 Origin of cell power capability and impedance

The rate of intercalation/de-intercalation process at an electrode defines the maximum current (thus the maximum power) of the cell. To increase current capability of the cell/electrode a simple way is to increase surface area to be in contact with electrolyte i.e. active surface area. The rate of intercalation/de-intercalation, thus the maximum current is linearly related to the surface area. Increasing surface area by using large piece of electrode is a simple solution but not

always practical due to size requirement of the cells. One way to increase surface area not by using a large piece of electrode is make it porous. Pores within the electrode increase the surface area and thus the maximum current [53, 54].

Internal impedance of the cell originates from four main areas, impedance of electrode materials, electrode electrolyte interface, current collector and electrolyte. The impedance of electrolyte is generally a simple resistive value. The impedance of current collectors are also resistive; however, depending on the design, they can show a little inductive behaviour [55]. When a potential is applied to a surface, electrodes confer a capacitance, as originally described by the *Helmholtz* model. When an electrode surface come into contact with electrolyte, multiple layers of solvent molecules and ions that are *specifically absorbed (anions)* at the interface, as shown in Figure 16. This inner layer is called the *compact, Helmholtz layer* and the plane of electrical centre (x_1) is known as *inner Helmholtz plane (IHP)* [56]. At a distance of x_2 solvated ions (cations) can approach. This layer is called *outer Helmholtz plane (OHP)*. These ions are known as *non-specifically absorbed* and are distributed in a three-dimensional region called *diffuse layer* which extend from OHP to the *Nernst diffusion layer* and to the bulk of the electrolyte. The thickness of the diffuse layer depends on the total ionic concentration in the solution. The double layer is approximated using a resistor and a capacitor C_d [56]. Therefore total cell impedance is a combination of resistance, capacitance and inductance.

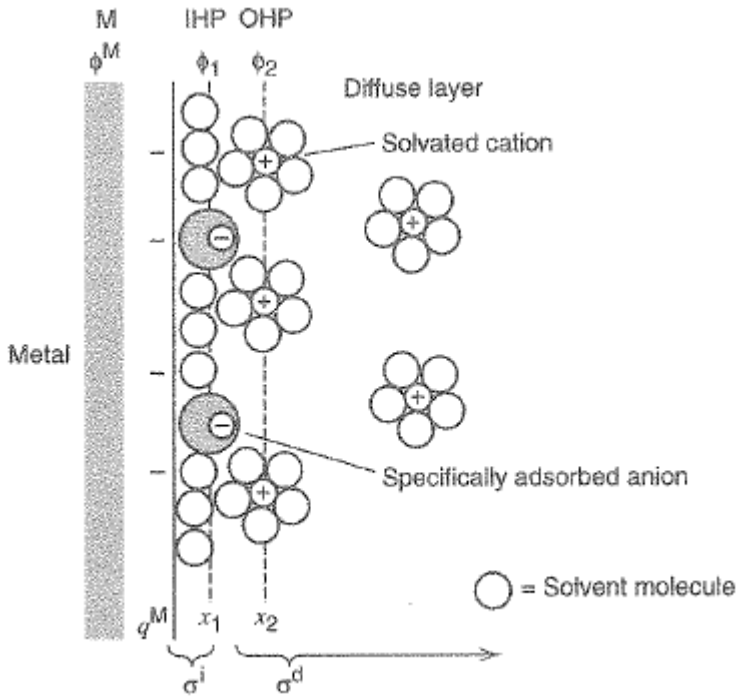

Figure 16: The model of double layer region as proposed by [56].

Commercially used carbonate electrolyte is stable within the voltage range of 0.8 to 4.5V, which is beyond the stable voltage of graphite anode [52]; as shown in Figure 13. Therefore, theoretically the anode-electrolyte interface is unstable and the electrolyte will decompose with lithium molecules at anode surface. However, at the very first charging of the cell, decomposition products build up on the anode surface, resulting in the formation of a protective layer on anode surface, which protects the anode from further decomposition. This protective layer is known as the solid electrolyte interface (SEI) [52, 57], shown in Figure 10. This SEI layer also increases the cell impedance and decrease maximum power capability, as lithium ions need to diffuse through SEI layer to move into and move back out of the graphite anode. As two charged surfaces are separated by SEI layer, it forms a capacitance. The electrode potential of LTO anode is around 1.5 V, which is well within the stable voltage range of the electrolyte. Therefore no SEI layer forms on LTO anode.

2.3.3 Variation of cell capacity, OCV, power and impedance with other variables

2.3.3.1 Charge-discharge rate dependency

The amount of total cycle-able lithium available and thus the capacity of the cell depend on different factors, like charge-discharge rate, temperature, ageing state etc. Electrodes have a limitation in how quickly lithium can move from/into the electrode i.e. rate of intercalation/de-intercalation process. The higher the rate used, lower the total amount cycle-able lithium can shuttle between electrodes. Further explanation of the rate dependency of capacity will be shown in Section 3.1.

2.3.3.2 Temperature dependency

Chemical reactions are highly dependent on temperature. Chemical reactions of a Li-ion battery are slowed down at low temperature and increase at high temperature, compared to room temperature. Also, the diffusion process slows down with temperature drop. Therefore, Li-ion batteries have lower capacity and power capability at low temperature, and higher capacity and power at higher temperature. The change of capacity and power of a cell at different temperature is shown in Figure 17. However, operating a cell at higher temperature has different issues related to safety and ageing which will be covered in Section 2.3.4. The variation of electrode potential with temperature is explained with Nernst equation (Equation (6). The variation of electrode potential with temperature is dependent on the electrochemical composition of the electrode (i.e. $\log\frac{C_o}{C_R}$ of Nernst equation is dependent on chemical composition of the electrode). Therefore, the change of

equilibrium potential of the cathode (E_c^e) and anode (E_a^e) will be different, changing the total cell voltage with temperature.

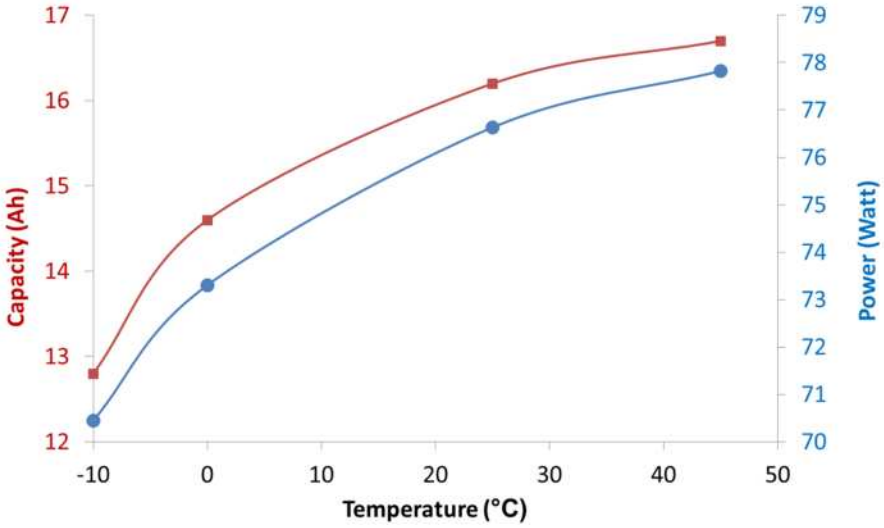

Figure 17: Change of capacity and power with temperature. Data reported by *Zhang et al.* [58].

Like electrochemical reactions and diffusion process, ionic conductivity of the electrolyte is also lower at lower temperature. Thus, impedance of the cell varies with temperature.

2.3.3.3 Time dependency

The electrode potentials E_c^e and E_a^e are dependent on ionic concentration in close proximity of the electrodes (C_o and C_R in Nernst equation). When a cell is charged or discharged, the ionic concentration around the electrode changes. After the charge/discharge event the cell needs to rest for the ionic concentration to reach equilibrium. Within this period as ionic concentration changes, E_c^e and E_a^e also change, so does the cell voltage. Among researchers this is known as relaxation of

cell voltage. As impedance is also dependent on the ionic concentration, cell impedance might change over the time of this relaxation.

2.3.4 Ageing process of the cell

Capacity fade and power fade (impedance rise) of a Li-ion battery with use is known as ageing [43, 59]. There are several ageing mechanisms that can be present in a cell depending on operating conditions i.e. cycling, storage. Ageing mechanisms are directly related to the chemical composition of electrodes, electrolyte and other cell components. However, there are similarities in the main ageing mechanisms between lithium-ion battery chemistries. Generally, it is known that capacity fade of a lithium-ion battery cell is due to three main reasons:

- Loss of active lithium [43, 52, 60]
- Loss of active electrode surface area [42, 43, 52]
- Loss of electrode & electrolyte material [42, 43]

The impedance rise of the lithium-ion battery cell is commonly attributed to following ageing mechanisms:

- Surface film formation on electrodes i.e. SEI [58, 61]
- Loss of active electrode area [43, 59]
- Increased charge transfer resistance [62]
- Degradation of separator, binder and current collector [59, 63, 64]

The common ageing mechanisms which cause capacity fade and impedance rise are visualised in Figure 18 which also shows their origin.

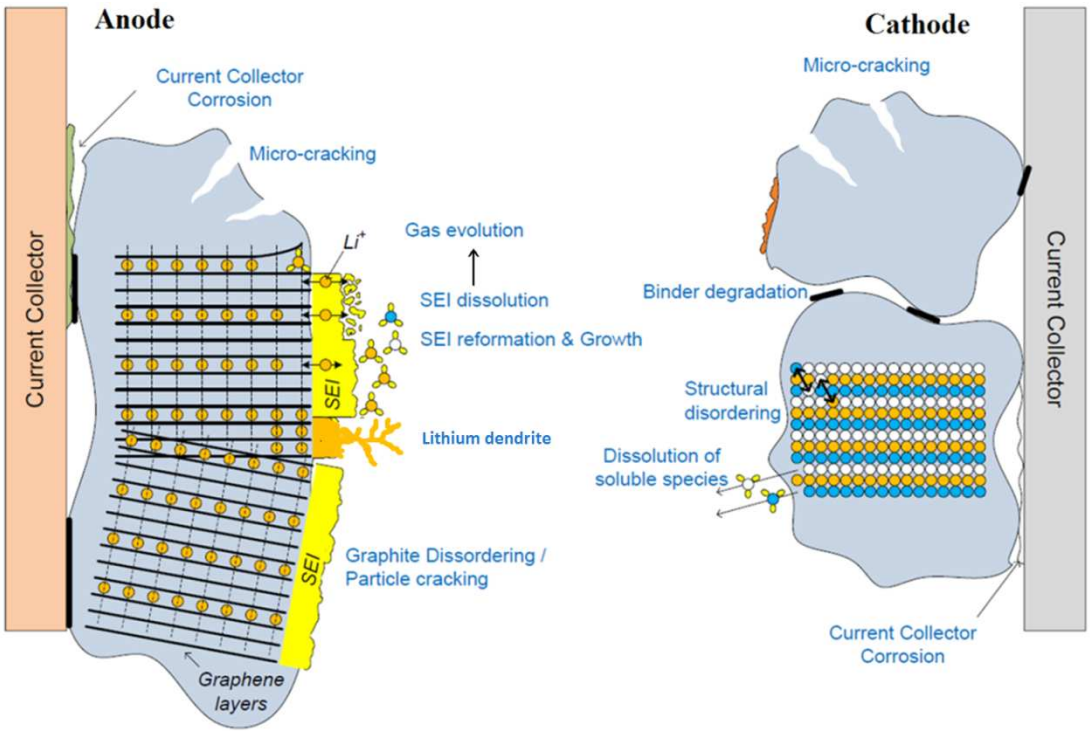

Figure 18: Main ageing mechanisms of li-ion battery. Figure adapted from [65].

At the anode surface, SEI formation mainly takes place during very first charge and continues to grow with further charge-discharge of the cell [52, 66]. Rate of SEI growth is higher when cells are cycled or stored at high temperature [67, 68]. With SEI formation, capacity fade (amount of cycle-able lithium reduces) and impedance rise continue throughout the lifetime of the cell. The graphite anode also has reduced diffusivity to lithium-ion at low temperature [69, 70]. Therefore when charged at low temperature (when lithium diffuse into graphite anode) or with very high C rate charging excessive lithium which do not have enough time to diffuse into graphite anode, grows like a dendrite [69-74]. This is a major safety risk involved with Li-ion cells used at low temperature and high C rate.

At the cathode, structural deformation and metal dissolution are two major sources of ageing. The geometrical deformation of atomic structure at the cathode, which is

known as Jahn-Teller distortion [75, 76] leads to formation of inactive atomic structure with lithium. Thus, this results in volume change and capacity fade [52, 77]. Also, metal dissolution (e.g. Mn^{2+} in LMO cell) to electrolyte contributes further in reduction of active material, thus battery capacity.

At both electrodes there are some mechanical changes that can happen such as micro cracking [43, 52, 60], gas formation [42, 43, 59, 60]. Degradation of inactive components like binder degradation, separator creep [78, 79] and current collector corrosion happens at both electrodes [59, 63, 64].

2.3.4.1 Summary of ageing mechanisms

As far as the ageing mechanisms have been discussed, they are summarised in Figure 19. This provides an overview of the origin of the ageing mechanisms, cause and effect of the ageing mechanisms, and mentions what it leads to. Also, the features which accelerate these ageing mechanisms are shown in yellow boxes. As mentioned earlier in this Section, ageing mechanisms are interconnected, e.g. when lithium plating occurs, more SEI will form. It also can be noted that, majority of the ageing mechanisms are accelerated at high temperature when kinetics of the ions are high. Use of high charge-discharge current is the next largest accelerating factor. For more details of ageing mechanisms of Li-ion cells, the author suggests the following literature [41-43, 52, 59].

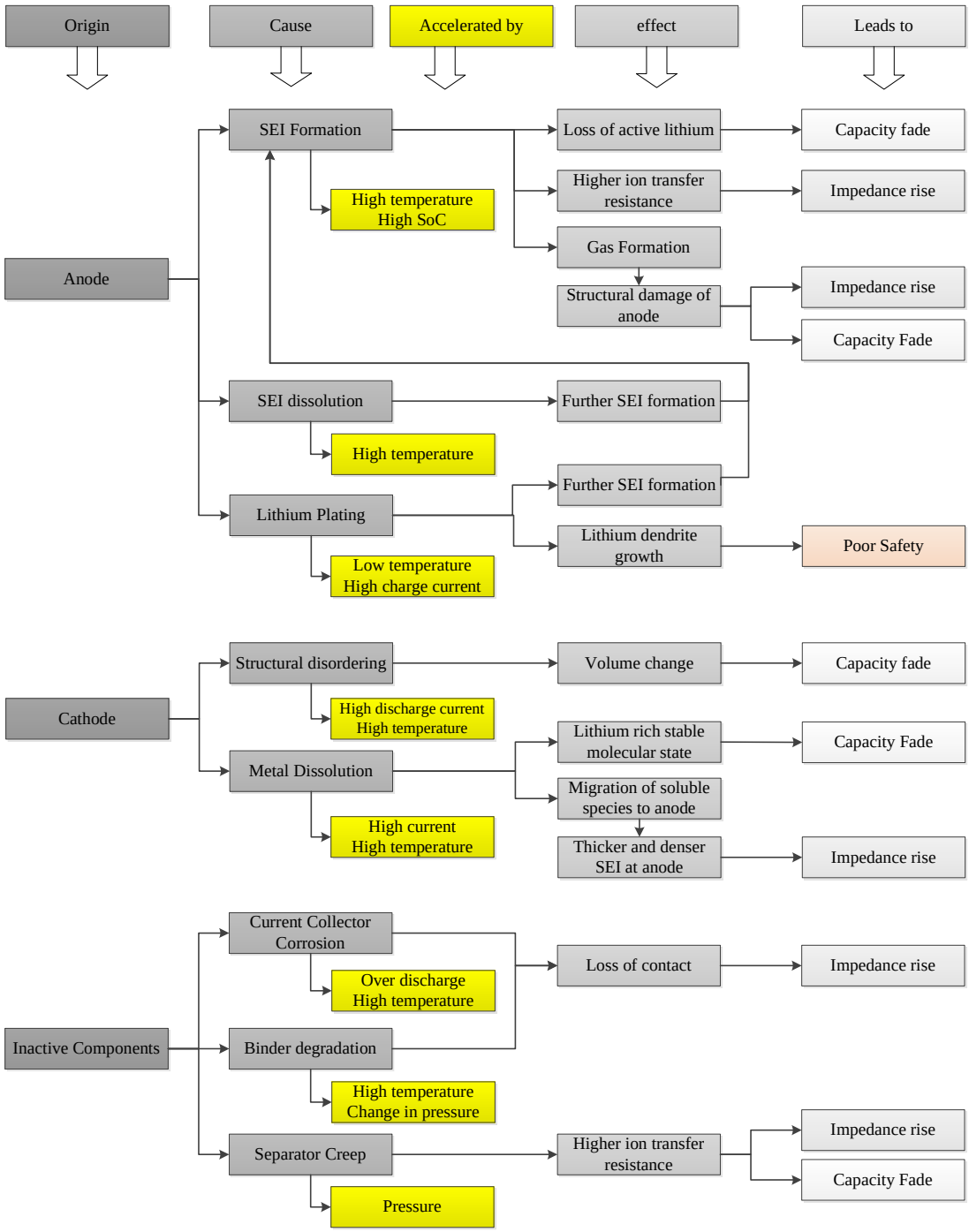

Figure 19: Cause and effect of main ageing mechanisms and their accelerating factors of li-ion cell.

2.4 Electrical equivalent circuit of a cell

The electrochemical processes within the cell are often represented with equivalent electrical components, known as equivalent circuit model (ECM) of the cell. ECMs

are commonly used to evaluate electrical performance (e.g. current, voltage, power, energy) of the battery in real world operating conditions. ECMs have a wide range of applications, varying from on-board SoC estimation [80-82] to long-term ageing estimation [35, 62, 83]. A substantial amount of research has been done on equivalent circuit modelling of the lithium-ion battery [80, 81, 84-87]. ECMs of the simplest form [84] to very complex form [85] have been proposed which represent the electrical and electrochemical behaviour of the cell.

The simplest form of ECM is shown in Figure 20. In this ECM, V_{ocv} represents the open circuit voltage of the cell, E^{e}_{cell}, and the resistance R originates from multiple sources i.e. electrolyte, separator, current collector, binder, diffusion of lithium into electrodes. Due to this resistance, the cell terminal voltage changes under load because of voltage drop at resistance R. Also, heat is generated inside the cell following Joule heating (I^2R) during operation, which is reflected as cell (surface) temperature increase. This ECM is simple but fails to demonstrate the different electrochemical processes within the cell.

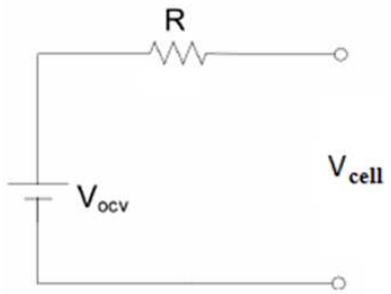

Figure 20: Simplest Li-ion battery model.

To reflect different electrochemical processes researchers have proposed different, more complex, ECMs [55, 88-90]. An example of the complex ECM of a Li-ion cell which has been commonly used in previously published work shown in Figure 21.

This type of equivalent circuit is known as Randles equivalent circuit and may have different combinations of resistor, inductor and capacitor to represent different electrochemical processes [91].

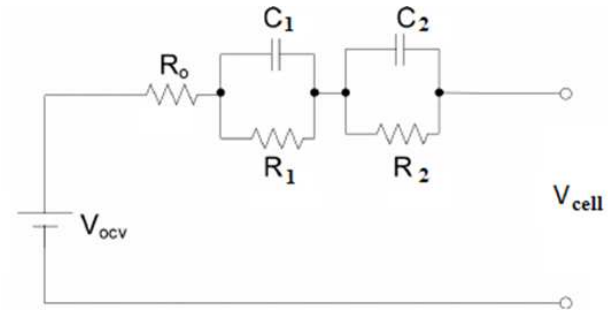

Figure 21: An equivalent circuit model of Li-ion cell.

The Ohmic resistance R_o is the sum of ion transfer resistance of the electrolyte and separator, and electrical resistance of the current carrying components like current collector. Generally, the capacitance is called double layer capacitance of the cell [80, 81, 92, 93]. The RC circuit which is represented by C_1 and R_1 in the equivalent circuit represent this capacitance and charge transfer resistance of lithium into electrode. The SEI layer on anode surface will form another RC circuit. Charge carrying ions and electrons at anode is separated by SEI layer; which works as a capacitor; which is represented with C_2 and R_2 in the equivalent circuit [92, 94]. Often these RC circuits are mentioned as RC time constant. Depending on the complexity of the equivalent circuit, there can be more RC branches, representing different electrochemical processes within the cell [55, 89].

The components (V_{ocv}, R_o, R_1, R_2, C_1, C_2) shown in Figure 21 need to be characterised to build-up the model. The methodologies used to characterise these

parameters are commonly known as characterisation tests, which will be discussed further in Chapter 3.

2.5 Summary

Different parts of an automotive battery pack are discussed in this chapter. BMS is one of the key components which ensure safe operation of the battery pack and translate the battery condition for the user. However, cells are the smallest energy storage blocks of the battery pack, which claims largest portion of total cost of a battery pack. The construction and individual component of a cell is discussed. The detailed explanation of the electrochemical operation of the cell including how open circuit voltage and capacity are formed, how power capability vary at different operating conditions is reported (Section 2.3). Finally, how the electrochemical processes within the cell are translated for a modeller as electrical parameters is discussed.

3. A review of existing characterisation tests of Li-ion battery

The components of the ECM are commonly parameterised using characterisation test results, thus performance of the ECM is dependent on characterisation tests. Four characteristics of Li-ion battery play an important role in parameterising ECM components and defining cell's performance. These characteristics are:

- Capacity
- Power capability
- Internal impedance (Z)
- Open circuit voltage (OCV)

In general, battery capacity defines range of the EV, power capability defines acceleration and maximum speed, internal impedance defines maximum power capability, heat generation and SoH of the battery, and open circuit voltage is used to calculate remaining capacity of the battery (SoC). These four characteristics are commonly tested as part of Li-ion battery testing standards for automotive application. Lists of usages of these four characterisation tests in different current standards are shown in Table 2. Although these standard characterisation tests aim to measure the same characteristic of the cell (e.g. pulse power) however the details of the test procedures varies considerably and will be reviewed in this chapter. It can be noted that, EIS test is not as part of any current standards. Although EIS has been used to characterise individual electrodes, it is only recently that researchers identified EIS is a powerful tool giving insight of a complete battery cell; therefore it is included as part of this study.

Table 2: Presence of different characterisation and ageing tests in current automotive test standards

Organizations		ISO	IEC	SAC	US DoE	Freedom CAR
Standards		ISO 12405-1	IEC 62660-1	QC/T 743-2006	Battery Test Manual	Battery Test Manual
Latest release		2012	2010	2012	2014	2003
Characterisation Tests	Capacity	X	X	X	X	X
	Pulse power (P)	X	X		X	X
	EIS (Z)					
	OCV				X (from pulse power test)	X (from pulse power test)

3.1 Capacity test

Capacity test is one of the most common characterisation test techniques used in current standards (Table 2) and by researchers [35, 58, 83, 95, 96]. Capacity test is used to determine total capacity of the cell. This test is performed by completely discharging a fully charged cell.

Lithium ion batteries operate with a voltage window (Figure 14). When cells are discharged, the cell voltage drops, and the cell voltage increases during charge as explained in Section 2.3. While charging the cell, a maximum charge voltage and minimum discharge voltage while discharged are used, defined on a cell basis by manufacturer. Li-ion batteries are charged using the constant current-constant voltage (CC-CV) method as shown in Figure 22. Charge starts with a constant current until the cell voltage reaches the maximum charge voltage V_{max}. The value of constant current is defined to C/3 in ISO and SAC standards; however, other

standards suggest using charge rate mentioned in cell datasheet provided by the manufacturer (Table 3). At this point of charging, cell voltage V_{max} is kept constant and current starts to drop; this is the constant voltage (CV) part of charging. When current drops to a predefined value which is low (e.g. C/30) compared to constant current part it is considered that the cell is fully charged. Among all the standards only SAC mentioned use of C/30 cut-off current. Therefore, when other standards are used, the cut-off current needs to be defined by the user, leading to use of different cut-off current, which will affect the reproducibility of the capacity test results by different user. This clearly indicates potential difference between results using different standards. The fully charged cell is then kept in an open-circuit condition to reach electrochemical equilibrium before discharging to minimum discharge voltage to get the discharge capacity of the cell. Use of 1 h rest period to allow the cell to reach electrochemical equilibrium is same for all standards, which might not be long enough.

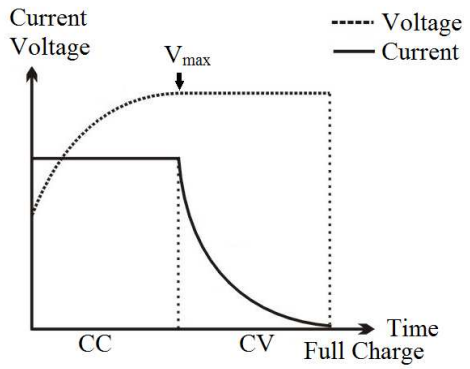

Figure 22: CC-CV charging topology of Li-ion cell

Table 3: Capacity test parameters used in different standards

Standards		ISO 12405-1	IEC 62660-1	SAC QC/T 743-2006	US DoE Battery Test Manual	Freedom CAR Battery Test Manual
Capacity test parameters	Charge current	C/3	Cell datasheet	C/3	-	Manufacturer defined
	Charge cut-off current	-	-	C/30	-	-
	Discharge current	C/3 1C 2C max C	C/3 1C	C/3 1.5C	C/2 – 1.5C	1C Manufacturer defined
	Temperature	-18°C -10°C 0°C 25°C 40°C	0°C 25°C 45°C	-20°C 20°C 55°C	30°C	30°C
	Rest after charge/discharge	0.5 h 1 h	1 h	1 h	1 h	-
	Cooling System	-	-	-	-	-

Theoretically, any battery cell can be discharged using one of the three methods; constant load, constant current and constant power [84]. These three modes of discharge are illustrated in Figure 23.

In constant load mode, load resistance, R_{Load} of Figure 12 (b) is kept constant. In this method, with discharge duration the battery's voltage drops, leading to current and power drop following, $V=IR_{Load}$ and power, $P=VI=I^2R_{Load}$. It is illustrated in Figure 23 (a) and Figure 23 (b). None of the current standards use this mode of discharge for capacity tests.

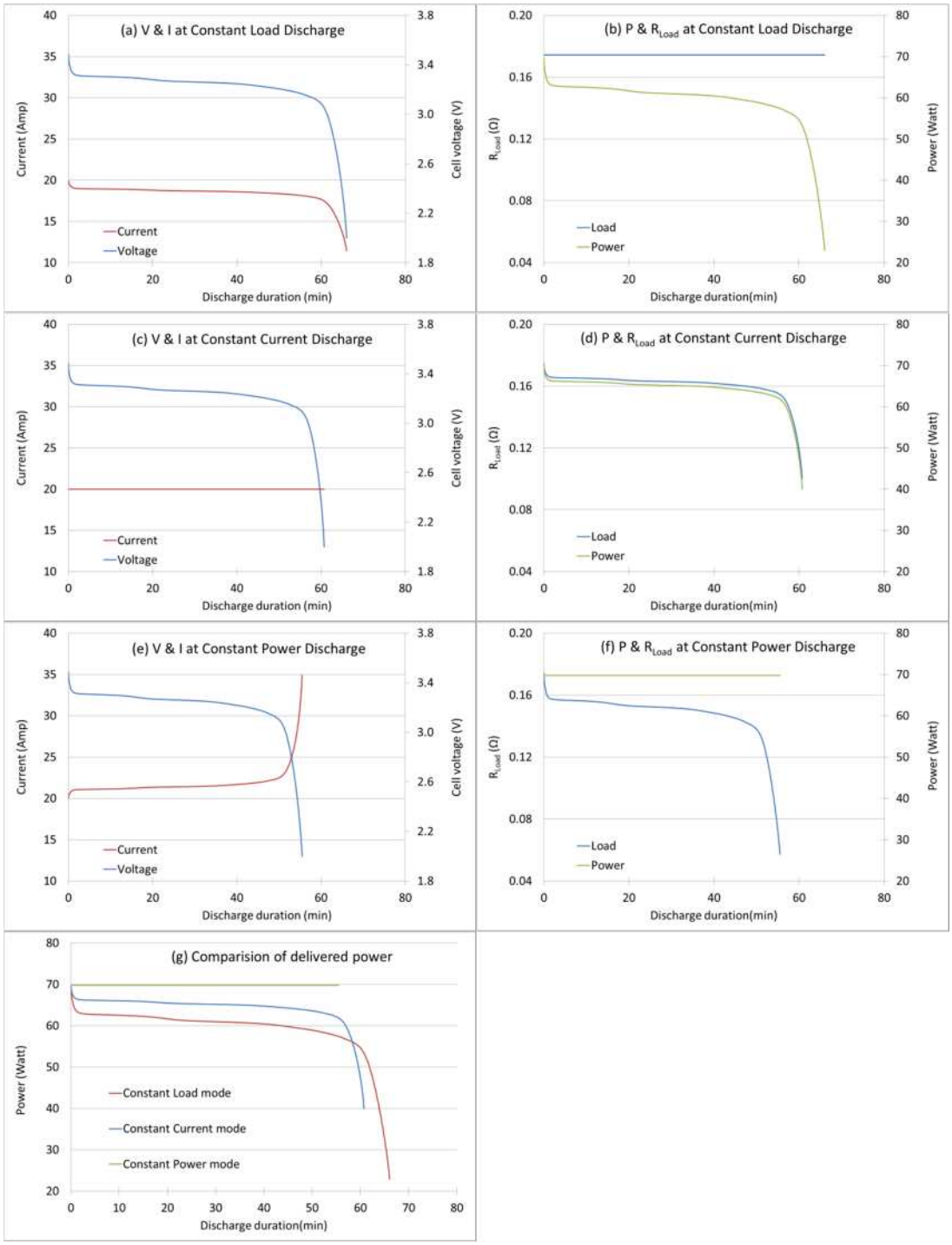

Figure 23: Discharge topologies (a) voltage and current (b) power and load resistance at constant load mode of discharge, (c) voltage and current (d)) power and load resistance at constant current mode of discharge, (e) voltage and current (f)) power and load resistance at constant power mode of discharge, (g) output power comparison among three modes of discharge.

Constant current discharge is used in all current standards. In constant current mode of discharge, discharge current is kept constant regardless of the voltage drop. To keep current constant, load resistance is proportionally reduced with voltage drop. The output power drops in this mode as voltage drops with discharge duration, which is illustrated in Figure 23 (c) and Figure 23 (d). However, power drop is lower than constant load discharge mode (in constant load mode both voltage V and current I drops with discharge duration, but in constant current mode only voltage V drops with discharge duration), which makes it a more aggressive mode of discharge.

In constant power mode of discharge, discharge power is kept constant regardless of voltage and current. This mode of discharge makes it easier to measure capacity in Watt-hours. As voltage drops with discharge duration, current increases to keep discharge power constant. It is achieved by controlling load resistance R_{Load}. It is shown in Figure 23 (e) and Figure 23 (f). For comparison, output power in these three modes of discharge is shown in Figure 23 (g). It can be noticed that in constant power mode of discharge cell is discharged (reach lower discharge voltage) faster (for the same starting current) than other two modes of discharge.

Battery capacity will vary depending on the mode of discharge. With higher discharge current battery voltage will reach to minimum discharge voltage sooner ($V_{cell} = V_{OCV} - IR$, Figure 20). Thus battery capacity will be lowest in constant power discharge mode and highest in constant load discharge mode. Among these three modes of discharge, historically, battery capacity tests are done using constant current discharge (Figure 23 (c) and (d)). For automotive applications, use of constant current discharge capacity tests continued, as reflected in capacity tests used

in current standards [23, 25-27, 97] and capacity tests used by researchers [35, 58, 68, 83, 95, 96]. However, an EV's acceleration and speed is directly related to the power demand of the motor, thus the constant power discharge might be best suited for the automotive application. This thesis will use power demand duty cycle of EV to compare against constant current discharge capacity.

Furthermore, cell capacity is affected by discharge rate [73, 95, 98] and temperature [58, 73, 99]. An example of capacity variation due to different discharge current during constant current discharge is shown in Figure 24 (a). Capacity drops more than 5 % when discharge current is increased from 0.2C to 5C. This is due to the internal voltage drop (at resistance R of equivalent circuit shown in Figure 21) increase with discharge rate. Therefore, the discharge cut-off voltage (V_{min}) is reached earlier. In the current ISO standard four different C rates are suggested to repeat the capacity test (Table 3) which is not reflected in other standards.

An example of capacity variation at different temperature using 1C constant current discharge mode is shown in Figure 24 (b). Capacity drops by 35% when temperature drops from 25°C to -20°C, and capacity increases by 5% when temperature increase from 25°C to 40°C. Because of this reason capacity tests are often done at different temperature regardless of the discharge mode. Five different temperatures from -18°C to 40°C are suggested to repeat the capacity test in ISO standard (Table 3) in contrast to three temperature points used in IEC and SAC standards, and only one temperature (30°C) suggested in US DoE standard, therefore there is a large variation among standards in temperature used.

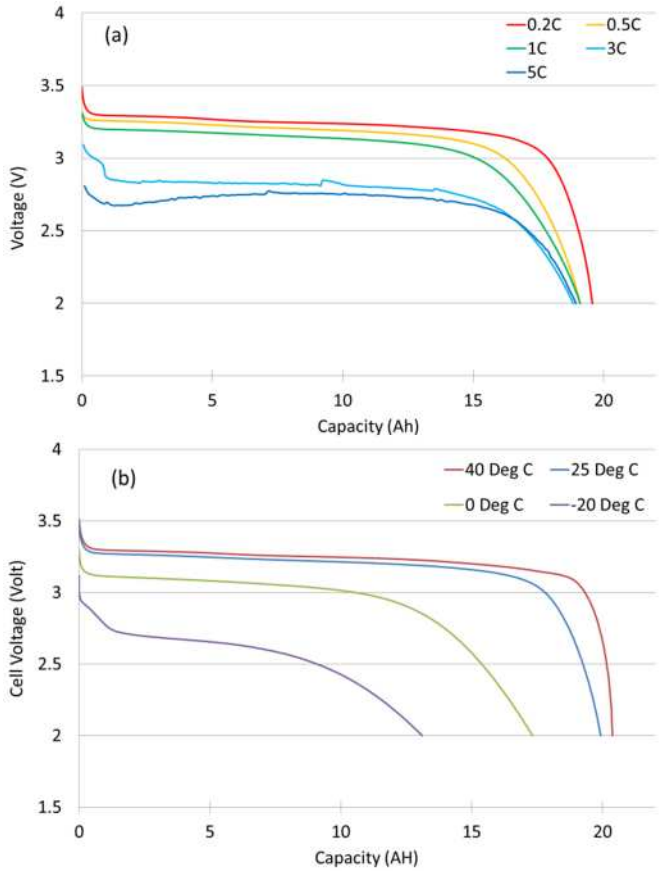

Figure 24: capacity variation of the cell due to variation in (a) discharge current, (b) operating temperature.

It is clear from Table 3 that the capacity testing has a wide variation among different standards. Different standards suggest different C rates and temperatures to do the test. Also a large variation in use of test temperature and C rates among standards exists.

3.2 Pulse Power Test

Power capability is a critical parameter for high power applications. High power capability is generally required for automotive applications to meet both short time acceleration and regenerative braking in a typical drive cycle of an EV. The pulse power test is commonly used to calculate power capability of the battery. Power

capability of a cell is directly related to its internal resistance. Internal resistance defines the cell voltage drop when charge/discharge current applied (V=IR), and a cell has a safe minimum voltage limit. Therefore, maximum charge/discharge current, i.e. power, is limited. This test is performed by applying charge-discharge pulse currents and detecting relative voltage drop. Voltage drop can be divided by the applied current to calculate internal resistance. However, as Li-ion batteries are electrochemical devices, some basic phenomenon of the electrochemical devices needs to be considered while using this technique.

The voltage drop of a Li-ion battery cell due to a pulse current is not linear. An example discharge pulse and relative voltage drop has been illustrated in Figure 25. Voltage drop can be divided into two parts, instantaneous drop which is marked as ΔV_o and slow voltage drop ΔV_1. Here ΔV_o is due to pure ohmic resistance R_o of the battery, which can be calculated by the formula $R_o = \Delta V_o / \Delta I$. The next part of voltage change ΔV_1, is due to electrochemical process of the battery cell. When a cell is at rest, electrochemical processes inside the cell are in equilibrium. Lithium molecules are equally distributed within anode and lithium ions within electrolyte has a stable concentration. When the discharge process starts, the lithium ions from the electrolyte accept electrons from the cathode, and lithium atoms at the anode lose electrons to become lithium ions, and start to move to the cathode through electrolyte. The de-intercalation of lithium at anode has a time constant; therefore, the stable condition changes, which leads to further voltage-drop. Thus, total resistance due to DC current (DCR) is $(\Delta V_o + \Delta V_1)/ \Delta I$. This is the result measured by pulse power test.

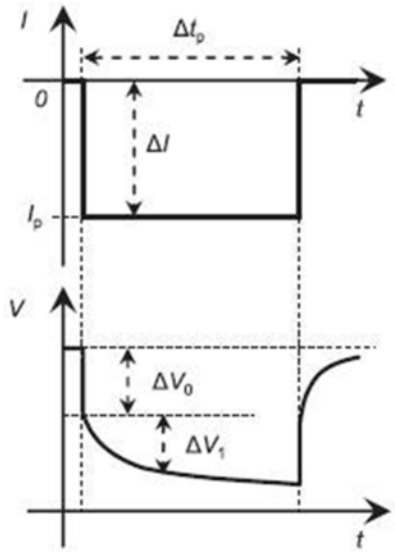

Figure 25: Discharge current pulse and relative voltage drop.

DCR is a strong function of current amplitude of the pulse. The de-intercalation of lithium at the anode and intercalation of lithium at the cathode is highly dependent on current amplitude [100]. Therefore, pulses of different current amplitude, representing up-to maximum discharge power, need to be used for full characterisation of the battery cell.

The pulse power test is commonly used as characterisation test among standards. Li-ion battery test standard for EV published by International Electrochemical Commission (IEC 62660-1) suggest doing pulse power test with different current amplitude ranging from 1/3C to maximum C rate of the battery cell [101]. An example pulse profile from IEC 62660-1 is shown in Figure 26. The 10min rest time in between pulses is to allow the cell to reach chemical stability. This pulse profile is suggested to be performed at different temperatures and SoCs to identify maximum power capability at different operating conditions. The test standard published by U.S. Department of Energy (DoE) have completely different pulse power test which

is generally called hybrid pulse power capability (HPPC) test as shown in Figure 27. It applies a single charge-discharge pulse at 10 different SoC starting from 100% to 10%. Although, it covers wide range of SoC, it does not use different current amplitudes. Furthermore, pulse power test standard published by International Standardization Organization (ISO 12405) have not only different amplitude pulse profile but also different length pulse profile as shown in Figure 28.

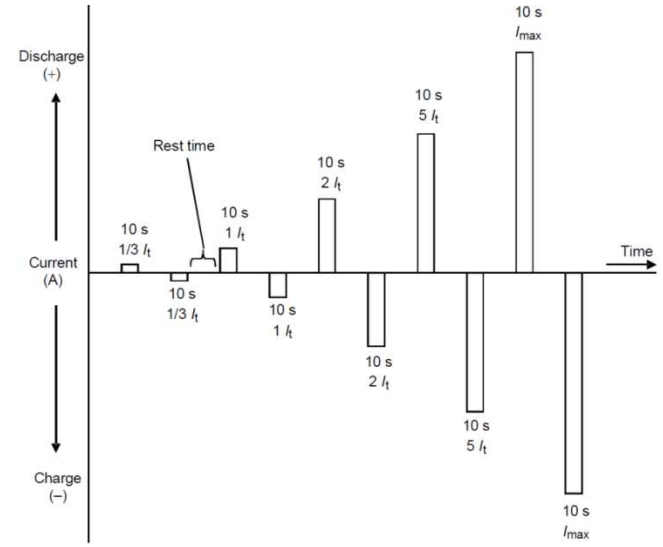

Figure 26: Pulse profile for pulse power test used in IEC 62660-1 test standard [101].

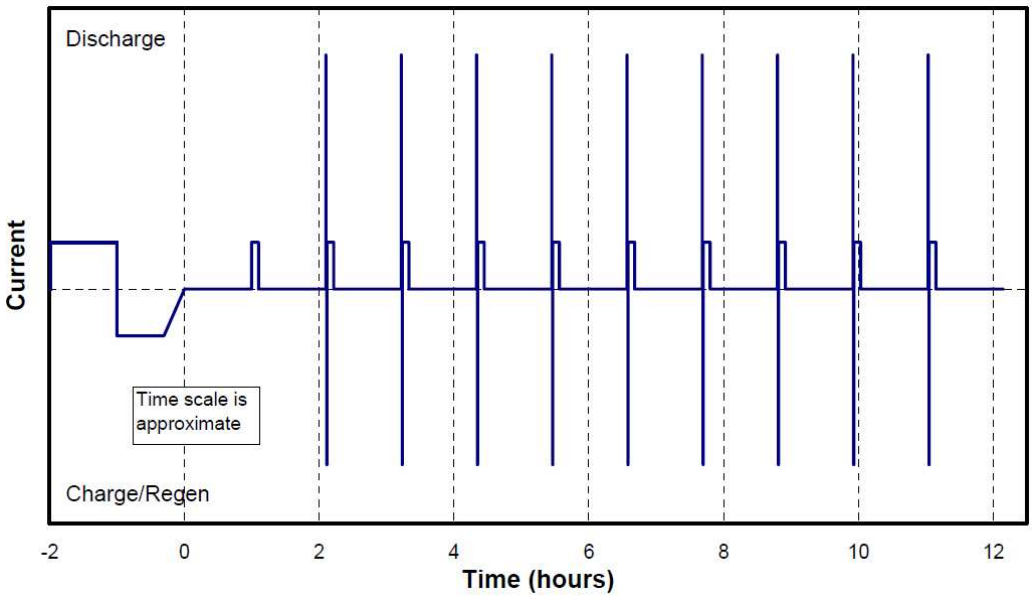

Figure 27: HPPC test profile [102].

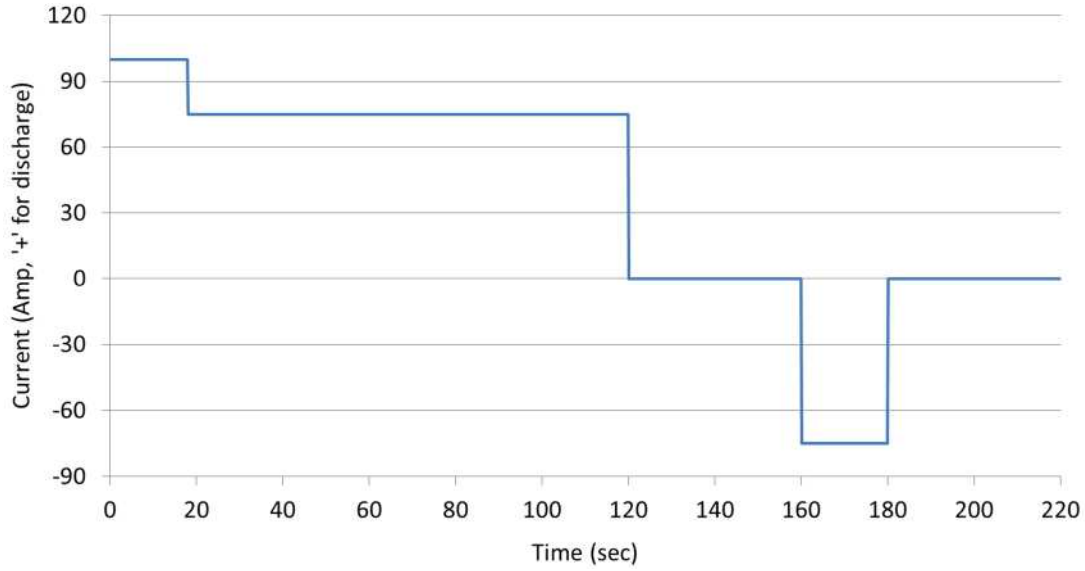

Figure 28: Pulse profile for pulse power test used in ISO 12405 test standard [25].

Table 4: Pulse power test conditions used in different standards

Standards		ISO 12405-1	IEC 62660-1	SAC QC/T 743-2006	US DoE Battery Test Manual	Freedom CAR Battery Test Manual
Capacity test parameters	Pulse amplitude	I_{max} 0.75 I_{max} (I_{max} is maximum current)	C/3 1C 2C 5C 10C Max C	-	1C discharge 0.75C charge	1C discharge 0.75C charge
	Pulse duration	18 sec 20 sec 102 sec	10 sec	-	10 sec	10 sec
	Rest after pulse	40 sec	10 min	-	40 sec	40 sec
	SoC	20 % 35 % 50 % 70 % 90 %	20 % 50 % 80 %	-	100-0 % SoC at 10 % SoC interval	100-0 % SoC at 10 % SoC interval
	Temperature	-25°C -10°C 0°C 25°C 40°C	0°C 25°C 45°C -20°C	-	30°C	30°C

In addition to the three different pulse power test profiles used in different standards there are variance in use of rest period after pulses, number of SoC and temperature the test needs to be repeated as summarised in Table 4. ISO standard suggested

repeating the test at five different temperatures from -25°C to 40°C in contrast to single temperature point (30°C) suggested in US DoE standard. Moreover, US DoE standard suggest performing the test at 10 different SoC while IEC standard suggest only three different SoC points.

A standard way of pulse power test among the existing standards is absent. Use of different rest period after the pulses and pulse duration might require further attention. Although the large variation of pulse power test exists, HPPC test and pulse profile of IEC standard are widely accepted by researchers.

3.3 Electrochemical Impedance Spectroscopy test (Impedance)

Power capability of li-ion cell mainly depends on the electrode polarisation, which in turn depends on the rate of lithium intercalation and de-intercalation at the electrodes. As a result, studies have mainly focused on decreasing electrode polarisation at high charge/discharge rates and low temperature [70, 71, 73]. The lower degree of electrode polarisation was achieved through deeper understanding of the lithium intercalation/de-intercalation process that takes place during charge and discharge [92, 103]. As explained in Section 2.3, lithium intercalation/de-intercalation is a series of complex processes including lithium ion diffusion in the electrolyte, migration through the solid electrolyte interface (SEI) layer, charge transfer through the electrode/electrolyte interface and solid state diffusion in the bulk of active material as shown in Figure 10. The voltage drop detected in pulse power test is the combined effect of these complex processes, therefore unable to give insight into individual mechanisms. Investigation of these processes

individually can be achieved by using electrochemical impedance spectroscopy (EIS). As each process has a different time constant or time domain or frequency of excitation [89, 91], EIS allows for the separation of these processes [88].

EIS provides a measurement of the internal impedance of the battery over a frequency range. This is in contrast with pulse power test, where internal resistance is measured using DC current; in EIS test an exciting voltage E_t (as shown in Equation (8) is applied to the sample which in turn generates very small AC current I_t of same frequency. The resultant current depends on the voltage signal applied and on the impedance of the cell. In Equation (9), the additional term $\emptyset$ is the phase change of current which is related to the impedance of the cell. The impedance is calculated by simply dividing voltage (Equation (8)) with current (Equation (9)) as shown in Equation (10).

$$E_t = E_0 sin(\omega t) \tag{8}$$

$$\omega = 2\pi f$$

$$I_t = I_0 sin(\omega t + \emptyset) \tag{9}$$

$$Z(\omega) = \frac{E_t}{I_t} = \frac{E_0 \sin(\omega t)}{I_0 \sin(\omega t + \emptyset)} = Z_0 \frac{\sin(\omega t)}{\sin(\omega t + \emptyset)} \tag{10}$$

The frequency of the applied excitation voltage signal is varied over the frequency range (e.g. 10 kHz to 10 mHz) and impedance is measured at a range of frequencies (commonly known as frequency sweep). This method of EIS test is known as potentiostatic mode. EIS also can be performed by applying fixed current signal and measuring change of voltage; which is known as galvanostatic mode. Both of the techniques are used by researchers, however galvanostatic mode is more suitable to

study low impedance samples like lithium-ion cells, due to the maximum current limitation of the equipment, typically 2-20 Amp [91].

Depending on the RC time constant of different electrochemical processes, impedance varies at different frequency. The impedance $Z(\omega)$ in Equation (10) has a real and imaginary part. To represent the impedance, the real part of the data is plotted in 'x' axis and imaginary part in 'y' axis of a graph; which is commonly known as 'Nyquist Plot'. An example Nyquist plot of a RC circuit is shown in Figure 29; to be noticed the 'y' axis is negative and each point is the impedance at a particular frequency. In this figure, far left is the starting of frequency sweep at high frequency and far right is the end of sweep at low frequency.

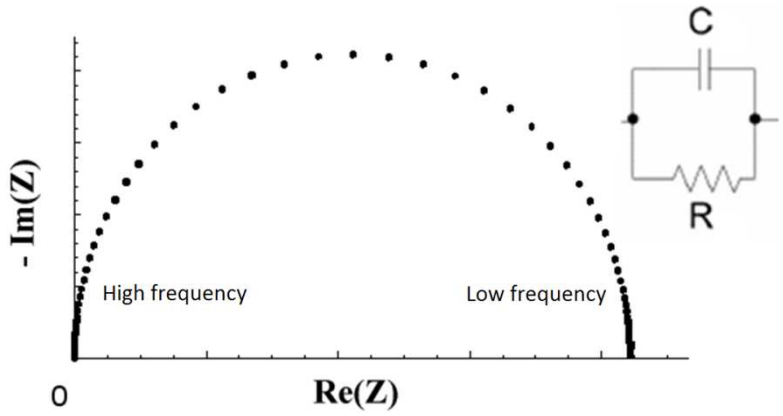

Figure 29: Nyquist plot of a RC circuit.

Figure 30 shows an example Nyquist Plot of a Li-ion battery cell. The Nyquist plot can be divided into three parts. The high frequency region (usually ≥1 kHz), or below 'x' axis region, is caused by the ionic conduction through the electrolyte and separator and electronic conduction through the sensor wires of EIS system [86, 104]. The mid-frequency semi-circle (usually ≤1 kHz and ≥100 mHz) is attributed to

charge transfer and the electrochemical double layer i.e. kinetics of the reactions [80, 81, 92, 93]. Depending on the age of the cell, a second semi-circle can be observed which originates from the SEI layer [92, 94]. The low frequency part (≤100 mHz), usually characterised by a 45° slope, represents the diffusion limited region, also known as finite length Warburg impedance [93, 105, 106]. Electrode materials used to manufacture Li-ion batteries have a crystalline structure which allows for lithium ions to shuttle through the materials during charge and discharge (Figure 10). The movement of ions within the crystalline structure is governed by solid state diffusion [107]. As ions diffuse through the material to the centre of the particle, their diffusion path is limited. This process is depicted at the very low frequency end of the Nyquist plot by a straight line with a 45° slope. It should be noted that, when the low frequency measurement is not performed, there is a possibility that the large semicircle in Figure 30 will not be visible. Therefore, the small semicircle will be incorrectly attributed to the double layer.

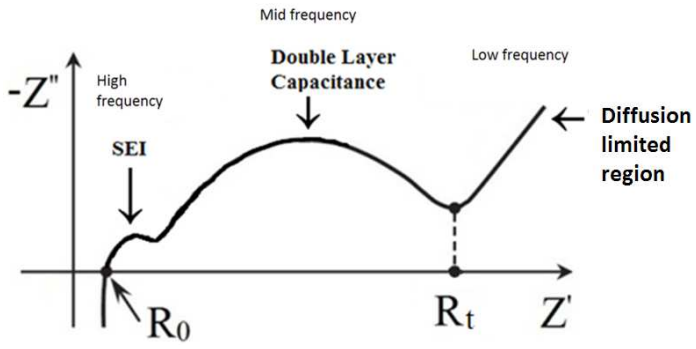

Figure 30: Example EIS plot.

To analyse EIS test results usually an equivalent circuit is used as shown in Figure 21. However, for solid electrodes, as is the case for Li-ion batteries, constant phase elements (CPE) are used as a replacement for capacitors. CPE accounts for the

inhomogeneity of the electrode surface such as roughness [81, 108]. In case of the presence of CPE, the semicircles shown in EIS result in Figure 30 will be suppressed, which is a perfect semicircle in case of a capacitor. The modified equivalent circuit commonly used to explain EIS results is shown in Figure 31. The series inductor L_1 is used to explain the inductive behaviour at high frequency. Therefore, the Equation (10) can be rewritten for the updated equivalent circuit (Figure 31) as Equation (11).

$$Z(\omega) = j\omega L_1 + R_0 + \frac{1}{j\omega CPE_1 + {}^{1}/_{R_1}} + \frac{1}{j\omega CPE_2 + {}^{1}/_{R_2}} \tag{11}$$

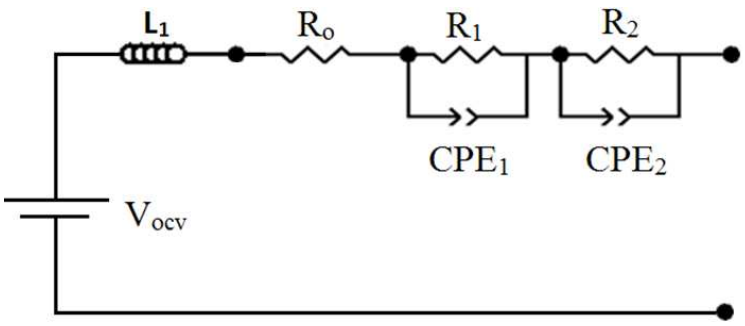

Figure 31: Updated electrical equivalent circuit of Li-ion cell.

All of these components behave differently at different frequencies. For example, with increase of frequency, the impedance of a CPE decreases. If the frequency is high enough, the CPE can short circuit the parallel resistance, thus causing the parallel branch to be temporarily removed from the circuit. When the curve crosses the x-axis, the frequency is such that all the parallel strings containing a CPE are shorted. Therefore, only the pure ohmic resistance component of the system (R_o) remains (considering very low inductance). At this particular point, both the applied current and voltage response are in phase with one another (though signals may

differ in amplitude). The origins of R_o are mainly the resistance of the electrolyte and the current collectors [62, 80, 93, 109].

Similarly, at low frequency, the capacitor acts as an open circuit and can be removed from the circuit. As a result, the impedance corresponds to the total resistance of the cell i.e. ohmic resistance and electrochemical impedance (charge transfer resistance at the electrode/electrolyte interface), and Equation (11) can be re-written as Equation (12).

$$R_T = R_0 + R_1 + R_2 \tag{12}$$

Although EIS test has the advantage of giving insight of electrochemical mechanisms of the cell, it is not included in any current test yet. However, it has been widely used by researchers to characterise Li-ion battery cells [40, 62, 83, 95, 110], although little consistency in test procedure exists. Electrochemical processes like lithium intercalation/de-intercalation, lithium diffusion through SEI, ion transport properties of electrolyte, are temperature and SoC dependent. Researchers have used EIS to study these electrochemical processes at different temperature and SoC. For example, at lower temperature, ion transport properties of electrolyte and electrical conductivity of other materials will decrease, which will be reflected as increase of R_o. Also, double layer capacitance and capacitance from SEI will decrease with temperature, i.e. increase of impedance, because of change of dielectric properties of separator and change of kinetics of lithium ions, this relationship has been reported by the researchers previously [62, 80, 88, 89, 92, 93, 111, 112]. Also, with the change of SoC there is no change of electrolyte or change of electrical conductivity of other materials involved. Therefore it is expected R_o will

not change with SoC. However, with increase of SoC cell voltage increases, also electrode properties changes, leading to increase of the capacitance, i.e. decrease of impedance. Therefore, cell impedance will rise when cells are at lower SoC; again, this relationship has been reported by the researchers [62, 80, 81, 105, 113].

EIS has been identified as an effective tool for Li-ion battery characterisation in laboratory and on-board diagnosis, which appears well understood by the researchers. However, for automotive application it requires further attention to ensure repeatable and reproducible results, which will be discussed in Section 4.2.

3.4 Open Circuit Voltage Test

The OCV is the battery thermodynamic equilibrium potential when not under a current load. The OCV as a function of SoC is an important characteristic for ECMs. It acts as an ideal but variable (e.g. with SoC) voltage source in the model to which over-potential is added by the remaining resistor and capacitor elements of the ECM. Conversely, the SoC of a cell, which is crucial for a vehicle Battery Management System (BMS), can be determined if the cell's OCV is known. An example of OCV vs SoC plot is shown in Figure 32. In a simple SoC estimation, using this plot, SoC value can be deduced from known OCV of a cell. More complex versions of this simple representation have been reported in recent literature [114-118], which demonstrate the importance of an accurate OCV for SoC estimation.

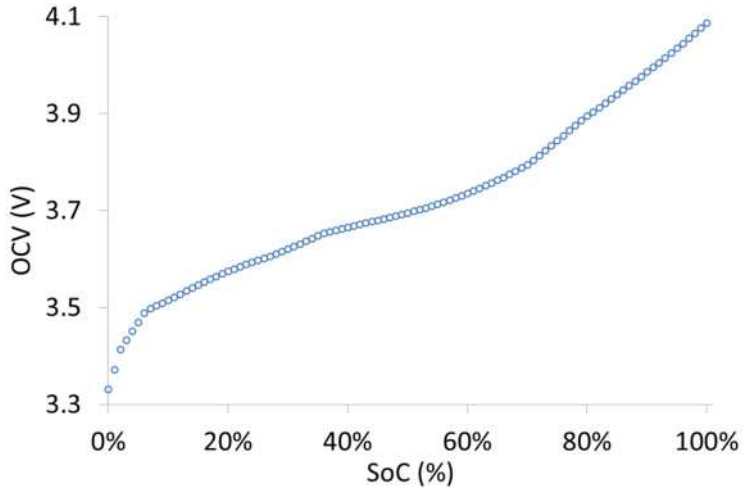

Figure 32: Open circuit voltage at different SoC of a Li-ion battery cell.

Although it is an important parameter, in current standards there is no stand-alone OCV test [23-26]. Only Freedom CAR and US DoE standards suggest calculating OCV data from HPPC test [102]. HPPC test procedure is illustrated in Figure 27. As pulse current is applied in 10 % SoC intervals from 100% to 0% SoC, OCV is recorded just before the pulse current is applied. Therefore, only 11 OCV measurements will be recorded. There are two concerns regarding this OCV measurement procedure; firstly, 11 measurement points do not provide adequate resolution of a full OCV vs SoC plot as shown in Figure 32. Secondly, the 1 hour rest period is used after SoC adjustment which might not be long enough for the cell to reach electrochemical equilibrium.

Nevertheless, researchers have developed different test procedures to generate OCV vs SoC plots. A possible approach to estimate a cell's open circuit voltage is to discharge and charge the cell with a low current (usually C/25), and average the measured charge and discharge voltages [117, 119, 120]. A low current is used to minimise any diffusion limitations. However, even with a low discharge/charge

current the cell will experience kinetic contributions when it is nearly discharged or fully charged, leading to a high voltage drop [115, 121]. As such, the measured voltage can then no longer be assumed as the cell's OCV, as it is under some load.

An alternative method is to discharge/charge the cell incrementally (e.g. 4 % SoC intervals) followed by a rest period to allow the cell dynamics to relax and reach equilibrium [115, 122-124]. The voltage recorded from this method, also known as the incremental OCV method, is a better estimate of the cell's OCV since the electrode kinetics are allowed to reach equilibrium. The relaxation time depends on the SoC increment, for example in [115], 6 minutes, 24 minutes and 2 hour rest intervals are used for SoC increments of 0.5 %, 1 % and 5 % respectively, in HPPC test 1h rest period is suggested after discharging 10 % SoC. Following this procedure OCV can either be measured while the battery is incrementally charged (OCV_{c}) from a fully discharged state or incrementally discharged (OCV_{d}) from a fully charged state. The OCVs then associated with the corresponding SoC as shown in Figure 32. This approach is valid for analysing the discharge and charge OCV characteristics independently.

3.4.1 OCV hysteresis

The measured OCV depends on how it is measured, by charging or discharging; it could be different depending on the method. Therefore, two SoC curves can be obtained for charge and discharge. This variation of OCV is known as OCV hysteresis [124, 125]. An example of OCV hysteresis has been shown in Figure 33. The charge-discharge OCV curves were obtained by the incremental OCV method.

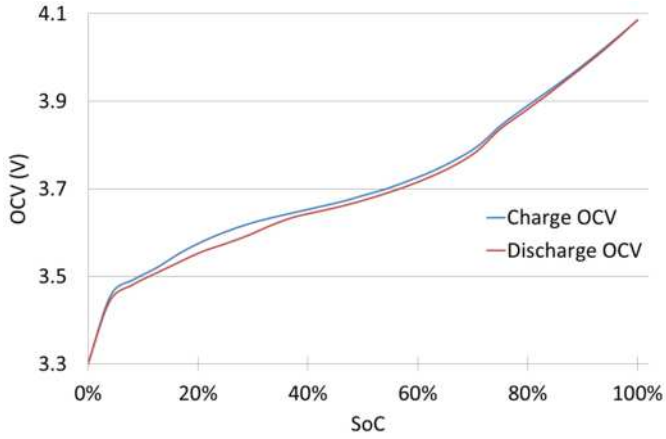

Figure 33: Hysteresis between OCV curves (of NMC cell) obtained by charging the cell in steps from 0% SoC to 100% SoC and discharging the cell in step from 100% to 0% SoC.

Cells with lithium iron phosphate electrodes or nickel hydroxide electrodes are known to have stable hysteresis [114, 121, 126]. Hysteresis in a battery corresponds to the existence of several possible thermodynamic equilibrium potentials at the same SoC of the cell. Positive electrodes with lithium iron phosphate as the active material are known to exhibit a hysteretic phenomenon [123, 127]. Srinivasan and Newman [121] provided an explanation for hysteresis based on the existence of a lithium rich and lithium deficient phase within an active particle. They termed the explanation as the *path dependent shrinking core model*, whereby during discharge a shrinking particle core of Li_yFePO_4 and a growing outer crust of $Li_{(1-x)}FePO_4$ occurs, while during charge a shrinking core of $Li_{(1-x)}FePO_4$ and a growing crust of Li_yFePO_4 occurs (considering mole fractions x and y are close to zero) as shown in Figure 34. As a consequence of shrinking core, the juxtaposition of the phases at 50 % SoC depending on immediate history can be clearly seen. The corresponding chemical potential of the particle at this point, and therefore open circuit potential, will be different. With a further charge, the composition of the core can be different

even at the same SoC and same immediate history (in this case it is charge). Therefore, depending on this two-phase particle composition there will be OCV hysteresis.

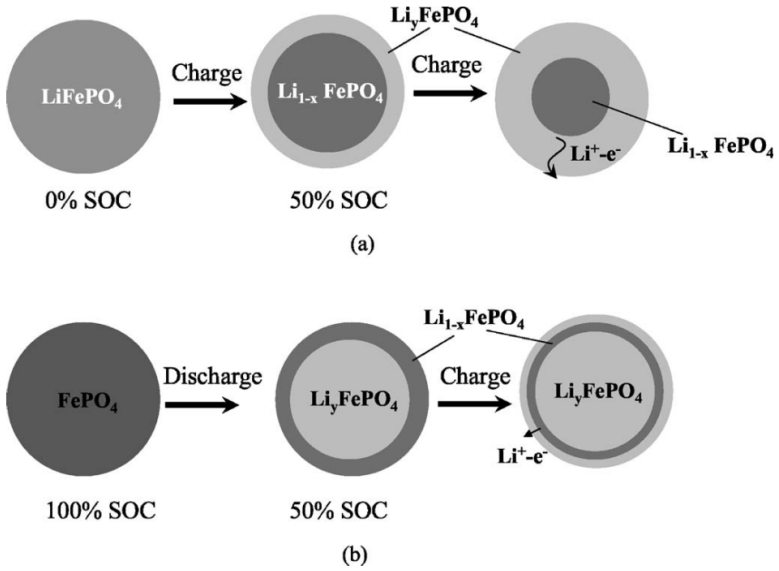

Figure 34: Illustration of path dependence shrinking core model as proposed by Srinivasan and Newman [121]. SoC of LFP electrode was adjusted to 50 % SoC by (a) charging from 0 % SoC and (b) discharging from 100 % SoC. The change of the core or further growth of new shell is shown due to further charge from 50 % SoC in both cases.

More recent work in explaining hysteresis has extended the single particle two phase transition of $LiFePO_4$. Dreyer *et al.* [127] argued that if the active material particle has a non-monotonic chemical potential with regards to its lithium mole fraction and in the presence of many such particles in the positive electrode, the chemical potential of the electrode will be different at the same SoC depending on the path taken to reach the particular SoC. In comparison to the path dependent shrinking core model a notable revision is the interconnectedness of many particles with a non-

monotonic chemical potential function. While in the former explanation a particle is assumed to be stable when it has reached its inhomogeneous two phase state (regions of low and high lithium mole fraction within the particle), in the latter the particle reaches a homogeneous stable state by distributing the lithium ions to neighbouring particles and decreasing its chemical potential during charge; similarly an inhomogeneous particle will admit lithium ions from neighbouring particles during discharge. This interchange of ions occurs when the mole fraction of an inhomogeneous particle reaches its maximum or minimum chemical potential (non-monotonic potential function) leading to different overall chemical potential, and therefore open-circuit potential of the electrode depending if it is charging or discharging. Therefore, while battery being charged or discharged, to estimate OCV by BMS, an accurate hysteresis data is crucial.

Although, OCV hysteresis is important for OCV measurement and thus operation of BMS, none of the current standards include any OCV test procedure. As OCV hysteresis is dependent on the accurate measurement of the OCV, a standard OCV test procedure is also essential.

3.5 Summary

Four characterisation tests have been reviewed in this chapter. Capacity test with constant current is commonly used to assess battery capacity. Existing standards suggest to measure capacity with a matrix of temperatures (e.g. -10 °C, 0 °C, 25 °C, 40 °C) and different constant current value (e.g. C/10, C/3, 1C, 3C). Battery capacity was historically measured in Amp-hours (Ah), which continued in capacity test procedures for automotive application. However, measure of battery capacity in

Watt-hours could be more appropriate for automotive application where energy is more important and will be further discussed in Section 4.1.

Internal impedance of the battery is an important parameter, as it indicates physical and electrochemical status within the cell and its power capability. The pulse power test directly measures the power capability of the cell. Although three different types of pulse power test present in existing standards, the HPPC and pulse profile used in IEC standard are widely accepted to measure power capability and DCR (real part of impedance). However, DCR fails to provide insight to the battery's electrochemical and physical status. For this reasons pulse power test will not be primarily investigated as part of this thesis. On the other hand, EIS directly measures impedance of the battery cell at a wide range of frequencies and electrochemical and physical processes within the cell are separated in the frequency domain. Although, EIS has been widely used by electrochemists, it is a fairly new technique (compared to pulse power and capacity test) to characterise li-ion cells for automotive applications. Therefore, further investigation of EIS test for automotive application will be performed later in this thesis.

Though OCV is a common parameter of ECM; existing standards fail to provide an adequate measurement. The OCV test procedures currently being used employ a very slow rate (e.g. C/25) charge-discharge or discharge the cell in steps. Slow rate charge-discharge is not ideal due to inclusion of kinetic contribution. OCV measured by step discharge exclude kinetic contributions; however, are not well developed yet e.g. little research has been done on requirement of the length of rest period. Further research with current issues of step OCV test will be discussed in Section 4.3.

4. The gap between automotive requirements and current testing procedures

The existing characterisation test procedures and inconsistency among different standards have been discussed in the previous chapter. In addition to the inconsistency, existing test procedures fails to provide the accurate knowledge of li-ion battery performance in real world driving and charging scenarios of EVs. Inconsistency and accuracy of characterisation techniques also a major issue for academic researchers, invalidating actual knowledge contribution reported using characterisation techniques. This chapter aims to highlight the requirement of automotive application and academic researchers, and recognise the existing gaps in knowledge of characterisation techniques.

4.1 Capacity test

Among automotive OEMs, currently it is a common practice to perform capacity tests with different discharge rates at different temperature to predict available electric range (i.e. battery capacity) at different speeds (i.e. discharge rate) and climates (i.e. different temperature). Battery capacity for different driving and climate scenarios are commonly used by BMS to estimate SoC, which are in turn used to estimate driving range (fuel gauge of the EV). Battery SoC is estimated using a simple equation shown in Equation (13).

$$SoC = SoC(t_0) - \frac{1}{Total\ Capacity}\int_{t_0}^{t_f} I\ dt, \tag{13}$$

Energy, typically discussed in terms of energy density (Wh/l) or specific energy (Wh/kg), is important because it translates directly into vehicle range. Remaining energy in Watt-hours, which can be expressed as State of Energy (SoE), analogously to State of Charge, can be defined as

$$SoE = SoE(t_0) - \frac{1}{FBE}\int_{t_0}^{t_f} P\, dt, \tag{14}$$

is more appropriate for RDR estimation. FBE denotes the full battery energy measured in Watt hours, P is the power delivered in Watts and t is time. According to *Zhang et al.* [128] the RDR is then estimated by

$$RDR = F(\gamma) \cdot \frac{RBE}{FBE} \tag{15}$$

where, RBE is the remaining energy and F is the full battery driving distance under driving conditions γ (e.g. rolling resistance, parasitic load, road gradients).

Total battery energy in Watt-hours has not received the same attention as total capacity in Amp-hours. In current standards, it is mostly absent and also not commonly used by researchers as a characterisation technique. Capacity testing with different C rates and temperature are suggested in standards. However, large variation of range estimation by existing EVs have been reported [14, 129, 130]. This could be due to the fact that SoE, not SoC, translates directly into vehicle range. This thesis will investigate advantages to BMS of using Watt-hours over Amp-hours as part of capacity testing.

Use of constant current discharge is appropriate for Li-ion batteries used for the applications where demand does not change dramatically e.g. laptop, uninterruptable power supply (UPS). However, where Li-ion batteries are used as the main source of power, their capacity test needs to be matched with their power demand profile. It is reflected in the capacity test profile for Li-ion batteries used in mobile phones [131]. Mobile phones have high power demand during calling and low power demand during standby period. Therefore, mobile phone battery's capacity test profile has variable power demand (high current pulses). Similarly, in real world operating conditions of an EV, a battery will not be discharged continuously and there will be no fixed load, current or power. Batteries can also be charged in an event of regenerative braking which can happen between large discharge demands. This makes automotive application different from other applications (e.g. portable electronics) of Li-ion battery. Therefore, intermittent discharging using real world drive cycles can provide a more realistic discharge capacity value of the battery; from a vehicle's perspective. However, it is not reflected in capacity tests used in current standards [23, 25-27, 97] and capacity tests used by researchers [35, 58, 68, 83, 95, 96], which assumes a constant current. An example of a real world duty cycle is shown in Figure 35. Negative current represents discharge and positive represents charge current. For the majority of time of this duty cycle the battery was being discharged. Peaks of discharge power represent acceleration and peaks in charge power represent braking of the vehicle. For a realistic capacity test, a fully charged cell can be discharged to minimum voltage using a longer duty cycle or repeating the duty cycle. This thesis will introduce a vehicle's duty cycle to compare against constant current capacity data of a vehicle, obtained using an international standard.

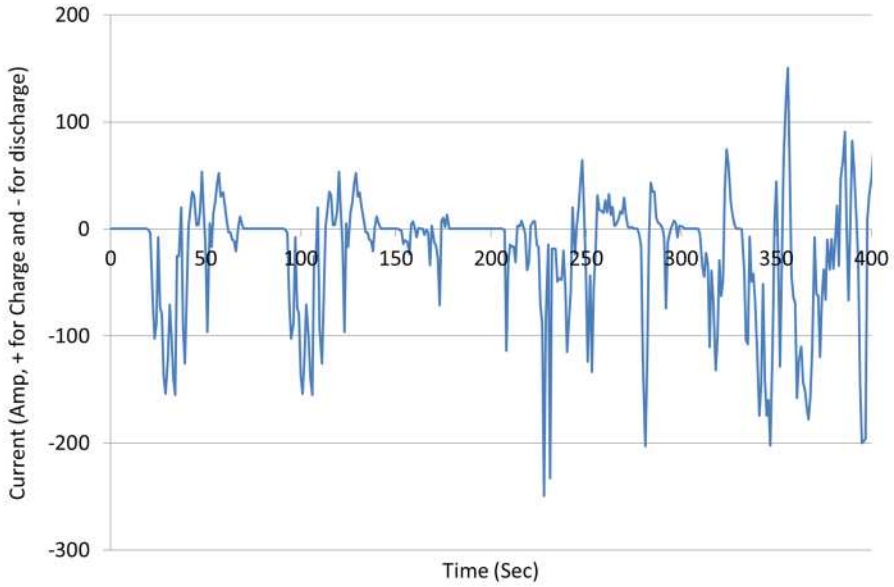

Figure 35: Current demand to a cell, of a vehicle's battery pack, for 400 second of city driving.

Battery capacity decreases with increased discharge rate (as shown in Figure 24 (a)) [30, 95]. Therefore, it is common practice among OEMs to de-rate the battery's maximum discharge current, toward the end of discharge (lower SoC) to get access to any remaining capacity [132]. For example, in Figure 24 (a) while the battery is being discharged at maximum 5C current and cell voltage reaches close to 2 V if the battery is de-rated to 0.2C it will allow 5 % more capacity to be discharged. Therefore, the speed of the vehicle will be limited (maximum current in duty cycle as shown in Figure 35 will be limited to 0.2 C) when the battery is de-rated but it will allow the driver to drive the vehicle 5 % more of its full range, which might be long enough to reach the base or a charging station. The current capacity testing procedure does not include de-rating of maximum discharge current of the battery. This gap will be further investigated in this thesis.

Simple constant current capacity tests are well developed; however, they are not adequate for automotive applications. The following issues need to be addressed within capacity tests for automotive applications:

1. SoE which was largely ignored over SoC, and requires further investigation to improve RDR estimation.
2. The de-rating technique used to maximise RDR, requires to be introduced into capacity testing.
3. Validation of capacity testing requires performing using dynamic discharge profile (e.g. duty cycle of EV).

4.2 EIS test

As explained in Section 3.3, EIS can provide insight to electrochemical processes within the cell. Therefore, several studies have investigated the use of EIS to estimate state of charge (SoC) and state of health (SoH) in electric vehicles [81, 82, 104], ageing [58, 62, 83, 95, 99] and electrode properties [86, 88, 89, 93]. When the on-board SoC and SoH measurement system use EIS, there is limited control over short-time previous history, i.e. rest period after last use and current rate. Therefore, it requires a robust test methodology or a calibration technique to ensure reproducibility of the results regardless of previous history. On the other hand, for the ageing tests, where particular ageing mechanism(s) are accelerated and tested, it is desirable to minimize any source of variation of the test results (except ageing), therefore, repeatability and reproducibility are crucial.

Although, researchers have used EIS extensively, limited attention has been paid towards understanding the effect of relaxation time prior to performing an EIS measurement. When the electrical load is disconnected, the polarisation of the cell ceases and as a result, the cell impedance and voltage of the cell changes [133, 134]. Herein, this effect is referred to as relaxation of the cell and is mainly caused by relaxation of ions within the double layer, electrolyte ionic concentration gradient redistribution and solid state diffusion of lithium atoms within the bulk of the materials. Previous studies that have employed EIS techniques have recognised that a relaxation period is prudent. Several EIS studies on Li-ion batteries were conducted after various relaxation periods ranging from several minutes to several hours following the removal of an electrical load [62, 86, 89, 92, 93, 104, 113]. However, these studies do not offer any scientific explanation nor have they systematically studied the influence of relaxation times on the stability of impedance measurements. Previous short-term history was considered prior to EIS measurements by *Waag et al.*[62], but they, too, did not account for the relaxation time as a possible influence on their results. Another work [135] presented the influence of relaxation time on EIS measurement. However, they did not offer any electrochemical explanation or any theory regarding the nature of the influence of relaxation on EIS. The relaxation period is not only important for EIS measurements but also other characterisation procedures like pulse power test and OCV test, where cell voltage is measured after cell reach electrochemical equilibrium. Therefore, the knowledge of the effect of relaxation on EIS response will also be applicable to pulse power test and OCV test to address the requirement of minimum rest period after charge/discharge pulse.

To ensure repeatability and reproducibility of the EIS measurement, in a vehicle or laboratory environment, it is crucial to develop suitable experimental protocols which minimise measurement variability. Therefore, it is essential to understand the effect of cell relaxation on the EIS response and incorporate this understanding into testing protocol which ensures repeatability and reproducibility of the EIS measurements. Following issues will be investigated as part of EIS test procedure in this thesis:

1. Investigate short-term effect of cell relaxation through EIS
2. Investigate long-term effect of cell relaxation through EIS

4.3 OCV test

Inaccurate OCV and OCV hysteresis data will lead to an inaccuracy in SoC estimation. An inaccurate SoC will be reflected as inaccurate range estimation, leading to decrease of user satisfaction/trust; which in turn is a potential business risk to the OEMs. On the other hand, the inaccuracy in SoC can lead to shift of operating SoC window of EV's battery packs. To maintain minimum available power assist and regenerative capability, HEV battery packs operate within a SoC window, avoiding high and low SoC [136]. A SoC window is also used for other types of EVs to extend battery life and avoid safety failures due to overcharge and over-discharge [136, 137]. An inaccurate measurement of SoC can shift/change the operating SoC window which will be reflected as short term (e.g. regenerative power capability) and long term performance drop (e.g. decrease of expected battery life). Therefore, it is important that the ECM used by BMS should incorporate an accurate OCV.

In the step OCV test procedure, OCV is measured while the battery is incrementally charged (OCV_{c}) from fully discharged state or incrementally discharged (OCV_{d}) from fully charged state. The OCVs can then be associated with the corresponding SoC. SoC is calculated from the charge (Q_c) or discharge (Q_c) capacity that has been added to or removed from the cell. The capacities are defined as:

$$Q_c(t) = \int_0^t I_c(t)dt \tag{16}$$

$$Q_d(t) = \int_0^t I_d(t)dt \tag{17}$$

In Equations (16) and (17) I_c and I_d are charge and discharge currents and are assumed positive in value. Battery SoC is assumed to be 0 % when the cell voltage (not OCV) reaches the minimum discharge voltage and 100 % at the end of CV part of charging. Depending on the charge/discharge conditions e.g. rate, temperature, intermediate rest period, age etc. Q_c/Q_d can be different. From the origin of OCV (as explained in Section 2.3) it is expected that OCV will be directly related to the capacity not the empirically determined SoC. This will be investigated further and reported in Chapter 8.

To investigate OCV hysteresis, OCV_{c} and OCV_{d} are required to be compared against a common capacity axis, instead of two separate capacity axes Q_c and Q_d. Therefore, an initial condition can be introduced and the current I can be assumed positive for discharge and negative for charge. The common capacity scale can be identified as the remaining capacity (Q_r), is now defined as:

$$Q_r(t) = Q_r(0) - \int_0^t I(t)dt \tag{18}$$

$$I(t) > 0 \quad \text{Discharge}$$

$I(t) < 0$ Charge

When OCV_{c} and $\mathrm{OCV_d}$ curves are plotted against the common axis, Q_r, an erroneous hysteretic behaviour may be observed. The apparent hysteresis artefact arises due to the testing procedure and in the assumption that the remaining capacity is zero ($Q_r(0) = 0$) at the end of the discharge prior to the start of the OCV_{c} test. For example, the cell needs to be discharged prior to the OCV_{c} characterisation test, for which a 1C constant current discharge can be performed up to the cell cut-off voltage V_{min}. The test is terminated and first OCV is measured as the starting value of the OCV_{c} test and the remaining cell capacity (Q_r) is assumed zero. In comparison, during the OCV_{d} test, diffusion limitations are reduced as the cell is discharged incrementally to V_{min}, and this allows for more capacity to be removed before the cell reaches V_{min}. Later in this thesis (Chapter 8) will be demonstrated the variation of discharge capacity with different step sizes. The remaining cell capacity (Q_r) will then again be assumed zero (since the cell reached V_{min} for the OCV_{d} test) however, the measured OCV value after similar rest will be lower (due to more capacity removal) in comparison to the starting value of the OCV_{c} test. Thus, when plotting OCV_{c} and OCV_{d} against remaining capacity an offset between the curves will be present, invalidating any true hysteresis assessment. Also, this phenomenon will have significant effect on repeatability and reproducibility of the OCV_{c} and OCV_{d} curves. However, researchers reporting OCV and OCV hysteresis [114, 115, 121-125, 127, 138], did not consider this phenomenon. Therefore, a robust methodology to assess OCV and OCV hysteresis is missing; consequently, an erroneous assessment of OCV and OCV hysteresis could be present historically.

In addition to that, active material particles with a non-monotonic chemical potential (as explained in Section 3.4.1) are expected in many intercalation battery systems and not only restricted to lithium iron phosphate electrodes. As such, a certain magnitude of hysteresis could also be present in other insertion electrochemical systems, which is yet unknown in the scientific community. As explained in Chapters 1 and 2 not only LFP, but also other Li-ion battery chemistries also considered for automotive applications, therefore it is important to fill this gap in knowledge.

Automotive application requires a wide range of operating temperature and theoretically battery OCV is dependent on temperature (Section 2.3 and Equation (6)). However, *Pattipati et al.* concluded no change of OCV-SoC relationship with temperature [117]. Also, higher level of OCV hysteresis with lower current rate has been reported previously by *Roscher et al.* [124]. Therefore, it is important to investigate change of OCV and hysteresis with temperature and C rate to incorporate accurate information to BMS.

Although a standard OCV test is missing in existing standards, researchers previously used different approaches to measure OCV. Step OCV test is appropriate for accurate measurement, however, following issues required to be addressed:

1. Effect of step size on OCV measurement needs to be investigated
2. Use of OCV vs capacity not SoC needs further research attention
3. OCV change with temperature requires to be identified
4. OCV change with discharge rate needs to be investigated
5. OCV hysteresis of different chemistry cells needs to be studied

4.4 Summary

The existing standard capacity tests with constant current discharge at C rates and temperatures do not reflect the dynamic discharge profile of an automotive battery pack and current/power de-rating. Hence, constant current discharge capacity requires to be validated with dynamic discharge profile e.g. drive cycle for automotive application. Also, commonly a BMS calculates a battery's SoC through coulomb counting and SoC is used to estimate RDR. Although different approaches have been proposed in literature to translate SoC to RDR, discrepancy of RDR estimation in existing EVs is still require significant improvement. This is possibly due to that fact that SoE, not SoC, has a direct relationship with RDR. This thesis will focus on use of SoE in RDR estimation.

Since EIS is considered as an online measurement technique, ECM parameterisation method and periodic characterisation tool as part of long duration ageing tests, a reliable and reproducible measurement is essential. Inadequate relaxation period can potentially significantly affect the reproducibility of the test result. This thesis will provide insight to the effect of short and long term relaxation period on EIS results at different temperature and SoC.

To develop an ideal OCV test protocol, the influence of step size on OCV measurements will be researched as part of this thesis. The proposed testing protocol then will be used to identify OCV and thus research OCV hysteresis of different chemistry lithium-ion cells, including different temperatures and charge-discharge rates.

5. Methodology of research

The procedure or system under investigation has a direct influence on selecting research methodology. To understand the problem of Li-ion battery testing for EV applications, a logical approach has been adopted for this research project. The research begins with reviewing the operation and construction of Li-ion batteries, followed by inquisitive investigation of current characterisation test approaches of Li-ion battery for EV application. A review of today's knowledge of characterisation of Li-ion batteries has been completed in previous chapters. It reveals that existing characterisation tests present in standards and used by researchers have significant difference between them. It also identified that current characterisation test techniques are not suitable to meet EV requirements, lack consistency and reproducibility which has received relatively little research attention.

Existing knowledge of characterisation tests have been likened with automotive requirement in order to create knowledge of more practical design methods for characterisation tests. The research begins with identifying limitations of characterisation tests considered as part of this study. Then research proceeds to investigate different methodology to overcome the limitations and identifying better approach. In the final stage of the research, it will be the implementation of the practical design of the characterisation tests and validation.

To contribute insight to the problem of characterisation tests it is very important to have sound knowledge of the fundamental science involved in the individual tests. The research methodology adopted for this research project has been illustrated in Figure 36. The literature review leads to different requirement of different

characterisation tests. In general, research problems with individual characterisation tests have been identified from the literature review. The research problems are analysed next to generate problem classification. This helps to recognize the fundamental knowledge of the research problem and identify gaps in existing knowledge. Once relevant gaps are identified, systematic actions are taken to fill the gaps in knowledge. When gaps cannot be filled with purely theoretical approaches, practical experimentations are considered. Finally, validation and reference implementation provide evidence for the applicability of the new knowledge to the automotive application. This approach provides a comprehensive perspective to the research problem and contributions to the research community thus have been chosen for this research.

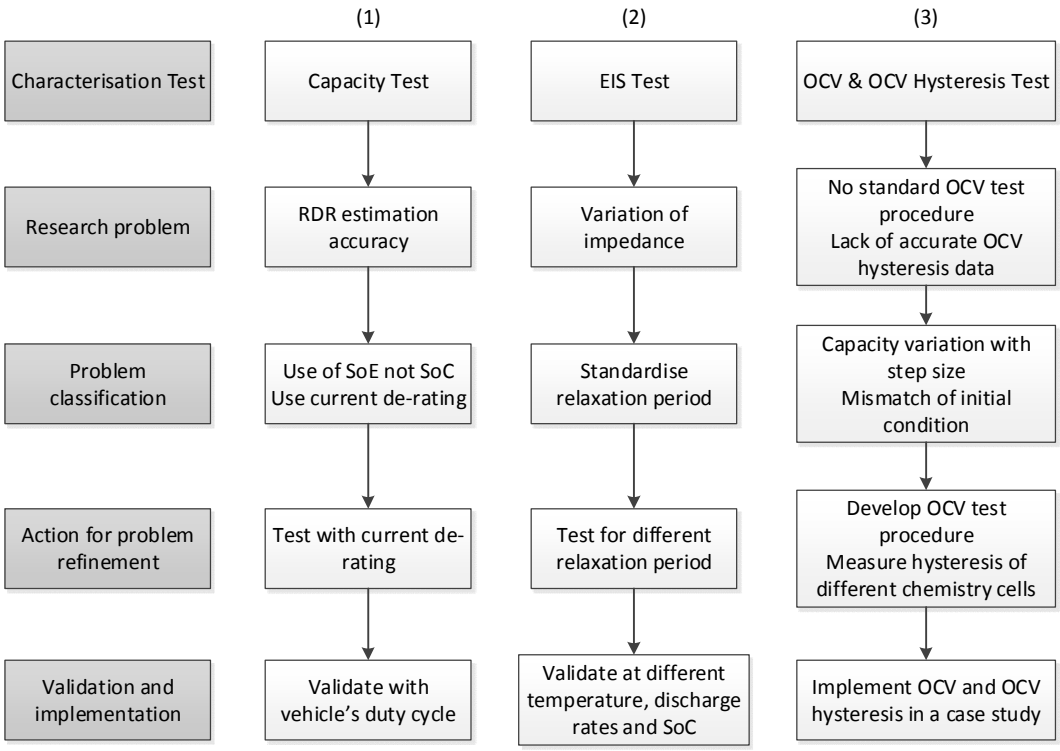

Figure 36: Research methodology

1) RDR estimation by BMS largely depends on capacity test data. Capacity test requires reporting capacity in Watt-hours instead of existing use of Amp-hours, while introducing current de-rating toward end of discharge. Therefore, a modified test procedure needs to be developed. Finally, the constant current capacity requires being validated using a realistic drive cycle of an EV.

2) From review of operation of Li-on cell it has been identified that cell impedance might vary with relaxation period. It neither received attention of the research community nor represented in standards. To investigate the required minimum relaxation period a test plan needs to be developed which will perform EIS test after different relaxation periods. From this test the minimum relaxation period to ensure constant results will be identified. This relaxation period will also be validated for different discharge rates, temperatures and SoCs.

3) The importance of OCV and OCV hysteresis in defining the performance of ECM has been explained. It is identified that there is no standard way of measuring OCV accurately and there is a little information of OCV hysteresis of different chemistry li-ion cells except LFP. The research will generate knowledge how an OCV test methodology will keep account of capacity variation and possibility of initial mismatch of charge and discharge OCV, thus allowing an accurate estimation of OCV hysteresis. To achieve this, initially variation of capacity with step sizes used for OCV tests will be identified, then, to account for any possible initial mismatch a reference procedure will be developed. Then OCV and OCV hysteresis of not only LFP cell but also cells of different chemistry will be measured. Finally, possible improvement of performance of ECM will be discussed using a case study.

6. Driving range estimation through capacity testing

6.1 Chapter Introduction

The primary objectives of this chapter are to study how successfully the existing capacity test interprets cell capacity for automotive applications, considering the current de-rating technique typically employed by a BMS. Suggestions to incorporate this knowledge into future developments of capacity tests for automotive applications are discussed. Since capacity is directly seen by the user, manifested as vehicle range, any inconsistencies in measuring a battery's capacity are directly translated to the end user. Therefore this thesis also focuses to understand how better remaining driving range (RDR) estimation can be achieved through improved capacity testing methods.

The existing capacity test applies constant current charge/discharge cycles at C rates and temperatures. A constant current discharge does not reflect the dynamic discharge profile of an automotive battery pack. Therefore, any capacity data extracted using constant current discharge requires to be validated with dynamic discharge profile e.g. drive cycle for automotive application, which is not part of existing standard testing.

Commonly a BMS calculates a battery's SoC through coulomb counting, considering other parameters like OCV, SoH, temperature etc. [139, 140]. The constant current discharge capacity is used to define 0 % and 100 % SoC. Thus, SoC indicates a battery's remaining capacity in amp-hours; however, this is not a direct analogy of RDR. The speed of the vehicle is proportional to the power transferred to

the wheel, and distance travelled is equivalent to the energy in Watt-hours, not capacity in Amp-hours. Some authors have proposed methodologies using the remaining capacity (i.e. SoC) to estimate the RDR by BMS [116, 141, 142]. The proposed approaches adopted methodologies to translate capacity in terms of Ah into remaining range (an analogy to a fuel gauge). State of Energy (SoE) however indicates remaining energy in Watt-hours, which therefore could be used as a direct analogy of RDR through Equations (14) and (15) (in Section 3.1). Using the experimental evidence later in this chapter it will be demonstrated that remaining energy in Watt hours (SoE), is more appropriate than SoC for estimating the RDR of an electric vehicle.

To maximise battery capacity, automotive battery packs are de-rated to a low discharge current toward end of discharge (low SoC) [143]. However, when only battery capacity (including current de-rating) in Amp-hour, i.e. SoC, is taken into consideration to calculate the total driving range, the difference in waste energy in the form of Joule heating is not considered. Therefore there is a possible discrepancy between actual driving range achieved, and that estimated through SoC. Conversely, SoE takes account of the waste energy, making a better estimation of remaining driving range.

Previous studies of estimated remaining driving range have considered the effects of parasitic losses due to air-conditioning usage, lamp and radio status [144]; vehicle current location [128]; road network topology [128]; expected road gradients [145]; expected travelling speeds [146]; expected acceleration and deceleration [147]; expected power demand [148]; expected weather conditions such as temperature and

wind speed [146]; and driving style (i.e., aggressive or mild) [146]. In more recent work *Liu et al.* [149] proposed an online neural networks based approach to estimate SoE that accounts for the energy loss in the battery due to irreversible joule heating caused by charge transfer and the falling open circuit voltage (OCV) due to phase shifts. However, a clear explanation of the improvement of the estimation of remaining driving range by adoption of SoE instead of SoC was not provided. Moreover, they too did not consider current de-rating and short-term cycling history (previous short duration current/power demand of the vehicle) as a possible influence on total available energy of the cell even after de-rating the battery power.

The dependency of the energy immediately available to the driver on cycling history has largely been ignored. Indeed, the form of Equation (22) through SoE or $F(\gamma)$, doesn't readily facilitate the inclusion of short-term cycling history. Later in this work it will be shown that accessibility of the stored chemical energy in Li-ion batteries depends on short-term cycling history, and therefore through de-rating, the total energy cannot reach the theoretical maximum. This relationship will be validated for real world scenarios using drive cycles. This knowledge then needs to be incorporated with the existing capacity test procedure to develop an appropriate test procedure for automotive applications.

In this chapter, after outlining the experimental method adopted for this study in Section 6.2; Section 6.3 presents results showing the existing standard capacity test results to support the recommendation that SoE is more appropriate than SoC in the reliable estimation of remaining driving range of EVs. A method for estimating remaining energy through the capacity test technique considering short-term cycling

history (due to current de-rating) is presented in the same section along with model validation. Finally, in Section 6.3 we propose how the existing capacity test technique could be developed for automotive applications using the knowledge generated as part of this research. To conclude, Section 6.4 summarises the key findings and contribution to knowledge.

6.2 Experimental method

Five commercially available Li-ion pouch cells with a $LiMn_2O_4$ (LMO) cathode and LiC_6 (graphite) anode were used for this study. The rated capacity, maximum discharge current, maximum charge voltage and minimum discharge voltage of the cells were 20 Ah, 200 A (10C), 4.2 V and 2.7 V, respectively. Five cells were chosen to ensure statistical significance and to minimise effects of cell-to-cell variations. Upon delivery from a commercial supplier, the cells were stored at 10 ℃ and 50 $\% SoC$, thereby minimising inevitable calendar ageing. Since the cells were not cycled, the cells employed in this work can be considered new. Moreover, in order to isolate the effect of temperature, all the tests were carried out at 25 °C within an environmental chamber (Weiss Gallenkamp Votsch, model: VC^3 4060).

In preparation for testing, the cells were fully charged. For this purpose, after taking the cells out of storage, the cells were discharged at a 1C rate to the manufacturer's recommended cut-off voltage (in this case 3V) at 25°C using a commercial Li-ion cell cycler (Bitrode battery cycler, model: MCV 16-100-5). The cells were then allowed to rest for 3 hours before being fully recharged via the constant current – constant voltage (CC-CV) protocol using a 1C current for the CC part until the voltage cut-off is reached and a C/20 cut-off rate for the CV part. At the end of

charging the cells were allowed to rest for 3 hours prior to cycling. The 3 hours rest period was used to allow the cell to reach electrochemical equilibrium [150].

6.2.1 Standard constant current capacity test

To examine the cell capacity at constant currents of different C rates, cells were discharged at 25°C using C/3, 1C, 3C and 5C discharge current until the manufacturer's recommended cut-off voltage was reached. This is the standard procedure commonly used by academic and industrial researchers, to determine a cell's capacity at different discharge rates.

6.2.2 Capacity test with drive cycle

Following the constant current discharge, cell capacity needs to be examined in the context of real driving scenarios. To do this, a dynamic real world drive cycle is required. This has a range of discharge rates and also includes some regenerative braking charging events. Two duty cycles, generated using a 1-d sizing tool for rapid optimization of pack configuration, explained in Ref. [151], were employed for validation. For a given battery pack size, cell choice, and drive cycle speed profile, the model outputs a time based power demand. Pack design parameters were chosen to coincide with a typical family sized vehicle such as the Nissan Leaf or BMW i3. Accordingly, the total pack energy was set to a minimum of 22 kWh with a maximum power of 125 kW and a nominal voltage of 350 V. The parameters adopted for the cell correspond to that employed in this study, namely a 20 Ah cell with a 200 Amp maximum current and nominal voltage of 3.7 V. The drive cycles used were the Artemis urban and Artemis motorway drive cycles. The urban drive

cycle has a 36 mph maximum speed and frequent rest events – and had a maximum power demand per cell of ~125 Watts and an average power demand (including regenerative charging) of ~31 Watts. In contrast, the motorway drive cycle with around 82 mph maximum speed had approximately 250 Watts maximum power demand and ~127 Watts average power demand. These two duty cycles are shown in Figure 37.

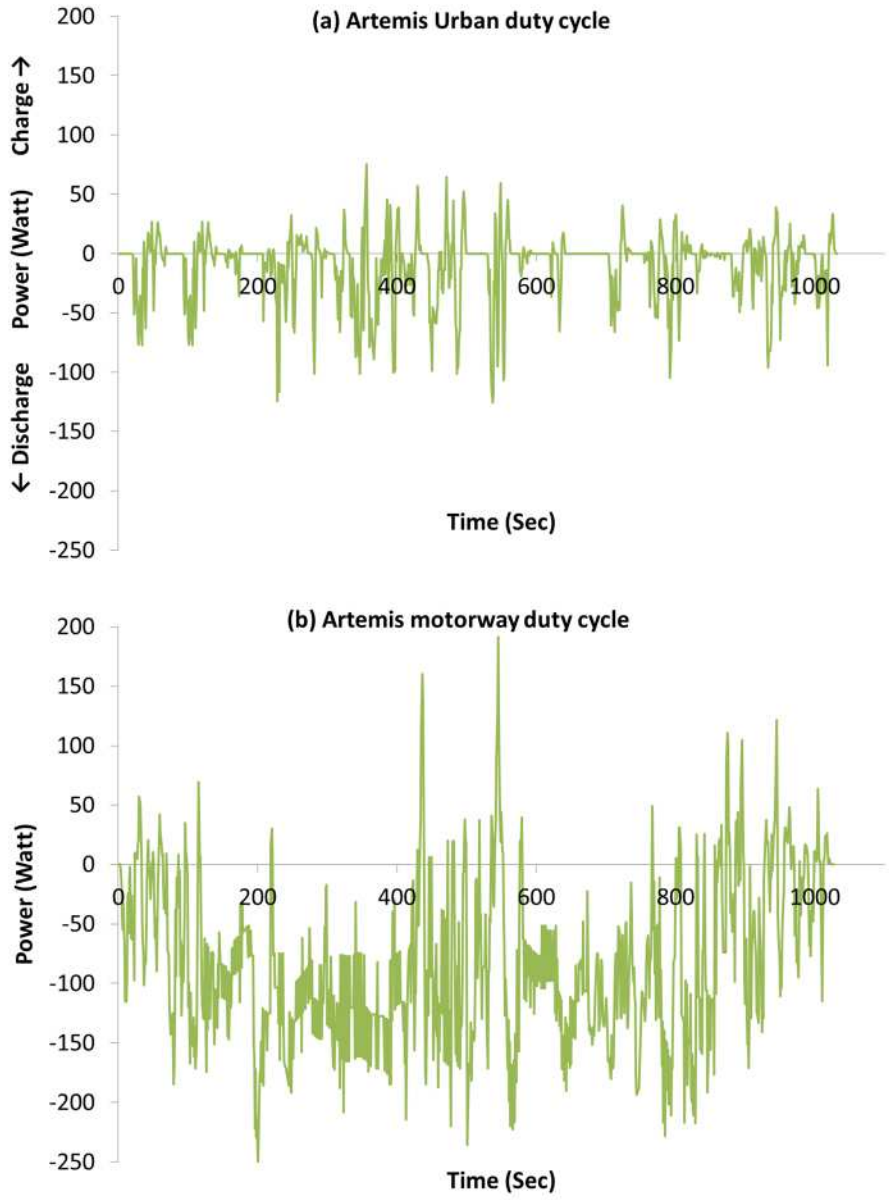

Figure 37: Two duty cycles (a) Artemis urban and (b) Artemis motorway generated for this particular cell using 1-d sizing tool.

The duty cycles were repeatedly used to discharge the cells until the minimum cut-off voltage of the cell was reached. This experiment identifies the cell capacity for a specific driving scenario.

6.2.3 Introduction of current de-rating into capacity test

The next stage of the experiment is to examine the effect of current de-rating of the cell toward the end of the discharge on cell capacity in Amp-hours and energy at Watt-hours. The cells were first continuously discharged from 100 % SoC to 20 % SoC at different rates, that is, from a fully charged state approximately 16Ah of capacity was extracted at the rates: C/3, 1C, 3C and 5C. The cells were then discharged at C/3 (without rest) until the manufacturer's recommended cut-off voltage was reached. The C/3 current rate was selected to represent a de-rated current for low SoC operation. This will determine if, under current de-rating conditions, the total capacity/energy available in a cell has a dependency on the method of initial 80% discharge.

6.2.4 Validation test with drive cycle

Any dependency on the current de-rating will need to be validated with real world driving scenario. In the first validation test, the cells were fully discharged using the Artemis urban drive cycle until the manufacturer's recommended cut-off voltage was reached. In the second test the cells were first discharged by 80 % SoC using the Artemis motorway drive cycle then instantly switched to the urban drive cycle until the voltage cut off was reached.

6.3 Results and discussion

6.3.1 Standard constant current capacity

The discharge capacity of the cell in Ah measured by traditional coulomb counting at four different discharge rates is shown in Figure 38. At the beginning of discharge and subsequently cell voltage drops with the increase of the current rate. This is due to higher voltage drop across total resistance of the cell (R in equivalent circuit shown in Figure 21) with increased discharge rate. Compared to cell capacity at the C/3 rate, capacity drops by 29 % at 5C discharge rate (Figure 39). This is due to the cell reaching the cut-off voltage (3V) earlier with the increase of discharge rate. This capacity drop with the increase of discharge rate is well known and is in accordance to the results reported in the literature [30, 95, 98].

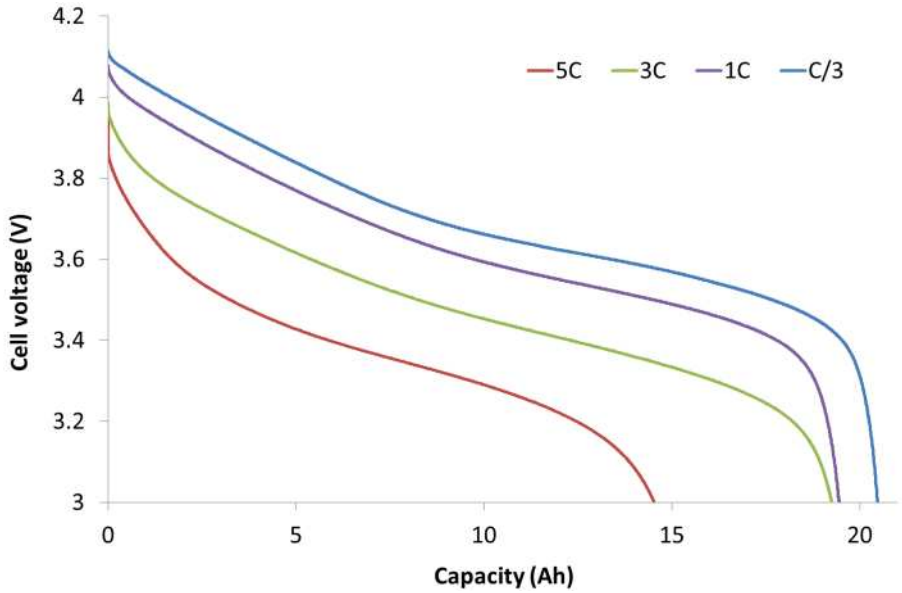

Figure 38: Discharge capacity of the cell at four different discharge rates.

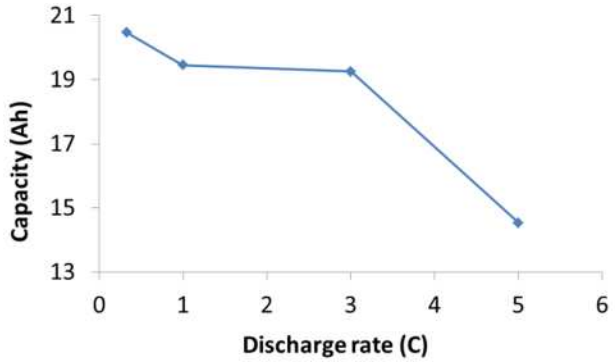

Figure 39: Capacity variation with constant current discharge rate.

6.3.2 Extracted capacity with drive cycle

Following the procedure explained in Section 6.2.2, the constant currents used to discharge the cell (as in Figure 38) have been replaced with two duty cycles derived from the Artemis urban and Artemis motorway drive cycle. The cell capacity for these two driving scenarios is presented in Figure 40. In the Artemis urban duty cycle, which has a similar average current to C/3, shows a similar discharge capacity (20.76 Ah) as C/3 constant current capacity (20.73 Ah). Artemis motorway is a more aggressive duty cycle having around 1C average current and 3.4C maximum current, and this shows 2 % lower capacity (19.01 Ah) to the 1C constant current (19.45 Ah). To design a more aggressive duty cycle with high average current (e.g. 3C, 5C) the maximum current of the duty cycle exceed the maximum current of the battery (especially at lower SoC). The validation of constant current discharge capacity with duty cycles was known to the research community; however, it has not been used commonly. These results suggest opposite trend of EV and conventional IC engine vehicle. In general, IC engines are more efficient in motorway driving compared to city driving. On the other hand, EV will provide longer range in city driving compared to high speed motorway driving.

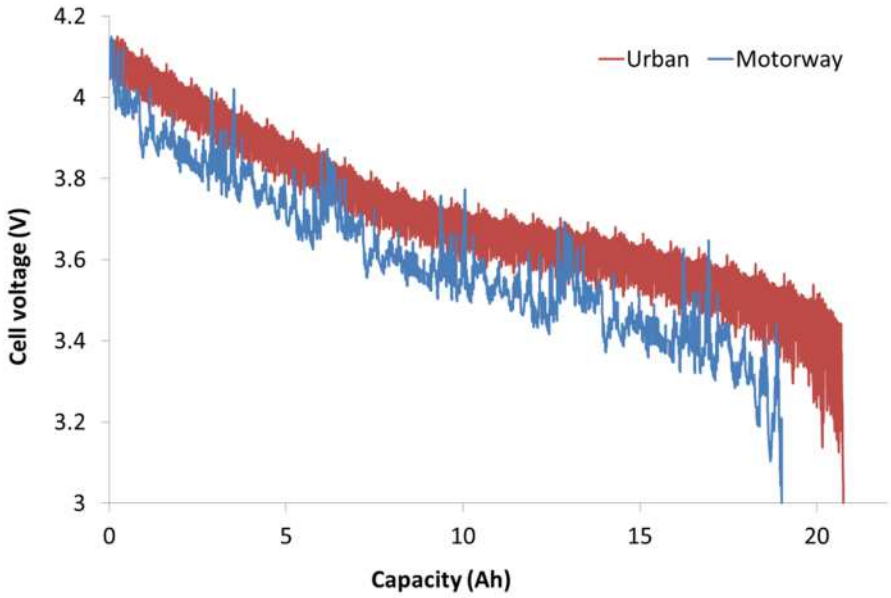

Figure 40: Discharge capacity of the cell at two different driving scenarios, Artemis urban and Artemis motorway.

6.3.3 Capacity and energy after de-rating

As discussed earlier in this chapter and in Section 4.1, while the battery is being discharged at a high rate (driving at high speed) the BMS can de-rate the battery's current capability to a lower C rate toward the end of discharge to maximise battery capacity. To represent de-rate of current capability of the battery in capacity testing, constant current capacity tests were performed in two phases. Discharge capacity in Ah of the cell for a two-phased discharge profile – a higher rate ($\geq C/3$) from 100 – 20 % SoC and a lower (C/3) rate from 20 – 0 % SoC – is shown in Figure 41. Different discharge rate was used to discharge from 100 – 20 % SoC to investigate cycling history (short-term cycling history) prior to re-rating. At 5C discharge, the cell reached the minimum discharge voltage at 28 % SoC (14.53 Ah), at which point discharge with C/3 was started. For other rates the cells were able to be discharged to 20 % SoC (16 Ah). Regardless of the rate employed in going from 100 – 80 % SoC,

it was found that the total discharge capacity, with the exception of maximum 0.6 % differences, was the same. The test with 5C current shows maximum capacity, 0.6 % higher than C/3 capacity which was the lowest among the tests. Although it a small variation, close to experimental error, however the trend is in opposition to the common knowledge i.e. higher the C rate lower the capacity. The possible reason can be the temperature rise associated with the higher C rate. Temperature of the cell at the end of discharge with high C rate (20 % SoC) is presented in Figure 42. At the end of 3C and 5C discharge, cell surface temperature rose to 36 °C and 44 °C respectively. Therefore, the C/3 discharge from 20 – 0 % SoC was started at a higher temperature for the 3C and 5C tests. As explained in Section 3.1, a higher amount of capacity could be discharged at higher temperatures, which has been seen in Figure 41.

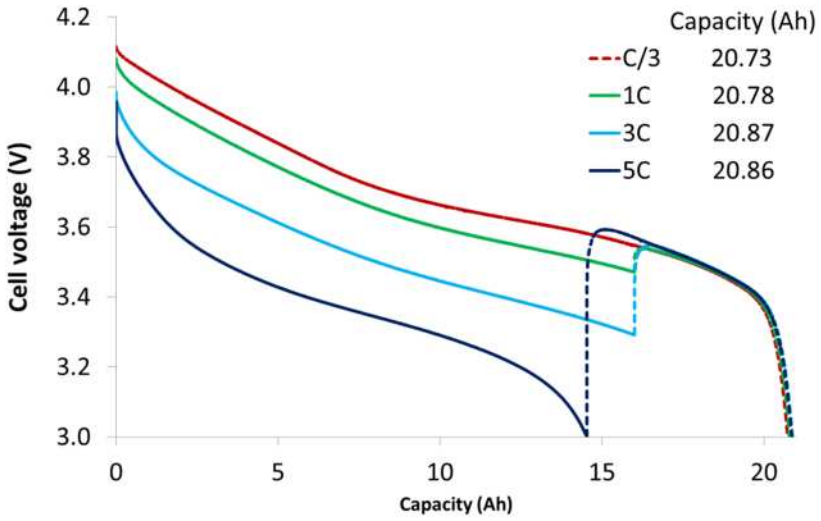

Figure 41: Discharge capacity (Ah) yield for a two-phased discharge profile. The solid lines indicate discharge rates employed (as in the caption) and dotted part indicates the C/3 rate.

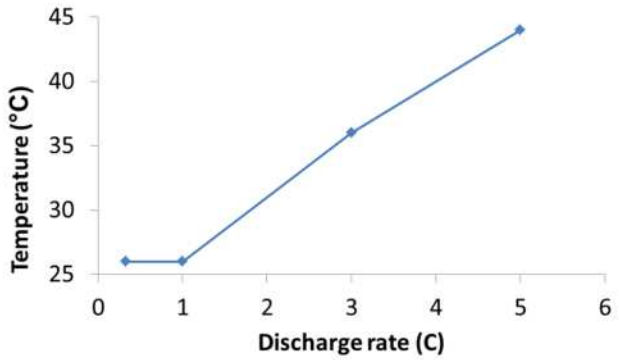

Figure 42: Cell temperature rise associated with discharge rate.

For the same tests, when the total energy discharged was obtained, Figure 43, the 5C rate test had a lower discharge capacity by up to 7% compared to C/3 discharge energy. Therefore, although 29 % capacity reduction with 5C constant current capacity test (Section 6.3.1) can be recovered through current de-rating, however, 7 % of total energy is not recoverable, leading to a discrepancy between total capacity in Amp-hours and Watt-hours. It is in contrast to the phenomenon that the cell temperature was higher for high discharge rates; leading to more capacity (and energy) able to be extracted. Therefore, if the heat generated at a higher discharge rate was extracted from the cell (by a suitable cooling system) and the cell temperature remains similar (to 25 °C), the 7 % drop in total energy could be higher.

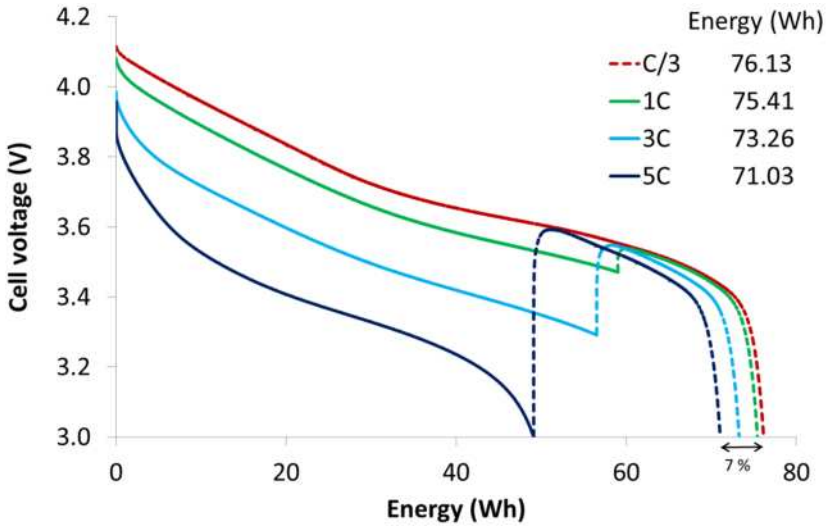

Figure 43: Discharge energy (Wh) yield corresponding to the two-phased discharge profile described in Figure 41.

This discrepancy between capacity/energy in terms of Amp-hours and Watt-hours means that using SoC as an analogue to the fuel gauge, as some OEMs have done [152-154], can lead to inaccurate indications of range, since RDR is a function of SoE, not simply SoC. It is suggested, therefore, that a better analogue to the fuel gauge is perhaps the measure of energy, SoE. Thus, a fundamental change in RDR estimation by BMS is required. The variation of total discharge capacity in Watt-hours, while discharge capacity in Amp-hours remaining the same, has not been reported in earlier literature and is presented in this thesis for the first time.

The difference between the behaviour seen in Figure 41 and Figure 43 can be explained from the origin of the total energy of the cell. The energy of the cell (E_{cell}) is expected to follow the relation:

$$E_{cell} = E_{thermodynamic} - E_{loss}$$

$$E_{cell} = \int_0^{Ah_{max}} V_{OC} dQ - \int_0^{t_{end}} \hat{\imath}_{cell} \left(V_{OC} - V_{cell} - T_{ref} \frac{dV_{OC}}{dT} \right) dt \quad (19)$$

where, V_{OC} is the cell's open circuit voltage, Q is the capacity measured in Ampere hours; $\hat{\imath}_{cell}$ is the average discharge current, V_{cell} is the cell's terminal voltage, T is temperature and T_{ref} is a reference temperature [155]. The first term on the right hand side of Equation (19) is the cell's thermodynamic energy ($E_{thermodynamic}$).The second term on the right hand side of Equation (19) is a loss term (E_{loss}) where $i_{cell}(V_{OC} - V_{cell})$ represents irreversible Joule heating caused by charge transport and the differential term represents the reversible rate of heat generation due to entropy change within the cell [155]. Given that the loss term will be dominated by charge transport contributions, it can be approximated as

$$E_{loss} \cong \int_0^{Ah_{max}} \hat{\imath}_{cell} R_{total} dQ \tag{20}$$

where, R_{total} is the total internal resistance of the cell and includes contributions from both the Ohmic and polarisation resistances. Therefore, Equation (19) can be re-written as

$$E_{cell} \cong \int_0^{Ah_{max}} (V_{OC} - \hat{\imath}_{cell} R_{total}) dQ \tag{21}$$

The cell's thermodynamic energy ($E_{thermodynamic}$) is the total area under the OCV vs capacity plot (Figure 44). Compared to discharge capacity plots shown in Figure 38 this plot can be considered as theoretical zero C discharge. The OCV test procedure is similar to the procedure outlined in Ref [156] and also has been explained in Chapter 8 of this thesis. For this particular $LiMn_2O_4$ cell, the total area in Figure 44 is 76.301 Wh. This thermodynamic energy is a little higher than the energy for C/3 rate discharge (76.13 Wh, in Figure 43) as there is no Joule heating.

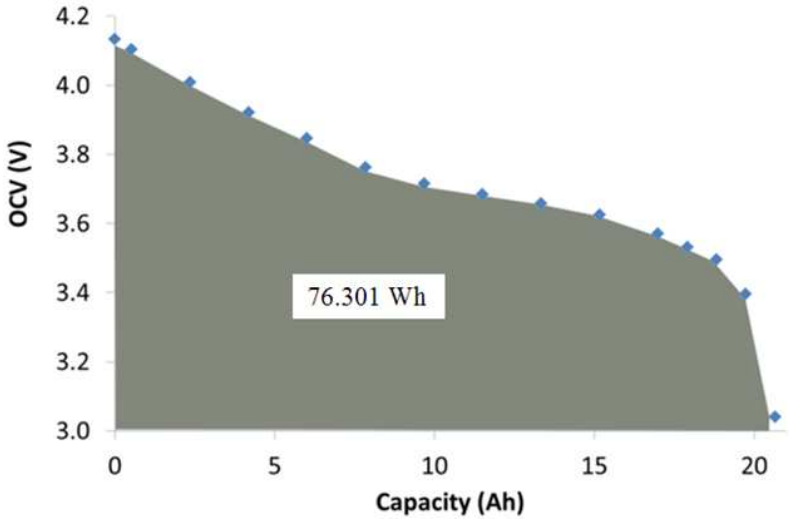

Figure 44: OCV vs capacity of the cell. The shaded area represent maximum energy can be stored within the cell.

As $\hat{\imath}_{cell}$ is average current (thus can be considered as constant), $\hat{\imath}_{cell} \int_0^{Ah_{max}} R_{total} dQ$ represents the loss term E_{loss} (Equation (20). Therefore, by calculating $\int_0^{Ah_{max}} R_{total} dQ$, the loss term for a given $\hat{\imath}_{cell}$ can be calculated. Thus, the total resistance R_{total}, needs to be measured over 0 – 100 % SoC (capacity range) . The total resistance was calculated using the voltage response to a series of 10 second discharge pulses across a State of Charge range (see Figure 45 (a)). The 10 second pulse duration was used following the standard pulse power test protocol as outlined in Ref [25, 26, 102]. The gradient of the curves indicates the total resistance of the cell at the corresponding SoC.

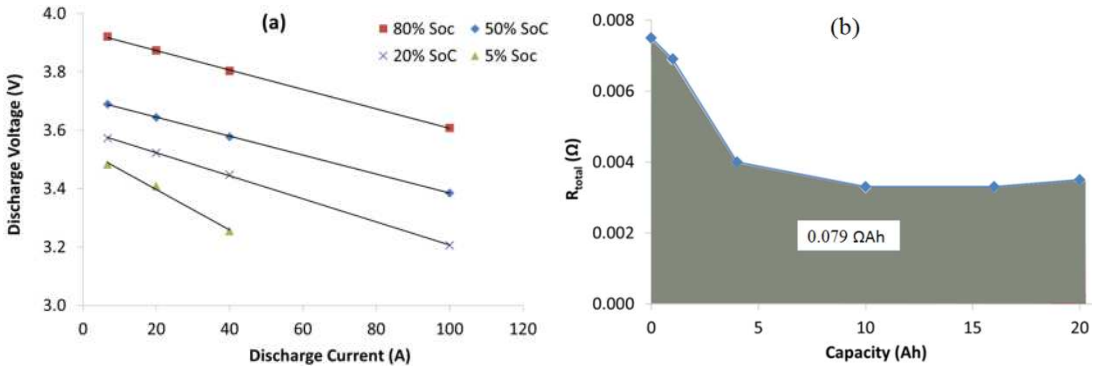

Figure 45: Cell voltage versus 10 second pulse currents is shown in (a); the gradients of the curves indicate the total resistance. Total resistance is then plotted as a function of discharge capacity in (b).

In Figure 45 (b) the 0 Ah and 20.73 Ah points are extrapolated estimates as completing charge-discharge pulses at these two extreme ends were not possible. In the experimental set-up considered in this work, the loss term is expected to scale linearly with cell current $\hat{\imath}_{cell}$ because both the integration limits and the profile of $R_{total}(Q)$ are fixed (see Figure 45 (b)); that is, regardless of rate, the area under the curve in Figure 45 (b) remains the same and therefore $E_{loss} \cong 0.079\hat{\imath}_{cell}$. Equation (21) can therefore be parameterised for the cell and written as

$$E_{cell} \cong 76.301 - 0.079\hat{\imath}_{cell} \tag{22}$$

which agreed with what was found experimentally as shown in Figure 46. In Figure 46 the total energy discharged from the cell is shown as a function of average discharge current. Average discharge current is the average of the high discharge rate used to discharge the cell from 100 - 20 % SoC and the C/3 discharge rate used to discharge from 20 - 0 % SoC. It was found that E_{cell} does indeed scale linearly with average discharge current. Moreover, while the first term in Equation (22) ($E_{thermodynamic}$) matches the experimental results to within ~0.11 %, the second term in Equation (22) fits the experimental results to within ~3.8 %. Although the

gradient approximation varies by 3.8 % it is adequate to estimate the total energy of the cell at high discharge rates with only a maximum 0.3 % variation (Figure 46), which falls within the cell to cell variation and error limit of the cell cycler used for this test.

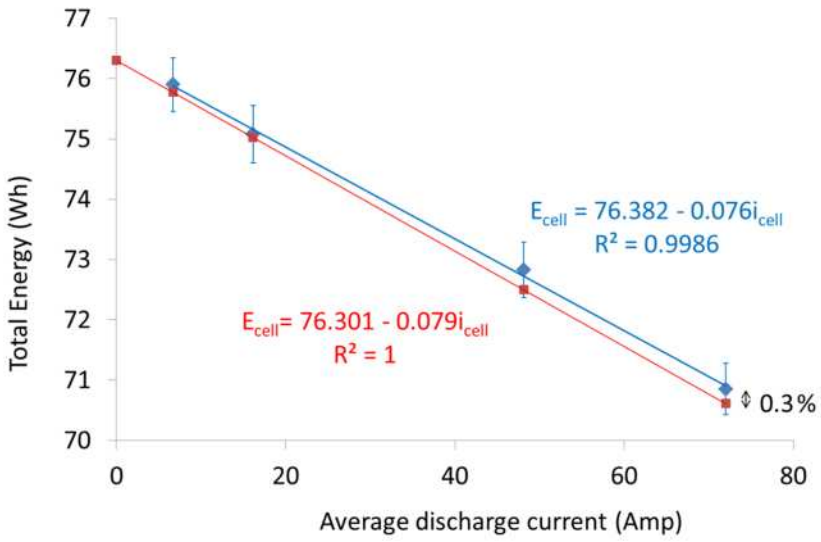

Figure 46: Total discharge energy vs average test current; red is the model approximation (Equation (22)) and blue is the experimental results. Error bars show cell to cell variations and experimental error.

From the results presented in this section, it can be concluded that SoE is a more appropriate measure of potential vehicle range than SoC for automotive applications. The effect of the average discharge current rate on total energy has been demonstrated for a continuous discharge, and this has been compared to theoretical predictions. The relationship and the validation have been shown for the first time here which has the potential to be implemented as part of a BMS. However, the average of constant discharge currents were used to show that the energy capable of

being extracted is dependent on short-term cycling history. It remains then to show that an average current from a duty cycle has similar behaviour.

6.3.4 Validation

To show the validation of the relationship with a drive cycle, real-world driving scenarios where currents vary according to power demand are employed. In agreement with the arguments presented in Section 6.2, in the first case of the Artemis Urban drive cycle which had an average current close to C/3 (8.36 Amperes), the resulting energy discharged falls on the linear fit (indicated by the first green dot in Figure 47). In the second case where the Artemis Motorway drive cycle was used for the first 80% of DoD followed by the Artemis Urban drive cycle for the last 20%, the average current was 19.06 Amperes and the resulting energy discharged is very close to the linear fit. In both of the cases green dots are within the experimental error limits (error bars). In contrast, capacity in terms of Ah (indicated by black markers in Figure 47) shows a minimal variation tending towards a rise in capacity as compared to total energy discharged, which had a negative trend; hence, employing capacity in the form of Amp-hours to calculate RDR leads to a worse estimation of remaining energy and hence vehicle range.

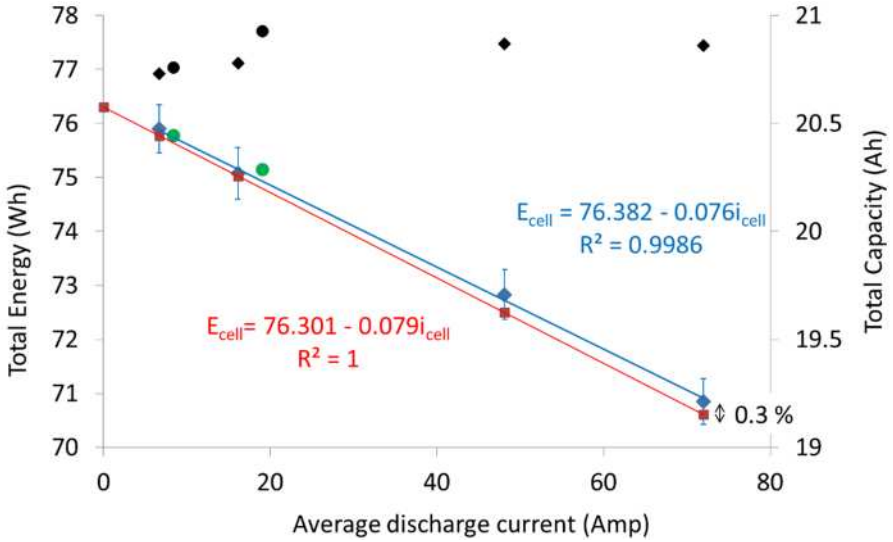

Figure 47: Validation results (green dots) for the two duty cycles. Black markers show corresponding capacity (Ah), round dots for duty cycles and diamond for continuous discharge (blue), red is for the model estimation.

This demonstrates that the method of total energy estimation described in this chapter is valid for dynamic real-world duty cycles as well as for continuous discharge cycles. The average current described above accounts for the average total current, that is, charging and discharging, compared to simply a continuous discharge current described earlier. The inclusion of dynamic charging and discharging currents could explain why the two green dots representing performance of the prediction for dynamic duty cycles are slightly different from the theoretical prediction, although within error limits and still having good agreement.

6.3.5 Future potential application

Tracking changes in energy yield as a function of average current could be used as a diagnostic and prognostic tool for battery SoH, see Figure 48. That is, as the battery degrades one expects capacity fade (capacity loss leading to a lowering of driving

range) and power fade (increase in impedance leading to a lower vehicular efficiency). Capacity fade in Watt-hours can be derived by estimating $\int_0^{Ah_{max}} V_{OC}\, dQ$ while power fade is fused into the slope $\int_0^{Ah_{max}} R_{total} dQ$ of the E_{cell} vs $\hat{\imath}_{cell}$ curve. As ageing proceeds the former is expected to fall while the latter is expected to rise, changing the gradients of the E_{cell} vs $\hat{\imath}_{cell}$ plot (Figure 46). As the capacity in Amp-hours vs $\hat{\imath}_{cell}$ plot does not provide similar relationship (Figure 47), the possible estimation of SoH can only be done using E_{cell}. However, this concept needs further experimental work which will be covered in future research.

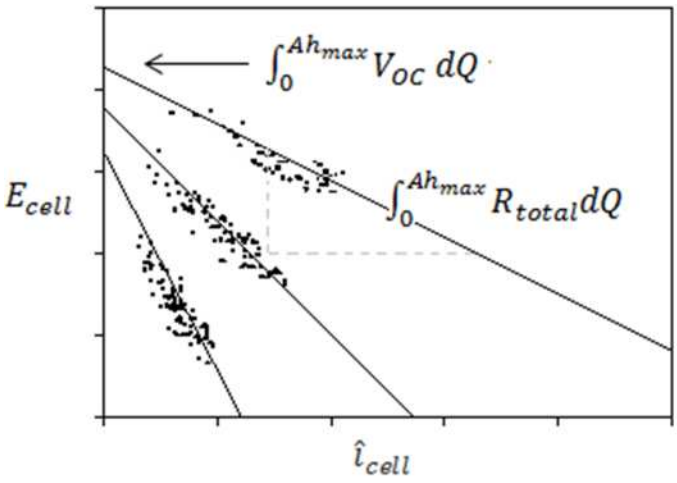

Figure 48: Illustrating how capacity fade and power fade of the traction battery can lead to changes in the $\boldsymbol{E_{cell}}$ vs $\boldsymbol{\hat{\imath}_{cell}}$ curve. The data points here are purely illustrative.

This has important consequences for a BMS and indicates that by controlling, or de-rating, the discharge current, the BMS is able to more accurately predict the remaining available range via energy/SoE. The linear relationship presented in Figure 46 and Figure 47 needs to be developed using capacity test results. Therefore, existing capacity tests need to be updated to reflect current de-rating and real world driving behaviour for automotive application.

6.4 Chapter conclusions

The capacity of the commercially available Li-ion cells has been investigated using the standard capacity test procedure with different discharge rates. The change of discharge capacity value with discharge rate agreed with previously published results.

The standard capacity test results have been validated for two different driving conditions, Artemis urban and Artemis motorway. In both cases, capacity was found to be in close agreement with standard constant current capacity tests, considering average current of the duty cycles are used.

The driving range of an EV is directly related to the energy in Watt-hours. In contrast, the existing capacity test measures capacity in Amp-hours. Amp-hour is then converted into driving range of an EV using various methodologies proposed in the literature. In this chapter it has been shown that in contrast to the existing measure of Amp-hour as SoC, SoE in the form of Watt-hours is more appropriate as an analogue to the “fuel gauge” for EV range prediction. This new knowledge suggests that a fundamental change (SoE instead of SoC) in BMS operation is required to more accurately predict EV range.

It is well known that discharge capacity decreases with increased discharge rates. Therefore, to maximise battery capacity a battery pack’s discharge current is usually de-rated by the BMS as the SoC approaches zero, which is commonly used by OEMs. In this chapter it has been shown that although through current de-rating the otherwise inaccessible capacity can immediately be recovered, the short-term cycling

history of a cell will dictate the driving range (total energy). Therefore, even though the capacity was recovered by de-rating a 5C cycle to C/3 at 20% SoC, in comparison to complete C/3 cycle, 7 % of energy in the 5C cycle was unrecoverable.

In Figure 46 and Figure 47 it was shown that the total useable electrical energy is linearly related with the average current of the short-term cycling history. This concept was validated with experimental results using constant current discharge. The applicability of this relationship in real world driving has been shown for two different duty cycles. It is evident that during a dynamic driving cycle, the energy available (SoE) and therefore the remaining driving range is dependent on short-term cycling history, which is not obvious with existing method (SoC).

Through further research, the relationship between short-term cycling history (average current) and total energy could be employed to estimate degradation (ageing) of power capability and a battery's capacity in the form of Watt-hours (thus the range) with vehicle usage. The new knowledge presented in this chapter will lead to design of better performing capacity test for automotive application, improving overall performance of EVs.

7. Consideration of the relaxation phenomenon for the EIS test technique

7.1 Chapter Introduction

This chapter aims to understand the effect of cell relaxation (the time taken for a cell to stabilize after a charge or discharge) on the EIS response, and incorporate this understanding into testing protocols which ensure repeatability and reproducibility of the EIS measurements.

For on-board EIS measurement systems (incorporated as part of the BMS), measurement time is a key requirement. However, fast measurement time implies that the cells will be measured very shortly after cycling; relaxation phenomenon in this time period is very important. In this case, a high number of data points on the Nyquist plot cannot be achieved. On the other hand, the effect of relaxation over longer durations is important for a laboratory environment, where a measurement is usually performed after several minutes to several hours after charge/discharge. In this case a higher number of data points are essential to perform meaningful electrochemical analysis. Therefore, two different experimental procedures are essential to investigate short-term and long-term effects of relaxation on EIS results. As explained in Section 4.2, currently there is no standard way to integrate cell relaxation into EIS testing.

The relaxation phenomenon of the cell could be different with varying SoC, temperature, charge-discharge rate, affecting the EIS test results differently. This is due to the change of electrochemical composition within the cell with SoC, change

of number of ions involved with different charge-discharge rate and change of kinetics of ion movement with temperature. Therefore, effect of SoC, temperature and charge-discharge rate on relaxation requires to be investigated.

The remainder of this chapter is organised as follows. In Section 7.2, the experimental methods adopted for this study are presented. Subsequently, in Section 7.3 the analysis of results including discussion around their electrochemical implications with reference to relevant published materials is presented. Finally, Section 7.4 summarises the key findings.

7.2 Experimental method

Five commercially available Li-ion cells were used as part of this study. These cells were selected based on their power and energy rating. Table 5 summarises the chemistry, capacity and format of each cell.

Table 5: Cell details and associated RMS current used during EIS measurements.

Cell number	Chemistry	Capacity (Ah)	Format	Current amplitude for EIS tests (Amp)		Cell type
				Short Duration	Long Duration	
1	NMC	40	Pouch	1.60	1.60	Power cell
2	LFP	20	Pouch	1.20	1.20	Power cell
3	NMC	2.2	Cylindrical	0.20	0.17	Energy cell
4	LTO	13	Pouch	1.00	1.00	Power cell
5	NMC	3.4	Cylindrical	0.23	0.25	Energy cell

In order to isolate the effects of cell relaxation, temperature and SoC were kept constant for each test; tests were carried out at 25 °C and 50 % SoC. The temperature

was selected as 25 °C to represent room temperature and measurements were carried out within a thermally controlled environment set at 25 °C. The 50 % SoC was selected to represent a mid SoC when both of the electrodes contain approximately equal amount of cycle-able lithium. To precisely adjust the cell SoC to 50 %, the cells were discharged at 1C rate to the manufacturer's recommended cut-off voltage at 25 °C using a commercial Li-ion cell cycler. The cells were subsequently allowed to rest for 3 hours before being fully recharged according to the manufacturer's recommended charge protocol, constant current constant voltage (CC-CV). At the end of charging, the cells were allowed to rest for 3 hours prior to being discharged to 50 % SoC at 1C rate.

To study the short-term effect of relaxation, measurements were performed in galvanostatic mode using a Solartron Modulab Xm system. For this study the applied amplitude (RMS value) of the signal was dependent upon the cell type and is summarised in Table 5. To accommodate this current rating a 2 Amp booster card was used with the EIS system (Solartron Modulab EIS system). Impedance measurements between 500 mHz and 10 kHz with 5 frequency points per decade were taken. This frequency range and number of measurement points were selected as a balance of test duration and number of measurement points; measurements at lower frequency take longer duration ($T = {}^{1}/_{f}$). Also, measurement duration is proportional to frequency points per decade. As explained earlier, higher number of measurement points are essential but tests needs to be quicker to study fast change of EIS with relaxation. In this setup a measurement will take around 10 seconds, which is acceptable and provides enough data points for analysis. Recording of the EIS

started as soon as the SoC adjustment was completed (i.e. immediately after the 1C discharge to 50 % SoC), and every 20sec thereafter.

For the long duration relaxation tests, the applied amplitude (RMS value, without any DC bias) of the signal was dependent upon the cell capacity and again is summarised in Table 5. Impedance measurements between 100 mHz and 10 kHz with 10 frequency points per decade were taken. This provides enough data points for the electrochemical analysis with acceptable test duration (1 minute). Recording of the EIS data started 10 min after the completion of SoC adjustment (i.e. after 10 min of the 1C discharge to 50 % SoC), and every 10 min thereafter for 15 hours within the same thermally controlled environment set at 25 °C.

To study effect of SoC on relaxation, a long duration EIS test with a range of SoCs has been performed on cell 1. Although both long duration and short duration EIS tests are important, only long duration tests offer enough data points for electrochemical analysis therefore only long duration test was selected for this instance. In this case, the test was repeated at 100 %, 80 %, 20 % and 0 % SoC. These SoCs were selected as being representative of high and low SoCs, in addition to 50 % SoC. For 100 % SoC, as no discharge is required, the long duration EIS test was started after charge.

To investigate temperature dependency of relaxation, a long duration EIS test has been performed on cell 1 with varying temperature. Cells were discharged to 50 % SoC at -5 °C, 10 °C and 40 °C and long duration EIS test carried out at same temperatures. These temperatures are representative of low and high operating temperatures of an EV.

Subsequently, on the same cell, a long duration EIS test was carried out to investigate effect of discharge rate on relaxation. Cells were discharged to 50 % SoC at 25 °C with different discharge rate, prior to start of EIS tests. Instead of 1C discharge current, 0.1C, 3C and 5C current were used as representative of low and high discharge rate.

7.3 Results and discussion

7.3.1 Short duration relaxation test

The shape of the Nyquist plots at high frequency is similar to that often found in literature (as per Figure 30). However, at low frequency cells 1, 2 and 4 show a spiral shape (Figure 49 (a), (b) and (d)) which was not reported or explained in previous related literature. The spiral shape in the Nyquist plot starts to shrink from the second test done at 1min after SoC adjustment, and finally disappears 10min after SoC adjustment when the EIS plot is similar to the Nyquist plots found in the literature [62, 89, 113]. The change of shape of Nyquist plots from 1min to 10min for cells 1, 2 and 4 happen at a different pace. Cell 3 and 5 (Figure 49 (c) and (e)) shows similar shape only for the very first test which was performed just after discharge was stopped. Afterward the shape is similar to the Nyquist plots found in the literature. To investigate the experimental setup as a probable cause of the shape, the experiment has been repeated with different leads which connect EIS equipment with the test cell, even different set of equipment; however, in all the instances similar results were found. To attempt to explain these findings a deeper understanding of the cell construction and operation is required.

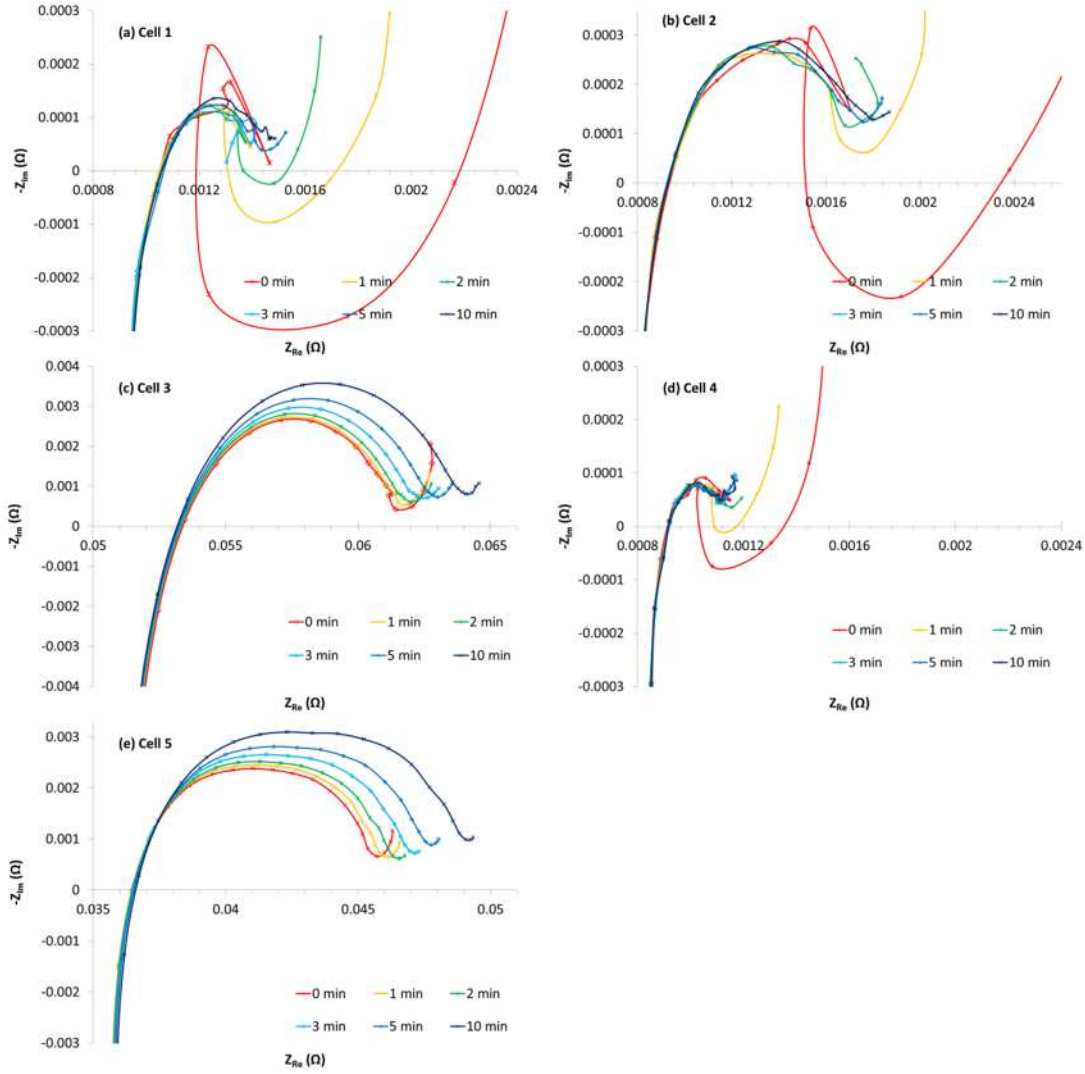

Figure 49: Nyquist plots of the cell from 0 – 10 min. Note that two different scales have been used for figures (a), (b) and (d), and (c) and (e).

Depending on the application of the Li-ion battery, the electrode preparation may be modified to ensure the cell meets the desired application requirements. Two of these characteristics are porosity and tortuosity of the electrodes. The more porous the electrodes, the greater the active electrode surface area will be in contact with the electrolyte and therefore the higher its power density. Alternatively, the more tortuous the electrode, the slower its electronic and ionic diffusion through the electrode material and hence the lower its power density. These two characteristics

are intrinsically connected as was reported by Thorat et *al.* [54]. The porosity of the electrodes confers a capacitance to the electrodes when a potential difference is applied to the cell; the electrodes therefore can be considered as a parallel plate capacitor as described by the Helmholtz model. When the electrical load is removed from the cell, the polarisation of the cell ceases and the electrodes are no longer polarised, the adsorbed ions desorb from the electrode surface and the force of repulsion between these ions becomes dominant. This drives the redistribution of the ions until this repulsion force reaches a minimum. As these ions desorb and move away from the electrode surface, the double layer capacitance decreases, which is detected by EIS test. This decrease in double layer capacitance can occur in the order of milliseconds to minutes depending on the cell type and electrode preparation [157]. When it happens in the order of milliseconds it will not be detected by EIS test results shown in Figure 49; however, if it happens in the order of minutes it will be detected. Moreover, the particles in an electrode will have different concentration of lithium. Particles with a high lithium concentration will give out their excess to a particle with lower lithium concentration. This movement of lithium ions can be opposing to the movement of ions explained earlier. There will be an electromotive force generated by this movement which will create an inductive behaviour which might have a low frequency response. Therefore, the results presented in Figure 49 have the deviation from pure capacitive behaviour at the low frequency end. This behaviour is dominant for the first couple of minutes of relaxation period for cell 1, 2 and 4, and only for first measurement for cell 3 and 5. Cell 1, 2 and 4 are power cell, hence it is likely that the electrodes are more porous compared to energy cells (cell 3 and 4) and have higher capacitance. Therefore, the repulsion force for the ions will be higher and dominate longer for this group of cells, which might be the reason of

the spiral shape shown in Figure 49 (a), (b) and (d), and spiral shape was not pronounced in Figure 49 (c) and (e). However, this phenomenon needs further investigation for a more detailed explanation, which is outlined in future work (Chapter 9).

In addition to this, the ionic diffusion occurs during the redistribution of ions within the electrolyte. This redistribution of ions causes the local concentration within the electrolyte at the electrode surface to decrease until the overall concentration of the electrolyte reaches equilibrium. As the concentration of ions at the electrode surface decreases, when compared to that of the cell under polarisation, the total cell capacitance decreases. Because this change in concentration gradient does not occur instantaneously, but rather occurs over several minutes or hours, the total cell capacitance decreases accordingly as a function of time. Therefore, this phenomenon can be more pronounced and observed for long duration relaxation period (i.e. beyond 10 min relaxation period).

Moreover, in Figure 50, the values of R_o for all cells at selected time intervals are presented. For all 5 cells measured values of R_o fall within experimental error bounds; therefore, can be considered as constant, regardless of relaxation time, cell format, cell chemistry and cell type. This is expected due to the origin of R_o. As mentioned in Section 3.3, R_o is a combination of the resistance arising from the current collectors, separator and electrolyte. The electrolyte used in Li-ion cells has a high salt concentration which ensures high electrolyte conductivity is maintained throughout the life of the cell. In addition, the kinetics of corrosion reaction of current collectors and/or parasitic electrolyte side reactions occur at a much slower

rate in comparison to the length of the experiment or mostly occur when the cell is in operation [49]. Therefore, the resistance component of the electrolyte, and that of the current collectors, would remain unchanged for the experimental conditions. Since R_o is also independent of double layer and electrolyte ionic concentration gradient redistributions, R_o can be considered to be independent of cell relaxation time. This theory is in good agreement with the data presented in Figure 50.

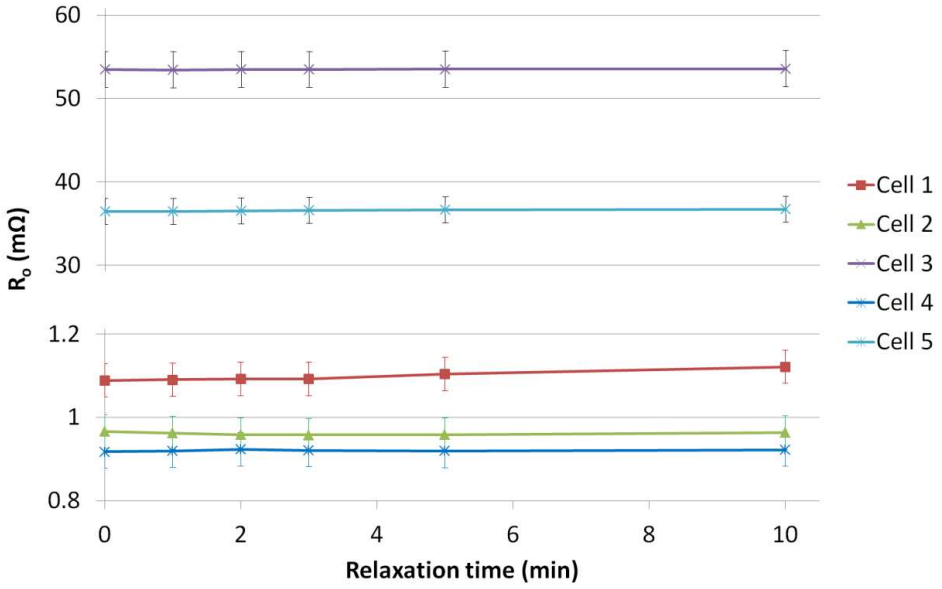

Figure 50: R_o with experimental error as error bar for all the Li-ion cells from 0 min to 10 min. Note that two different scales of y-axis are used.

The variation of the R_o values between cells 1 to 5 arises from the differences in cell characteristics. Although each cell has an NMC cathode, there are differences i.e. the actual intrinsic active material resistance is different, electrode preparation, apparent surface area and capacity (i.e. number of current collectors and electrode thickness) and electrolyte mixture (i.e. solvent mixtures and additives). All of these cell characteristics are the origin of R_o and, thus contributing to the observed variations.

Results presented in this section suggest R_o does not change with relaxation period between 0-10 minutes, therefore could be used as online measurement parameter. However, R_o could not be used as an analogy of SoC as it is expected to have a very low variation with SoC, but expected to change with temperature and age, therefore could be used as an analogy of SoH. In contrast to R_o, total resistance R_T and double layer capacitance C will be inconsistent within 0-10 minutes after cycling. Therefore, when R_T and C are used as a fast on-line measurement parameter, they will produce unreliable results, i.e. SoC and SoH. EIS has been considered for SoC and SoH measurement [81, 82, 104], however, for the first time these results show the possible discrepancy involved.

7.3.2 Long duration relaxation test

The shape of the Nyquist plots (blue plot in Figure 51) obtained for the cells in this study is in accordance with similar Nyquist plots found in the literature [62, 89, 113]. The first EIS data recorded after 10 min of end of discharge to 50 % SoC is similar to the last EIS data recorded after 10 min of SoC adjustment as part of short duration relaxation test (Figure 49). The <1mΩ difference in R_o as shown in Figure 51 is probably due to the calendar ageing happened between two tests. In actual testing the long duration test was performed first then based on the equipment availability the short duration tests were performed. In between cells were stored at 10 °C to minimize calendar ageing, however the cell's R_o has been increased due to ageing mechanisms explained in Section 2.3.4. Moreover, the combined experimental error involved with R_o in two test results shown in Figure 51 is close to 1 mΩ (Figure 50), hence, the variation seen in Figure 51 is within measurement error. Therefore, the small variation seen in Figure 51 could be purely due to measurement error.

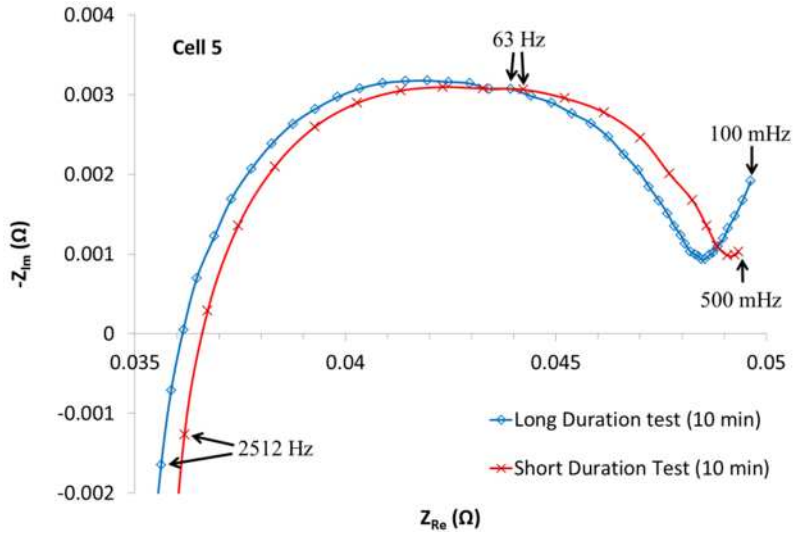

Figure 51: Typical Nyquist plot recorded within this study. Two measurement was performed on same cell with two experimental setup.

To analyse, Nyquist plots can be fitted to an equivalent electrical circuit model. As only one semicircle is present in the test result (the cells are new and therefore minimum SEI, consequently no/very low 2nd semicircle) the equivalent circuit in Figure 31 can be amended for this study, as given in Figure 52.

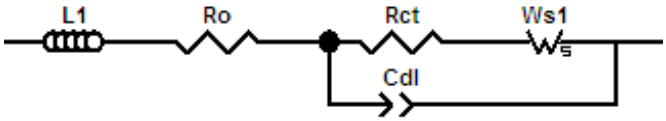

Figure 52: Typical Randles equivalent circuit model showing an inductor (L_1), the pure ohmic resistance (R_o), charge transfer resistance (R_{CT}), double layer capacitance (C_{dl}) and the short finite length Warburg impedance (W_{S1}).

Following the SoC adjustment described in Section 7.2, impedance measurements on the cells were carried out after a defined relaxation period; which ranged from 10 minutes to 15 hours. Figure 53 shows the EIS spectra of all the cell types considered

in this study. Impedance was found to be changing for all the cells tested. Cell 1, 2 and 4 has very low impedance, which is lowest for cell 4, reflecting their type of cell (power cell). Compared to other cells, cell 5 has a much flattened semicircle, which indicates the capacitance had large deviation from ideal operation, and will be reflected in CPE value of the Randles equivalent circuit. These measurements were performed with a low frequency of 100 mHz, therefore based on previously published research [62, 89] it is almost certain that the semicircle visible is Figure 53 attributes to the double-layer capacitance and charge transfer resistance. As the cells were new, SEI layer thickness was deemed to be the lowest possible [43, 52], therefore the semicircle might not be visible separately. The research presented within [62, 158] studies similar cells using EIS at low frequency. This also did not find the presence of a second semicircle at lower frequency and thus attributed the semicircle to the double-layer capacitance and charge transfer resistance.

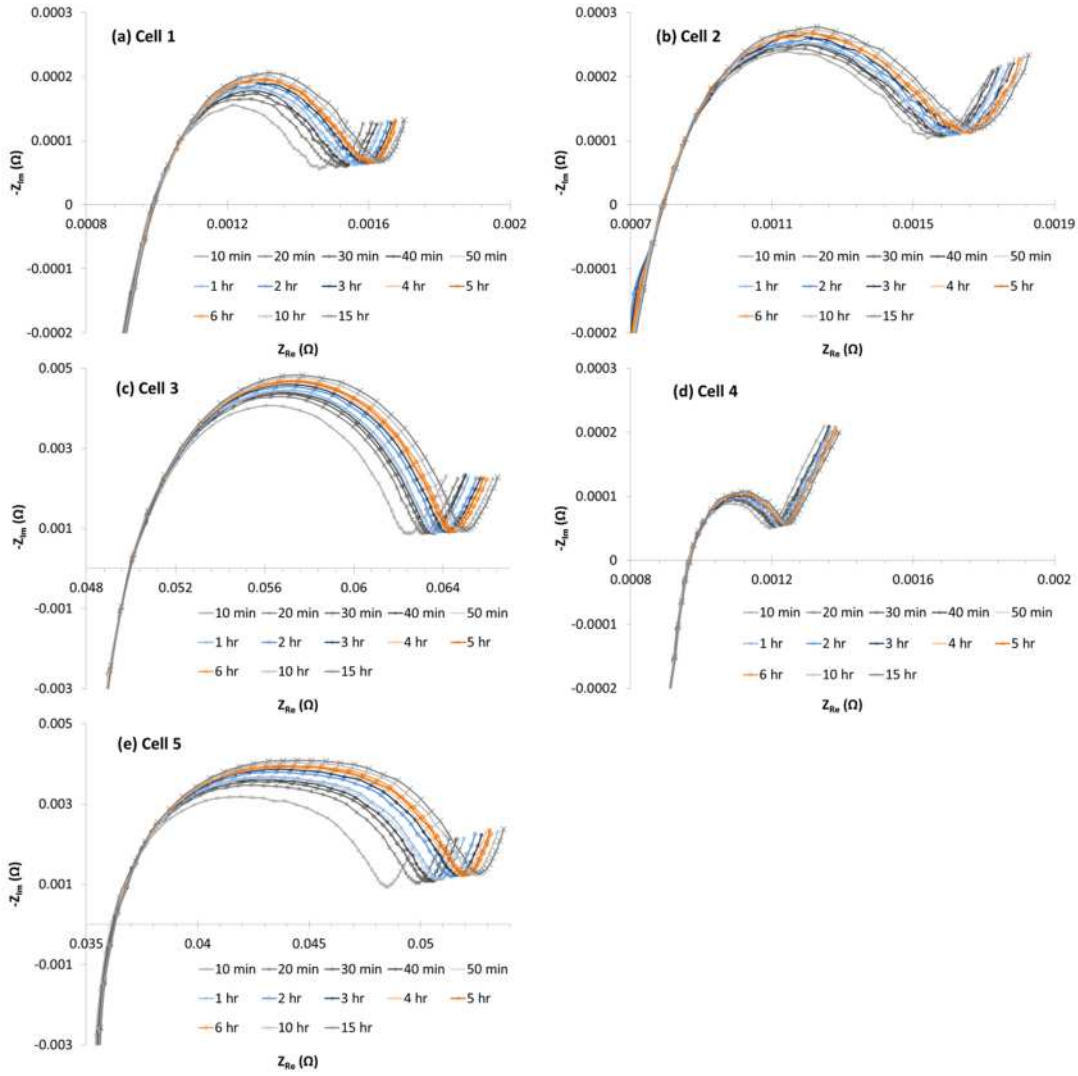

Figure 53: EIS spectra of several Li-ion cells at different relaxation time ranging from 10 min to 900 min after SoC adjustment. Note that different scales have been used for figures (a), (b) and (d), and (c) and (e).

Moreover, in Figure 54, the values of R_o for all cells at selected time intervals are presented following the similar fashion as in Figure 50. This result (Figure 54) is in good agreement with the theory explained in Section 7.3.1 and the data presented in Figure 50, where it is shown that for a given cell all measured values of R_o fall within experimental error bounds, regardless of relaxation time, cell format, cell chemistry and cell type.

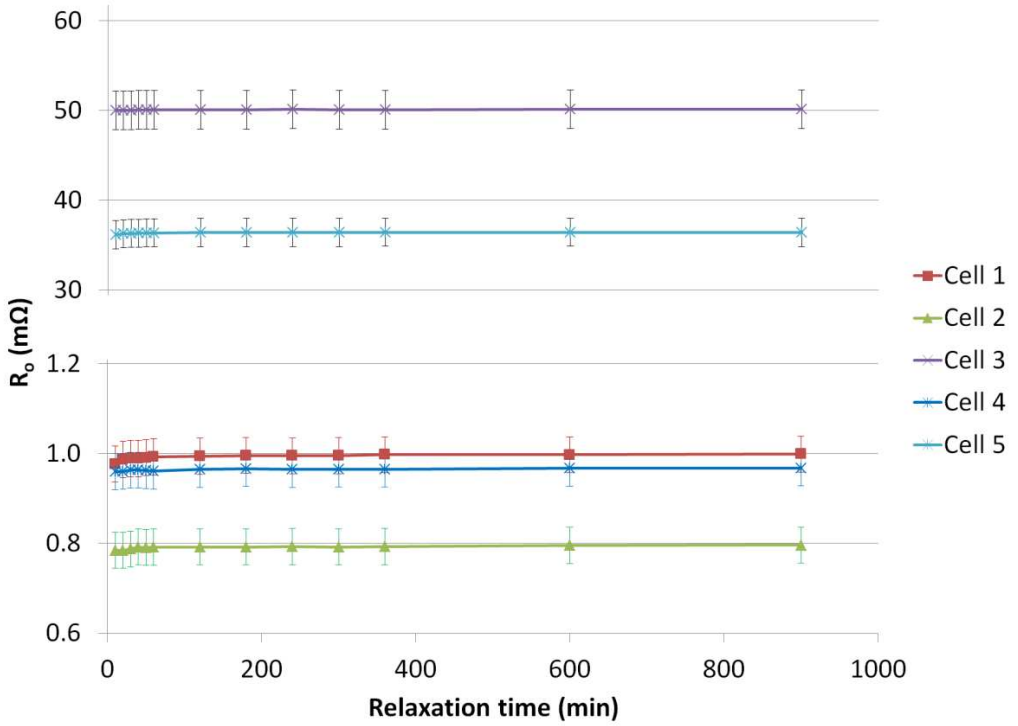

Figure 54: R_o with experimental error as error bar for all the Li-ion cells at selected time intervals. Note that different scales of y-axis are used.

Instead of fitting the Nyquist plots with the equivalent circuit (as given in Figure 52) the total cell capacitance can be estimated from the frequency at the peak of the semi-circle (f_{max}) observed for all cells and using Equation (23). In this method instead of calculating the CPE value, as shown in Figure 52, pure capacitance is calculated. To study the effect of relaxation, both pure capacitance and CPE can be used. Because of the simplicity of the parameter extraction, pure capacitance values were used in this study. This capacitance measured using Equation (23) represent the pure capacitance part of the CPE used in the equivalent circuit shown in Figure 52. The capacitance was calculated for the cells at relaxation periods presented in Figure 53 along with the error. When the electrical load is removed from the cell, the polarisation of the cell ceases and as a result, the cell capacitance decreases. The cell capacitance decreases exponentially as shown in Figure 55. The rate of change of

capacitance depends on the construction of the cell as explained in Section 7.3.1, and therefore will be different for cells 1 to 5. The change of cell capacitance for the cell 1 to 5 is documented in Table 6 along with measurement error. The capacitance decreases for all cells, reflecting the results presented in Figure 53. From Figure 55 and Table 6, it can be seen that after a relaxation time greater than 240 min, the value of the cell capacitance no longer significantly changes and remains within the experimental error bounds.

$$C = \frac{1}{(R_T - R_o) \times 2 \times \pi \times f_{max}} \tag{23}$$

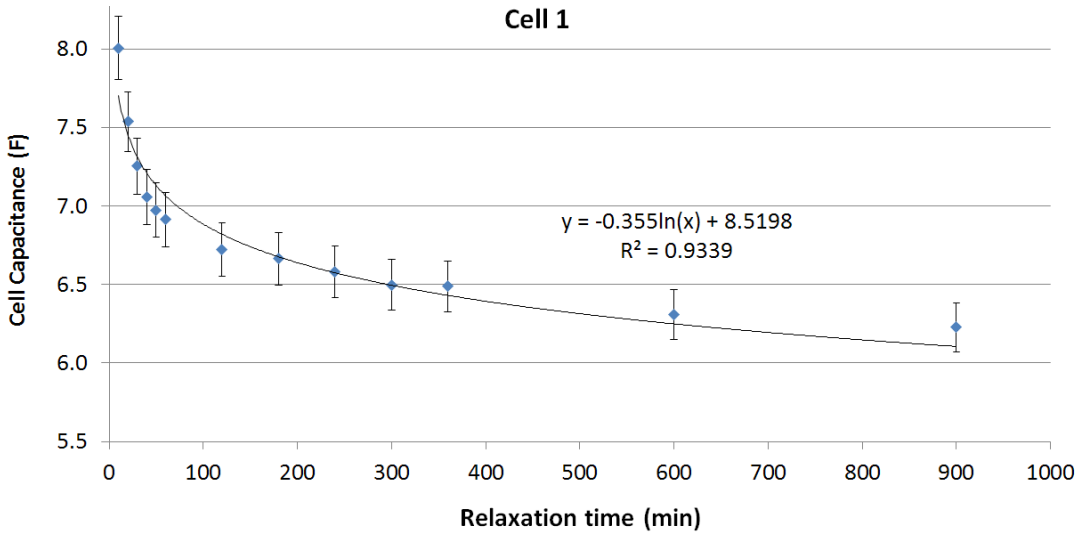

Figure 55: Typical plot of capacitance for Li-ion cell (Cell 1) as a function of relaxation time (Experimental error is shown as error bar).

Table 6: Capacitance with experimental error of Li-ion cells as a function of relaxation time.

Relaxation time / min	Capacitance for cell 1 (F)	Capacitance for cell 2 (F)	Capacitance for cell 3 (F)	Capacitance for cell 4 (F)	Capacitance for cell 5 (F)
10	8.01 ± 0.20	5.203 ± 0.13	0.126 ± 0.003	26.67 ± 0.67	0.162 ± 0.004
20	7.54 ± 0.19	5.056 ± 0.13	0.120 ± 0.003	25.19 ± 0.63	0.147 ± 0.004
30	7.25 ± 0.18	4.996 ± 0.12	0.118 ± 0.003	25.06 ± 0.63	0.143 ± 0.004
40	7.06 ± 0.18	4.987 ± 0.12	0.117 ± 0.003	24.76 ± 0.62	0.141 ± 0.004
50	6.97 ± 0.17	4.939 ± 0.12	0.117 ± 0.003	24.43 ± 0.61	0.139 ± 0.003
60	6.91 ± 0.17	4.904 ± 0.12	0.116 ± 0.003	24.01 ± 0.60	0.138 ± 0.003
120	6.72 ± 0.17	4.836 ± 0.12	0.114 ± 0.003	23.93 ± 0.60	0.133 ± 0.003
180	6.66 ± 0.17	4.775 ± 0.12	0.112 ± 0.003	23.59 ± 0.59	0.131 ± 0.003
240	6.58 ± 0.16	4.745 ± 0.12	0.111 ± 0.003	23.32 ± 0.58	0.130 ± 0.003
300	6.50 ± 0.16	4.715 ± 0.12	0.110 ± 0.003	23.09 ± 0.58	0.129 ± 0.003
360	6.49 ± 0.16	4.683 ± 0.12	0.110 ± 0.003	23.16 ± 0.58	0.128 ± 0.003
600	6.31 ± 0.16	4.610 ± 0.12	0.108 ± 0.003	22.83 ± 0.57	0.125 ± 0.003
900	6.23 ± 0.16	4.567 ± 0.11	0.107 ± 0.003	22.56 ± 0.56	0.124 ± 0.003

In accordance with capacitance, R_T should follow a similar pattern but in the opposite direction i.e. R_T increases as relaxation time increases. Figure 56 confirms the logarithmic relationship of R_T vs relaxation and the R_T values at the similar relaxation time of other cells tested are shown in Table 7.

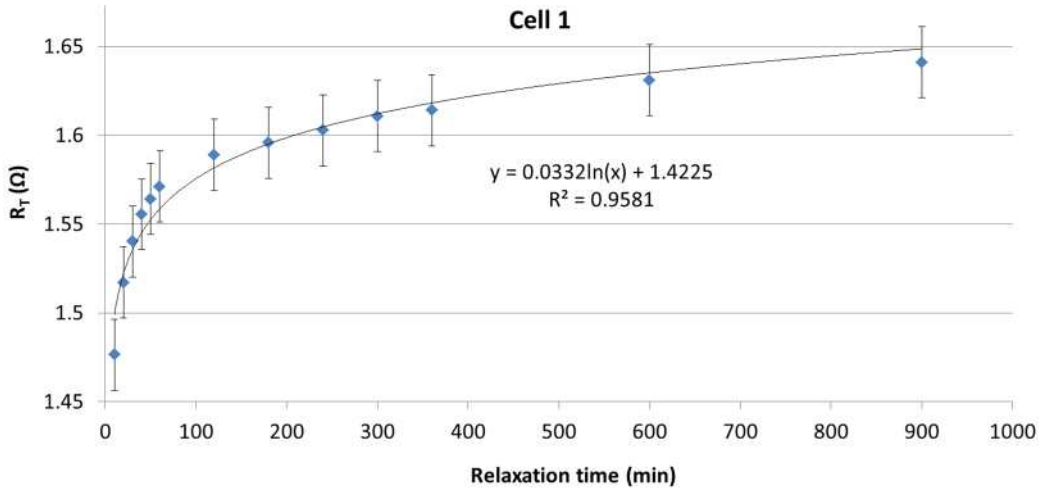

Figure 56: Typical plot of R_T for Li-ion cell (Cell 1) as a function of relaxation time (Experimental error is shown as an error bar).

Table 7: R_T with experimental error of Li-ion cells as a function of relaxation time.

Relaxation time / min	R_T for cell 1 (mΩ)	R_T for cell 2 (mΩ)	R_T for cell 3 (mΩ)	R_T for cell 4 (mΩ)	R_T for cell 5 (mΩ)
10	1.48 ± 0.02	1.55 ± 0.02	62.59 ± 0.84	1.20 ± 0.02	48.55 ± 0.66
20	1.52 ± 0.02	1.58 ± 0.02	63.28 ± 0.85	1.21 ± 0.02	49.86 ± 0.67
30	1.54 ± 0.02	1.59 ± 0.02	63.50 ± 0.86	1.22 ± 0.02	50.31 ± 0.68
40	1.56 ± 0.02	1.59 ± 0.02	63.65 ± 0.86	1.22 ± 0.02	50.54 ± 0.68
50	1.56 ± 0.02	1.60 ± 0.02	63.68 ± 0.86	1.22 ± 0.02	50.74 ± 0.69
60	1.57 ± 0.02	1.61 ± 0.02	63.83 ± 0.86	1.23 ± 0.02	50.87 ± 0.69
120	1.59 ± 0.02	1.62 ± 0.02	64.08 ± 0.86	1.23 ± 0.02	51.42 ± 0.70
180	1.60 ± 0.02	1.63 ± 0.02	64.27 ± 0.87	1.24 ± 0.02	51.69 ± 0.70
240	1.60 ± 0.02	1.64 ± 0.02	64.40 ± 0.87	1.24 ± 0.02	51.87 ± 0.70
300	1.61 ± 0.02	1.64 ± 0.02	64.49 ± 0.87	1.24 ± 0.02	52.00 ± 0.70
360	1.61 ± 0.02	1.65 ± 0.02	64.60 ± 0.87	1.24 ± 0.02	52.10 ± 0.70
600	1.63 ± 0.02	1.66 ± 0.02	64.83 ± 0.87	1.25 ± 0.02	52.39 ± 0.70
900	1.64 ± 0.02	1.67 ± 0.02	65.05 ± 0.87	1.25 ± 0.02	52.69 ± 0.71

The changes exhibited by these parameters are linked to the ionic diffusion occurring during the redistribution of ions within the electrolyte during the relaxation period as explained in Section 7.3.1. To recap, as the concentration of ions at the electrode surface decreases, when compared to that of the cell under polarisation, the total cell

capacitance decreases. Because this change in concentration gradient does not occur instantaneously, but rather occurs over several minutes to hours, the total cell capacitance decreases accordingly as a function of time. These phenomena can be observed in Figure 55 and Figure 56.

Similarly, during the relaxation period, solid state diffusion will occur within the bulk of the particles. This will lead to a rearrangement of the Li atoms within the materials and hence modify their respective electronic properties; thus varying the charge transfer resistance which is reflected in the change observed for R_T.

Figure 57 shows the capacitance value of cell 5 from 0 min to 15 hr of relaxation period. First 0 min to 10 min capacitance was calculated from results shown in Figure 49 (e) and 10 min to 15 hr capacitance was calculated from results shown in Figure 53 (e). Capacitance values at 10min of relaxation recorded by both tests agree with each other. Capacitance decreases linearly from the first 10 mins, then follows a logarithmic relationship. This analysis supports the existence of two different dominating mechanisms as discussed in Section 7.3.1 (repulsion force of ions just after removing load and ionic diffusion in longer duration). Due the ionic diffusion within the electrolyte in longer period (in hours) the local concentration of ions at the electrode-electrolyte interface decrease until the overall concentration reach equilibrium. As the concentration of ions at the interface decrease, the double-layer capacitance decreases. Therefore, the total cell capacitance decreases as a function of time.

Both high power and high energy cells were used as part of this study and both type of cells exhibited similar behaviour with respect to the relaxation time prior to performing an EIS measurement. From the presented results, a period of 4 hours prior to performing EIS measurement would ensure that the variation in R_o, R_T and cell capacitance falls within the experimental error regardless of cell type and chemistry.

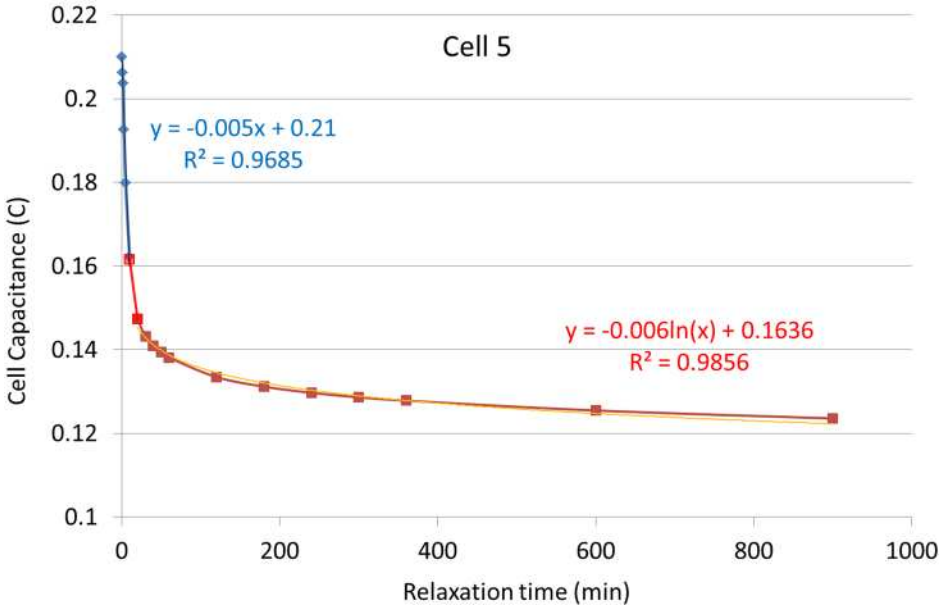

Figure 57: Change of capacitance of cell 5 from 0 min to 15 hr of relaxation period. Blue part was recorded by the short duration relaxation test and red part was recorded by long duration relaxation test.

As discussed earlier in this chapter and in Section 4.2, previously there was no standard way to allow a relaxation period prior to an EIS test. Here in this research, it has been shown that EIS test results varies with relaxation period from minutes to hours, and the electrochemical mechanisms responsible have been discussed. This new knowledge invalidates any comparison with previously published EIS results and any comparison made previously when there was no control over relaxation

period and has clear implication in improvement of accuracy and consistency of EIS tests in future.

7.3.3 SoC dependence of relaxation

As explained in experimental details in Section 7.2, to study SoC dependence of relaxation, a long duration EIS test has been performed at 100 %, 80 %, 20 % and 0 % SoC on cell 1. Figure 58 shows the test results along with the result at 50 % SoC (presented in Figure 53 (a)). Compared to 50 % SoC, the spread of the Nyquist plots do not change a lot at 100 % SoC, 80 % SoC and at 20 % SoC. At 0 % SoC, results are not showing a clear semicircle (which is in accordance to previously published results [109]); however, it can be noticed that relaxation has highest spread in result.

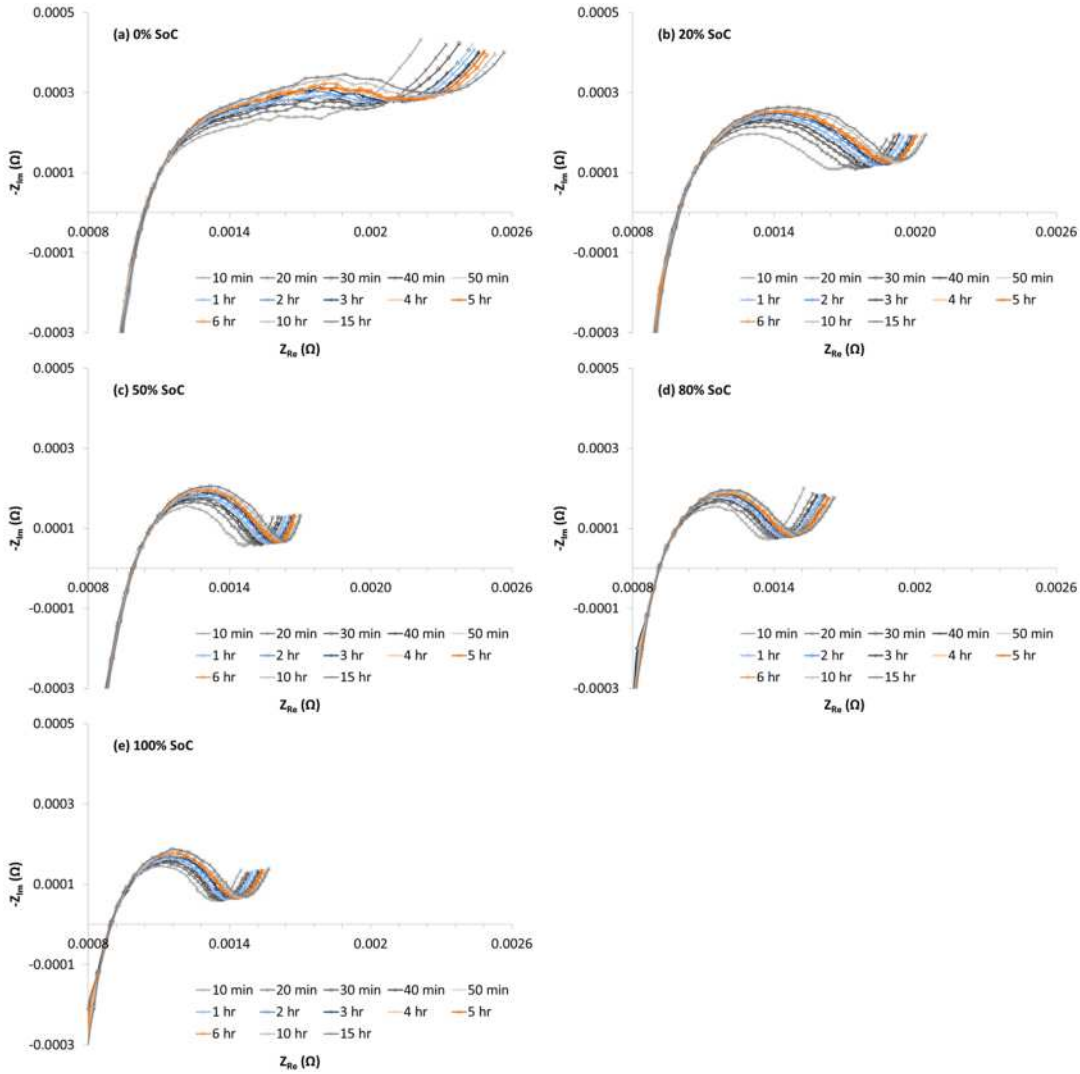

Figure 58: EIS spectra of cells 1 at (a) 0 % SoC, (b) 20 % SoC, (c) 50 % SoC, (d) 80 % SoC and (e) 100 % SoC. Relaxation time ranging from 10 min to 900 min after SoC adjustment.

With reduction of SoC thus proportion of cycle-able lithium at the cathode will be increasing, slowing down further lithium diffusion into the electrode (solid state diffusion) which will be slowest at 0 % SoC. However, with change of SoC a little change in ionic redistribution in the electrolyte is expected. Therefore, increase of relaxation with reduction of SoC is low. At 100 % SoC there is an additional source which reduced relaxation further, which is due to charging protocol used for the test.

To adjust to 100 % SoC the cell was charged only with manufacturer recommended procedure; there was no discharge step. Manufacturer recommended charge procedure (i.e. CC-CV) included a constant voltage part toward the end of charging when lower current is used to charge. Hence, the lithium gets a longer period to diffuse into the electrode, minimizing influence on relaxation of impedance. The change in shape of Nyquist plots at different SoC is due to change in the electrochemical composition of the electrodes and has been explained previously [62, 81, 105, 113].

The results reported here demonstrate that the relaxation of the cell is independent of SoC excluding extreme end of SoC (~100 % and ~0 % SoC), although impedance will vary with SoC. This has clear implication in the use of EIS test. Previously, EIS tests at different SoCs were performed by researchers [62, 86, 104, 109], the findings of this study shows the requirement of same relaxation period prior to EIS measurement for direct comparison.

7.3.4 Discharge current rate dependency

To investigate the influence of discharge current on relaxation, long duration tests have been performed on cell 1 with 0.1C, 3C and 5C discharge current to adjust to 50 % SoC at 25 °C. The results are presented in Figure 59 along with the 1C results presented in Figure 53 (a).

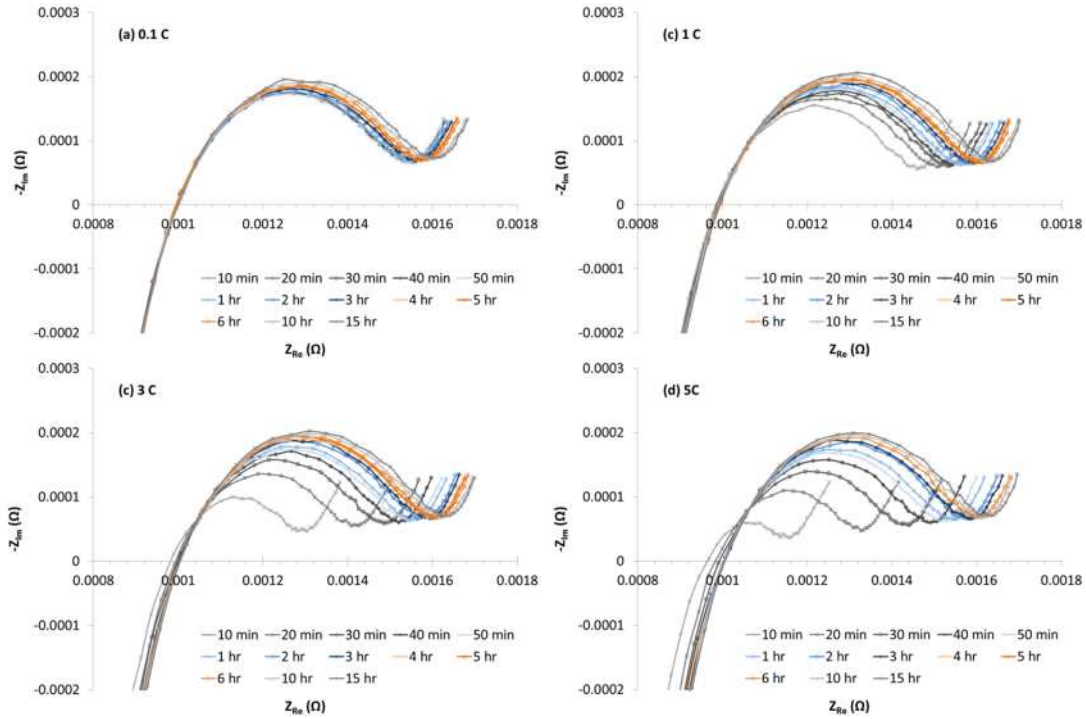

Figure 59: EIS spectra of cell 1 at relaxation time ranging from 10 min to 900 min after 50 % SoC adjustment with (a) C/10, (b) 1C, (c) 3C and (d) 5C discharge current.

Figure 59 (a) shows that the impedance after 10 min was close to the impedance after 4 hr and therefore minimum relaxation happened. On the other hand Figure 59 (d) shows impedance was lowest after 10 min among Figure 59 (a)-(d), which relaxed by the highest amount to reach equilibrium after 4 hours. Also, the R_o which was found to be constant for this cell up until now shows a small increase from 10 min to 20 min results at 3C test and 10 min to 40 min results at 5C test, after that become constant. The change of R_o with discharge rate has been presented in Table 8. After 40 min of relaxation R_o value become the same for all the discharge rates, while it was minimum at 5C after 10 min of relaxation. This reduction of R_o could be due to temperature rise involved with discharge at higher C rates (3C and 5C) [55, 89].

Table 8: Change of R_o as a function of relaxation period at different C rate.

Relaxation time / min	0.1C R_o (mΩ)	1C R_o (mΩ)	3C R_o (mΩ)	5C R_o (mΩ)
10	1.00 ± 0.02	1.01 ± 0.02	0.97 ± 0.02	0.92 ± 0.02
20	1.01 ± 0.02	1.02 ± 0.02	0.99 ± 0.02	0.97 ± 0.02
30	1.01 ± 0.02	1.02 ± 0.02	1.00 ± 0.02	0.99 ± 0.02
40	1.01 ± 0.02	1.02 ± 0.02	1.01 ± 0.02	1.01 ± 0.02
50	1.01 ± 0.02	1.02 ± 0.02	1.01 ± 0.02	1.01 ± 0.02
60	1.00 ± 0.02	1.03 ± 0.02	1.01 ± 0.02	1.01 ± 0.02
120	1.01 ± 0.02	1.03 ± 0.02	1.02 ± 0.02	1.02 ± 0.02
180	1.00 ± 0.02	1.03 ± 0.02	1.02 ± 0.02	1.02 ± 0.02
240	1.01 ± 0.02	1.03 ± 0.02	1.02 ± 0.02	1.02 ± 0.02

At different C rates discharge the ion concentration at the electrode-electrolyte interface is different. Therefore, different amount of ions are re-distributed in the electrode when discharge is stopped; the number of ions increases with current rate. Therefore, relaxation of impedance will be small with lowest current and highest with highest current. However, impedance will be same after adequate relaxation period e.g. 4 hours. Results presented in Figure 59 are in accordance with this theory and has been shown here for first time.

Moreover, internal heat generation (joule heating) increases with increased current. Even though the test was carried out within a temperature controlled environment this extra heat will increase the internal temperature of the cell. The average temperature rise on cell surface at the end of discharge to 50 % SoC (at 25 °C) could be up to 3 °C with 1C discharge, 8 °C with 3C discharge and 15 °C with 5C discharge current. The higher the amount of heat generation (so the surface temperature), the longer it will take for the cell to return set temperature i.e. 5C will

take longer than 3C discharge. Pure ohmic resistance of the cell R_o is dependent on the temperature [89]. Therefore the variation of R_o has been seen in Figure 59 (c) and (d), which was higher and longer for 5C discharge (Figure 59 (d)).

The results presented here show that relaxation affects impedance by a larger amount for a higher discharge rate. However, effect of relaxation is present even with the use of C/10 discharge current to adjust 50 % SoC. Therefore, the requirement of minimum relaxation period cannot be fully compensated with reducing discharge rate. Also, the EIS test commonly used along with other characterisation tests like pulse power test which use very high charge-discharge current. Therefore, when EIS is done after a high current charge-discharge event, much more attention needs to be paid for selection of the relaxation period.

7.3.5 Temperature dependency

To investigate the change of relaxation with temperature, long duration EIS tests were performed at -5 °C, 10 °C and 40 °C after adjusting 50 % SoC with 1C discharge current. Results are shown in Figure 60, which shows at -5 °C the cells impedance changes most with relaxation time, and there is minimal change at 40 °C.

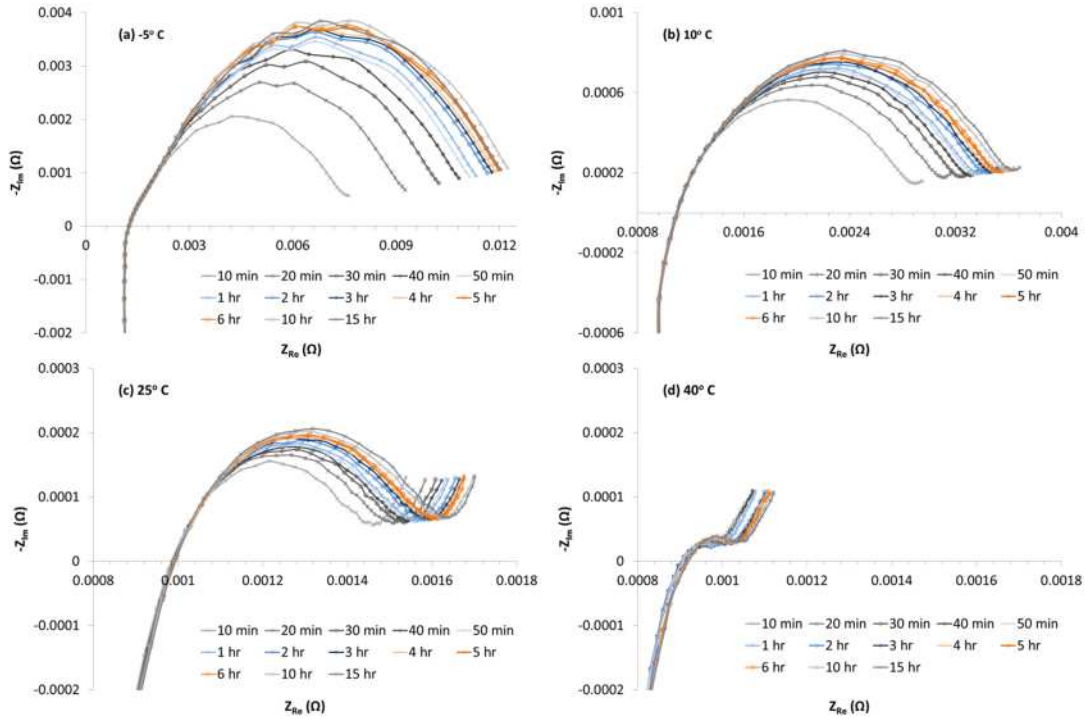

Figure 60: EIS spectra of cells 1 at 50 % SoC at (a) -5 °C, (b) 10 °C, (c) 25 °C and (d) 40 °C. Note that different scales are used in (a) and (b).

In Figure 60 (a) the semicircles are not complete and R_T could not be measured; this is due to the fact that at low temperature R_T occurs at much lower frequency than 100 mHz. The change of impedance after 4 hours among Figure 60 (a) to (d) is due to temperature variation, which has been well understood by other researchers [62, 80, 88, 89, 92, 93, 111, 112]. However, relaxation was faster at higher temperature (narrow spread in Figure 60 (d)) and slower at lower temperature (wide spread in Figure 60 (a)). At the lowest temperature studied (-5 °C) the impedance continue to change even after 4 hour to 15 hour of relaxation period, indicating further research is required at lower temperatures to fully understand the relaxation phenomena.

One of the consequences of lowering temperature is ionic re-distribution and solid state diffusion slow down at low temperature. Therefore it is expected that relaxation

will not follow similar path at all temperature, explaining different spread in Figure 60 (a) to (d).

The results reported here make it evident that although change in impedance with temperature is well known to the scientific community, the change could be influenced by the relaxation period which is more pronounced at lower temperature.

7.4 Chapter Conclusion

In this chapter, the variation of cell impedance as a function of relaxation period after applying an electrical load has been investigated for five different commercially available Li-ion cells. Short and long duration effects of relaxation have been investigated with two different experimental procedures. Also, the disparities of relaxation with different SoC, discharge rate and temperature have been investigated.

It was concluded that the pure ohmic resistance R_o of the cell was independent of the relaxation processes occurring within the cell for both short duration and long duration tests and at all SoC, discharge rate and temperature. This phenomenon has been explained from the origin of R_o in the cell. Therefore, R_o could be used for direct comparison irrespective of the relaxation period used for the test.

For short duration tests, R_T and cell capacitance C were found to be inconsistent within 0-10 minute of relaxation. Therefore, when R_T and C are used as a fast on-line measurement parameter, they will produce unreliable results, which could affect SoC and SoH estimation. This new knowledge shows the possible discrepancy of SoC

and SoH measurement via EIS test done by EIS measurement system integrated as part of BMS, which have been proposed by researchers previously.

From the long duration relaxation tests, it was established that the maximum change of R_T and cell capacitance occurred within the first 4 hours of the relaxation period (i.e. 4 hours after removal of the electrical load). The root causes of these changes have been discussed from an electrochemical point of view; ionic redistribution and diffusion within the electrolyte and solid state diffusion of lithium atoms within the bulk of the materials are the main sources of impedance change during the longer relaxation period.

From the additional test results at different SoC a little change of relaxation behaviour was found. This is because of the electrochemical mechanisms responsible for relaxation remains unchanged with SoC except extreme end of SoC (~100 % and ~0 % SoC).

The increased number of ions involved at higher charge-discharge rate and reduction of diffusion kinetics are identified as the main reasons for higher relaxation of impedance when discharged with high C rate.

With reduction of test temperature relaxation found to be more pronounced. This is due to the fact that ionic re-distribution and solid state diffusion slow down at low temperature.

These new knowledge can provide a guideline for both academic and industrial researchers using EIS as a research and/or diagnostic tool, demonstrating that comparative results can be obtained if a standardised relaxation time is adopted between removal of an electrical load and EIS measurement. To ensure reproducibility and repeatability (i.e. to ensure variation in R_o, R_T and cell capacitance falls within acceptable experimental error), whilst keeping experimental time manageable a minimum relaxation time of 4 hours should be allowed prior to performing an EIS measurement.

8. OCV and OCV hysteresis testing of Li-ion cells

8.1 Chapter introduction

8.1.1 OCV characterisation

The first step toward developing a robust hysteresis test technique and investigating hysteresis is to have an accurate OCV measurement technique. Since the OCV-SoC relation is typically determined empirically it is important that the experiment and subsequent calibration are performed with care.

Usually the SoC is determined via Coulomb counting for which an initial SoC is required. However, the actual capacity of the battery might vary depending on the test technique. Therefore, an error could be embedded into empirically determined SoC, complicating investigation of OCV with the use of SoC. For instance, diffusion limitations are reduced when the cell is charge/discharged incrementally, therefore, it is expected charge/discharge capacity will be different with step size, even at the same temperature and discharge rate. Although the cell is allowed to discharge until V_{min} is reached, assumption of cell has reach 0 % SoC will be incorrect, leading to an erroneous conclusion that OCV-SoC relationship varies with step size. Therefore, use of charge (Q_c) or discharge (Q_d) capacity instead of SoC while investigating OCV can address the issue with capacity variation at different temperature, rate and relaxation period.

Furthermore, recently researchers reported change of OCV with charge-discharge rate [124] and no change with temperature [117]. Both are in contrast to the theory explained in Section 2.3 and Equation (6). Therefore, these two relationships have

been investigated further as part of this thesis using proposed OCV test methodology. Later in this chapter, in Section 8.2.1, the experimental method used as part of this research to investigate the influence of discharge/charge step size, temperature and charge/discharge current rate on OCV_{c} and OCV_{d} characteristic are shown. Subsequently, results are shown in Section 8.3.1.

8.1.2 OCV hysteresis

An incorrect initial SoC value can offset the charge and discharge OCV-SoC curves and incorrectly indicate that hysteresis is present. Therefore, while studying hysteresis it is preferable to use either charge (Q_c), discharge (Q_d) or remaining capacity Q_r as shown in Equations (16), (17) and (18).

The offset between OCV_{c} and OCV_{d} as explained in Section 4.3 can be eliminated by ensuring that the OCV_{c} test characterisation is performed directly after a $\mathrm{OCV_d}$ characterisation. By doing so, the state of the cell for the start of the OCV_{c} procedure, will be the same as when the OCV_{d} ended; eliminating any apparent offset and allowing the true hysteretic magnitude to be assessed. This procedure has been adapted in this thesis to investigate hysteresis. Furthermore, as the cell is first incrementally discharged and then incrementally charged, the OCVs for hysteresis assessment can be plotted against the extracted capacity Q_e which is defined as:

$$Q_e(t) = Q_e(0) + \int_0^t I(t)dt \tag{24}$$

$$I(t) > 0 \quad \text{Discharge}$$

$$I(t) < 0 \quad \text{Charge}$$

The advantage of using Q_e over Q_r for the hysteresis assessment plot is that the initial extracted capacity $Q_e(0)$ can be assumed zero when the cell is fully charged; while the initial remaining capacity value $Q_r(0)$ might not be known for a fully charged cell. The total capacity extracted during the incremental discharge procedure ($Q_{e,max}$) can be used as the cell capacity in subsequent analysis. Note that dividing Equations (18) and (24) by $Q_{e,max}$ gives the corresponding SoC, $z(t)$ of the cell.

$$z(t) = \frac{Q_r(0)}{Q_{e,max}} - \frac{1}{Q_{e,max}} \int_0^t I(t)dt \tag{25}$$

$$I(t) > 0 \quad \text{Discharge}$$

$$I(t) < 0 \quad \text{Charge}$$

Moreover, in general, OCV hysteresis is not expected to be different with current rate if an adequate relaxation period is applied and the current is within the maximum limit of the cell. However, it has been reported previously that hysteresis increases with reduced current rate [124], although the electrochemical explanation of the origin of the difference reported was not provided. Furthermore, any change of hysteresis with temperature has not been reported in literature. Therefore, further investigation of hysteresis with charge-discharge rate and temperature was completed as part of this thesis. Section 8.2.2, illustrates the experimental method used to investigate hysteresis of different chemistry cells and changes with temperature and charge-discharge rate.

8.1.2.1 Introduction of OCV hysteresis into BMS

To provide an example of the improvement of BMS performance by better OCV estimation when accurate hysteresis data is incorporated, a dynamic hysteresis model has been developed which was originally proposed by *G. L. Plett* [119]. As shown in Figure 21, an ECM consists of an ideal voltage source (the OCV) that is a function of SoC. A monotonic static function or a piecewise linear interpolation function, relating the OCV to the cell SoC can be used if the empirically determined charge and discharge OCVs yield negligible hysteresis (in the order of a few millivolts, as many commercially available cell cyclers record to the nearest millivolt).

In the presence of hysteresis, a single static function will not suffice. A model capable of transitioning between the charge and discharge OCV curve is required. A possible approach is to introduce a hysteresis state variable h which is added or subtracted from the average of the charge and discharge OCVs where the average OCV is $\overline{OCV}$.

$$OCV(z) = \overline{OCV}(z) + h \tag{26}$$

The hysteresis state variable h is obtained as a solution to the differential equation given in Equation (27).

$$\frac{dh}{dz} = K(H(z) - h(z)) \tag{27}$$

Here, $H(z)$ is the difference between the charge/discharge OCV and the mean OCV, $H = OCV_c - \overline{OCV}$ or $H = \overline{OCV} - OCV_d$ and is positive when charging and negative when discharging. In Equation (27) K determines the rate at which the hysteresis state $h(z)$ reaches $H(z)$. To simulate the ECM the hysteresis state variable

should however be solved as a function of time, as such the left and right side of Equation (27) is multiplied by $dz/dt = I/Q_n$. To ensure stability of the resulting Ordinary Differential Equation (ODE) the coefficient of h should remain negative and therefore the modulus of I/Q_n is used, resulting in the following expression:

$$\frac{dh}{dt} = K\left|\frac{I}{Q_n}\right|(H(z) - h(t)) \tag{28}$$

Finally for simulation purposes the first order ODE in Equation (28) can be written in a standard discrete time (denoted by subscript i) form as follows:

$$h_{i+1} = h_i e^{\left(-K\left|\frac{I_i}{Q_n}\right|\Delta t\right)} + \left(1 - e^{\left(-K\left|\frac{I_i}{Q_n}\right|\Delta t\right)}\right)H(z_i) \quad i = 0, 1, \ldots \tag{29}$$

To simulate Equation (29) the initial hysteretic state h_0, $H(z_i)$ as a function of SoC and the transition rate K are required. The initial condition h_0 can be set to zero when the charge/discharge history of the cell is unknown and $H(z_i)$ can be determined empirically (from OCV test results). A higher K value implies faster transition between charge-discharge OCV curves. To determine and validate the transition rate K, OCV values occurring in-between the charge and discharge OCV characteristic curves are required. However, as an example a mid-range value of $K = 50$ will be used in this thesis.

The following Sections detail the experimental procedures to evaluate the influence of discharge/charge step size on OCV_{c} and OCV_{d} characteristics and the characterisation of the hysteresis function $H(z_i)$ required for hysteresis modelling.

In Section 8.2, the experimental method used as part of this research is detailed. Subsequently, results of the influence of discharge/charge step size, temperature and charge/discharge current rate on OCV_c and OCV_d characteristic are shown (Section 8.3.1). The hysteresis assessments of the cells are shown in Section 8.3.2. Section 8.3.3 presents the results, analysis of the results and their implications to the model. Finally, the key findings are summarised in Section 8.4.

8.2 Experimental method

Experimental studies were performed on four different types of commercially available Li-ion cells. The chemistry, rated capacity and format of each cell included in this study are listed in Table 9. These cells were unused, having spent ~1 year in storage at 10 ± 3 °C after delivery, therefore can be considered as new. The number of cells tested varied depending on the availability of test equipment; however, a minimum 5 cells were used to get the cell to cell variation.

Table 9: Cell details

Cell Type	Chemistry	Rated Capacity (Ah)	Nominal Voltage (V)	Maximum C rate (10 Sec)	Format	Number of cells tested
1	NMC	40	3.7	8C	Pouch	5
2	LFP	20	3.2	15C	Pouch	6
3	NMC	2.2	3.6	2C	Cylindrical	8
4	NMC - LTO	13.4	2.6	15C	Pouch	8

8.2.1 Discharge & charge OCV characterisation procedure

8.2.1.1 OCV with different step size test procedure

OCV tests were conducted inside a temperature controlled chamber set at 25 ˚C and the charging and discharging of the cells was done via a commercial battery cycler. For the discharge OCV test (OCV_d) the cells were initially fully charged via a CC-CV procedure using a 1C current and C/20 cut-off current. After the full charge, cells were allowed to rest for 4 hours and the initial OCV_d measurement was recorded. The cells were then gradually discharged in 4 % of rated capacity steps using a 1C discharge current until the lower cut-off voltage was reached. After every discharge step, a 4 hour rest period was applied for cell relaxation and the $OCV_{\mathrm{c}}/OCV_{\mathrm{d}}$ was recorded. This process is shown in a flowchart in Figure 61 (a). The length of the rest period is important; a shorter rest interval would not have allowed the battery to reach equilibrium and the recorded OCV at a particular discharge capacity can deviate. The relaxation time should depend on the SoC increment, for example in [115], 6 minutes, 24 minutes and 2 hour rest intervals were used for SoC increments of 0.5 %, 1 % and 5 % respectively. In the procedure described here the incremental OCV method is used with a maximum rest period of 4 hours to estimate the cell OCV. Even after a rest period of 4 hours the cell voltage may not have reached a thermodynamic equilibrium; however, it has been shown in Chapter 7 of this thesis that after 4 hours the electrochemical changes within the cell are negligible.

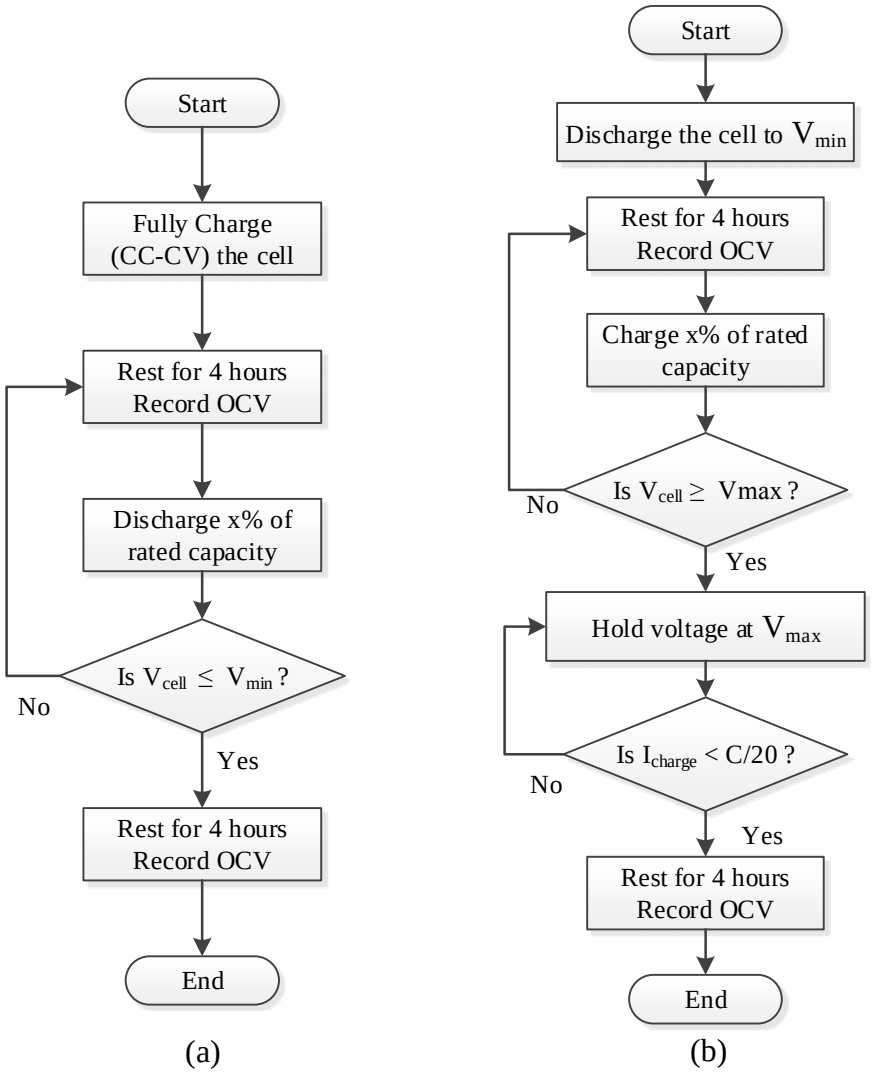

Figure 61: Flowchart for (a) discharge OCV and (b) charge OCV; value of x is 4%, 10%, 25%, 50% and 100%.

The smaller the step size the higher the number of OCV_d points (higher resolution) can be obtained; however, the longer the total test period. The 4 % step size was selected as a trade-off between test duration and resolution of OCV curve. Following a similar procedure the OCV_d tests were also repeated in steps of 10%, 25%, 50% and 100% of rated capacity to study capacity variation with step size and validate the relationship between OCV and discharge capacity as explained in Section 4.3.

For the charge OCV (OCV_c) characterisation, the cells were discharged with a 1C constant current until the cells reached the cut-off voltage. The initial OCV_c value was recorded after a 4 hour rest period and the cells were then gradually charged in steps of 4%, 10%, 25%, 50% and 100% of the rated capacity using a 1C current; a 4 hour rest period was again applied after each step and the OCV was recorded at the end of rest period. As Li-ion cells are normally charged using a CC-CV procedure, when the cells reached V_{max} the voltage was held until the current dropped below C/20. The flowchart of the OCV_c test procedure is shown in Figure 61(b).

8.2.1.2 OCV test procedure at different temperature and charge/discharge rate

To investigate the temperature dependency, OCV tests with 4 % step size were repeated on the LFP cells (cell 2 in Table 9) at 0 °C and 40 °C. Subsequently, on the same cells charge/discharge OCV tests with 4 % step size were repeated with 0.2C and 3C charge/discharge current at 25 °C to access charge/discharge rate dependency. For both instances cells were initially fully charged at 25 °C via a CC-CV procedure using a 1C current and C/20 cut-off current.

8.2.2 Proposed OCV Hysteresis Test Procedure

The proposed test procedure to characterise the level of hysteresis, starts by fully charging the cells using CC-CV method. The cells are then discharged in steps of 4% of the rated capacity with a 1C current and a 4 hour rest after each step discharge until the cut-off voltage V_{min} is reached. The cells are then charged in steps of 4%

with a 1C current and 4 hour rest period after each charge step. When the cell reaches its maximum cut-off V_{max} the cell is held in CV mode until the current reduces to less than C/20, and the test procedure ends. The flowchart of OCV hysteresis test is shown in

Figure 62.

Following the similar procedure hysteresis of the LFP cells were recorded at 0 °C and 40 °C; and at 25 °C with 0.2 C and 3 C charge/discharge current to investigate change of hysteresis with temperature and charge/discharge current.

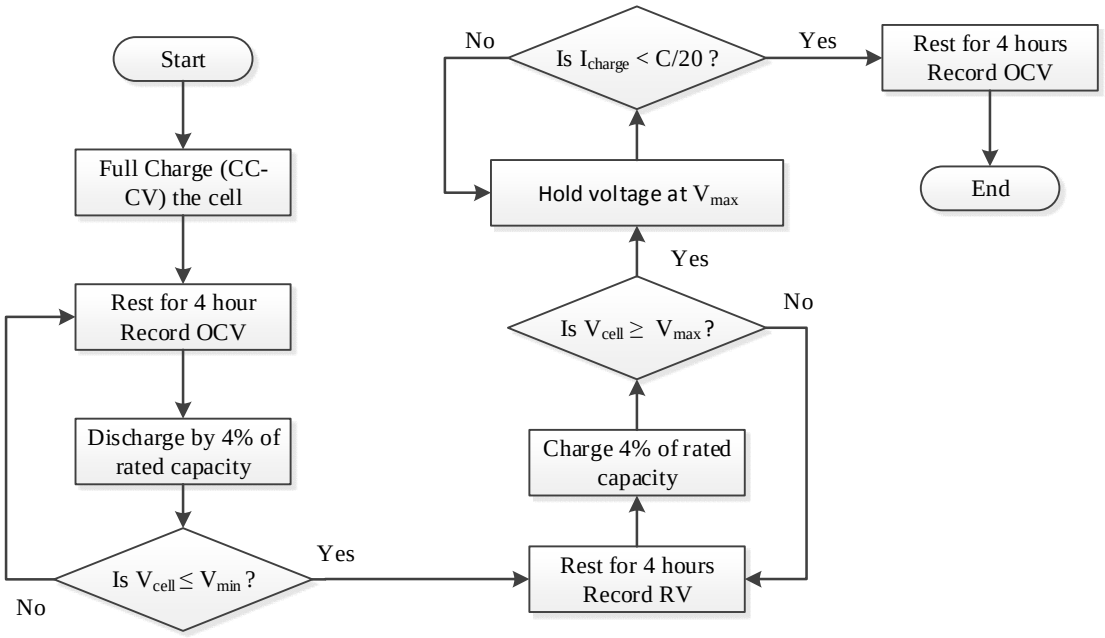

Figure 62: Flowchart for OCV hysteresis characterisation. Compared to Figure 61, OCV_c test process starts just after OCV_d test process.

8.3 Results and discussion

8.3.1 Charge and discharge OCV characteristics

8.3.1.1 Capacity variation with different step size

From the OCV test results with different step size, an increase in total discharge capacity with the decrease in discharge step size was observed. The variation of capacity with step size for all 4 types of cells is shown in Table 10. The capacities shown are the average over the number of cells and the error values represent the 95 % confidence intervals which include cell to cell variation and measurement error. From Table 10, it can be seen that there is capacity reduction of 5.0 % for Cell 1 and 4.1 % for Cell 4 when the cells are discharged continuously at the same C-rate in contrast to a 4 % step discharge. In contrast the capacity variation of Cell 2 and Cell 3 is within the standard error.

Table 10: Total discharge capacity $Q_{e,max}$ with respect to discharge step size

Step Size	Total discharge capacity $Q_{e,max}$ (Ah)			
	Cell 1 (NMC)	Cell 2 (LFP)	Cell 3 (NMC)	Cell 4 (NMC/LTO)
100 %	35.86 ± 0.09	19.17 ± 0.08	2.09 ± 0.01	14.36 ± 0.03
50 %	37.11 ± 0.07	19.19 ± 0.07	2.10 ± 0.01	14.59 ± 0.03
25 %	37.14 ± 0.07	19.19 ± 0.08	2.11 ± 0.01	14.57 ± 0.03
10 %	37.67 ± 0.03	19.26 ± 0.07	2.09 ± 0.01	14.89 ± 0.02
4 %	37.66 ± 0.04	19.31 ± 0.09	2.11 ± 0.01	14.95 ± 0.01
Maximum percentage capacity increase	5.0 %	0.7 %	0.1 %	4.1 %

As a cell approaches complete discharge, a reduction in total discharge capacity with increase in step size can be expected. A larger step size relates to a longer continuous discharge time period which corresponds to higher polarisation effects within a cell [115]. As such the cell terminal voltage can drop rapidly to its cut-off voltage V_{min} ending the test. With a smaller step size the polarisation time is reduced and will in general allow more capacity to be discharged before the cell reaches its cut-off voltage.

The reduction in discharge capacity of Cells 2 and 3 with the 100 % step size is small in comparison to Cells 1 and 4. This suggests that the active material particles are almost fully lithiated when discharged continuously and discharging in 4 % steps only leads to a minor increase in total discharge capacity due to the reduced polarisation time effect. Factors that affect the lithiation process of the electrode active material include porosity, tortuosity, particle size and solid phase diffusion coefficient can affect the lithiation process of the active material [54, 159] . As such the percentage capacity increase via incremental discharge can vary for different cells due to variations in manufacturing processes for the same cell chemistry.

8.3.1.2 OCV characteristics with different step size

Following the similar procedure as used previously in Ref. [114, 115, 120, 122] the discharge open circuit voltage (OCV_d) plotted against the SoC for Cell 1 is shown in Figure 63. It was considered that 0 % SoC is equivalent to when cell reaches to V_{min} at 25 °C with 1C discharge rate. For the simplification of the comparison, result with 4 % ΔQ_n is shown as a solid line with intermediate points as linear interpolation. At 100 % SoC the OCV was same irrespective to step size, because the cells were

charged to 100 % SoC before OCV_d tests using same procedure. However, with the decrease of SoC, the OCV starts to differ at similar SoC, and the effect is largest at 0 % SoC. As explained earlier, this is because of the difference of discharge capacity as presented in Table 10, although in all instances cells had reached V_{min}. This difference is expected to be no longer valid when OCV_d is plotted against the discharge capacity.

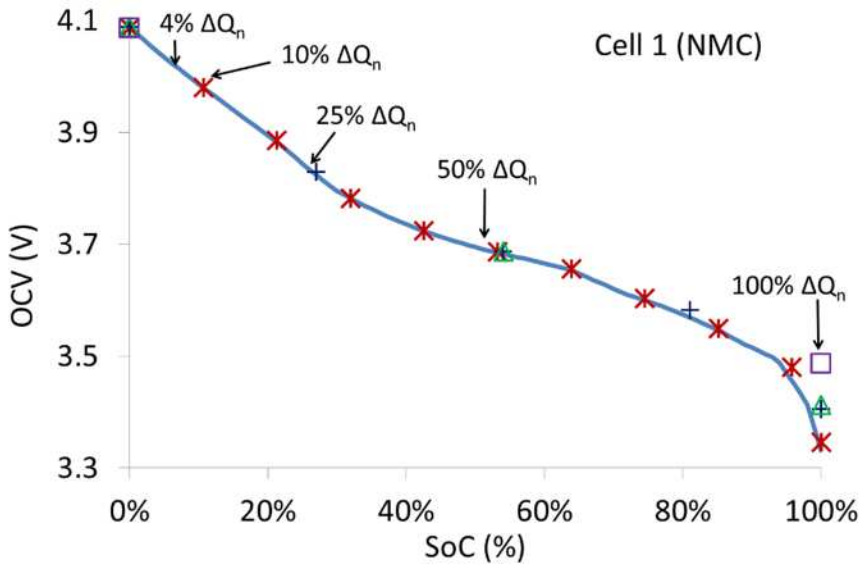

Figure 63: OCV_d as a function of SoC and varying step size for 40 Ah NMC cell.

The discharge open circuit voltage (OCV_d) plotted against the discharge capacity Q_d for Cell 1 is presented in Figure 64(a). In contrast to Figure 63, all the OCV_d recorded by different step tests are consistent at a particular discharge capacity, Q_d point e.g. 20 Ah / 50 % SoC. The only exception is there is a small variation in OCV between 4 % ΔQ_n and 100 % ΔQ_n at the end of discharge. This could be because of the error introduced by linear interpolation done with the 4 % ΔQ_n test result. The gradient of voltage drop close to end of discharge is large; amplifying, the error introduced by liner interpolation. Similar results were also obtained for the other

three cells, as shown in Figure 64 (b-d), indicating that the effect of step size on the OCV_d is negligible. Therefore, depending on the requirement of numbers of OCV points and test duration, any step size can be selected for the OCV test.

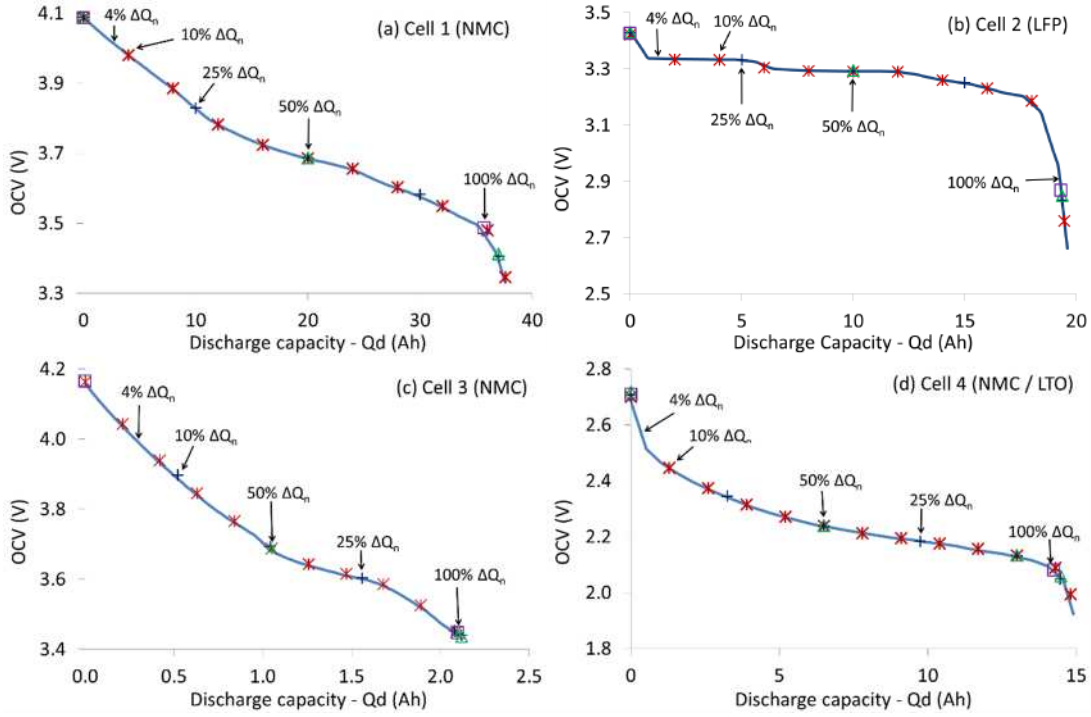

Figure 64: OCV_d as a function of discharge capacity and varying step sizes for (a) 40 Ah NMC cell, (b) 20 Ah LFP cell, (c) 2.2 Ah NMC cell and (d) 13.4 Ah LTO cell.

Figure 65 shows the charge open circuit voltage (OCV_c) against charge capacity Q_c for all of the cells. Similarly to the OCV_d characteristic, the OCV_c recorded by different step sizes are consistent at a particular charge capacity Q_c point. The effect of step size on OCV_c is therefore negligible provided sufficient rest time (~4 hours) is allowed between charge increments for cell equilibration.

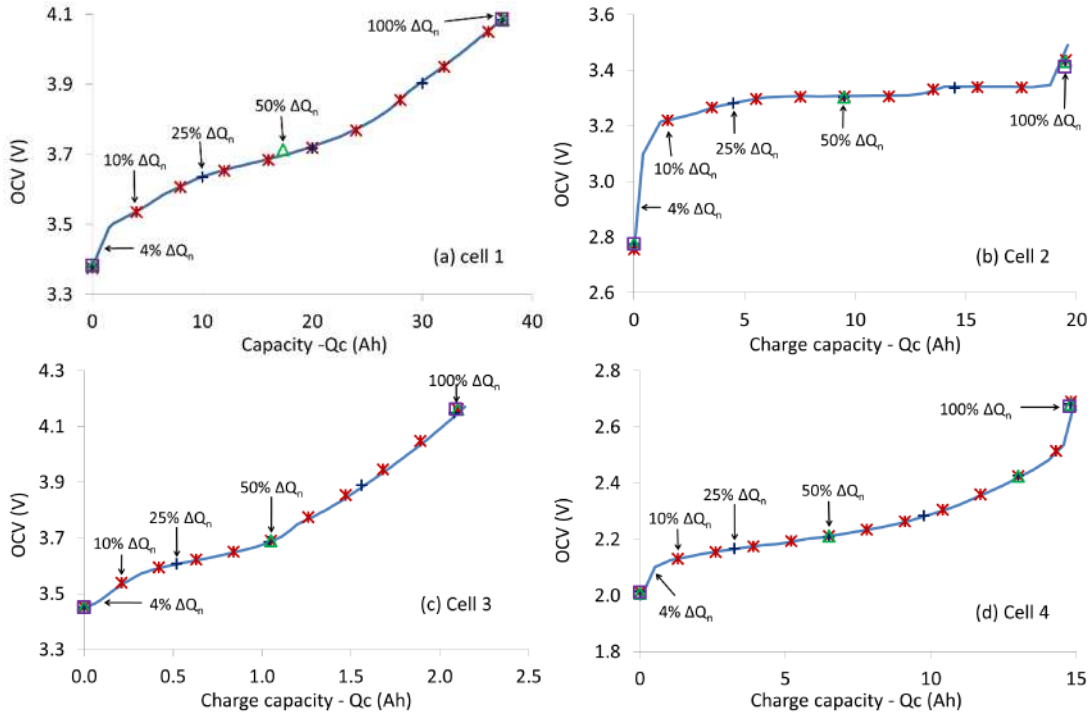

Figure 65: $\boldsymbol{OCV_c}$ as a function of charge capacity and varying step sizes for (a) 40 Ah NMC cell, (b) 20 Ah LFP cell, (c) 2.2 Ah NMC cell and (d) 13.4 Ah LTO cell.

In contrast to the OCV_d tests, the total charge capacities were similar for all step sizes in the OCV_c test, and this outcome can be expected due to the testing procedure. In the OCV_c test, the charging current is allowed to drop when the cell voltage reaches V_{max} (constant voltage (CV) charging) and charging is stopped when the current drops to or below C/20. This procedure charges the cells to a similar total capacity regardless of the step size, since the CV phase dominates the end of the charge for all step size.

From the results presented in this section it can be concluded that OCV has a constant relationship with charge (Q_c) or discharge (Q_d) capacity regardless of the step size, which is explained from theoretical background. However, empirically determined SoC can introduce error; indicating that the relationship varies with step

size. This is new knowledge and has clear implication in development of future OCV tests with different step size depending of application requirement. The 5 % capacity variation observed with different step size is significant for BMS operation, which will contribute to vehicle to vehicle range variation depending on the usages.

8.3.1.3 Temperature dependency of OCV

The mechanism of the change of OCV with temperature has been explained in Section 2.3 from an electrochemical point of view using the Nernst equation (Equation (6). To recap, the log part of the Nernst equation will depend on the amount of oxidised species (C_o) and the amount of reduced species (C_R) in the electrode. For the $LiFePO_4$ cathode the C_o would be $FePO_4$ and the C_R would be $LiFePO_4$, and for the graphite anode, C_o would be C (carbon) and C_R would be LiC_6. Therefore, for the LFP cell, with temperature there will be expected to be a variation in OCV. The relationship between temperature and OCV will be SoC dependent as the ratio of C_o and C_R changes with SoC. In the ideal case, at mid SoC, the ratio will have an average value, minimizing temperature dependency of the OCV. At the higher end of SoC (beginning of discharge curve and end of charge curve), the C_o/C_R is maximum for the cathode and minimum for the anode. Therefore, temperature will have highest influence on the logarithmic part of the Nernst equation for cathode and least for anode. Also, at high SoC, the cathode potential is high and anode potential is low (Figure 14). The opposite phenomenon is present at low SoC, where, compared to high SoC, the anode potential is high and the cathode potential is low (Figure 14), and the ratio of C_o and C_R is minimum for cathode and maximum for anode. However, more complexity is present at lower SoC, anode voltage is still considerably lower than cathode voltage (Figure 13 and Figure 14),

and therefore influence of temperature on cathode still can outplay anode voltage variation. Consequently, at lower temperature, the cell voltage still can be lower (Equation (22).

In recent literature, OCV variation with a temperature reported by *Xing et al.* showed a ~40 mV variation of OCV at mid SoC points with temperature variation of 0 °C to 40 °C and lower variation at higher and lower SoC points [120]. This appears to be in opposition of the theory explained here; however, experimental details indicate the probable cause of this type of variation, as a low C rate charge-discharge OCV test was used the cell voltage is no longer the true representation of OCV (explained in Section 3.4). In another recent study, *Pattipati et al.* concluded that OCV vs SoC remains the same regardless of the temperature studied (-25 °C to 50 °C), although minimum experimental details was offered in the published article [117]. Therefore, it is important to investigate OCV as a function of temperature with a robust test protocol, as proposed in this study.

The results of OCV tests performed as part of this research with 4 % step size on the LFP cells (cell type 2 in Table 9) at 0 °C, 25 °C and 40 °C are shown in Figure 66. The results show the maximum change of OCV is at higher end of SoC regardless of charge and discharge. As explained earlier in this section, with reducing temperature the maximum reduction in cell voltage will happen. It is confirmed from the beginning of the plot in Figure 66 (a) and at the end of the plot in the Figure 66 (b), where, cell voltage is lower for 0 °C. Also, the results presented in Figure 66 (a) and (b) for the middle and lower SoC points are in accordance to the concept developed for low SoC, where, at 0 °C cell voltage is lower. Furthermore, reduction of OCV_d

with temperature was larger than OCV_c which might be related to the interconnectedness of many particles after a discharge/charge event.

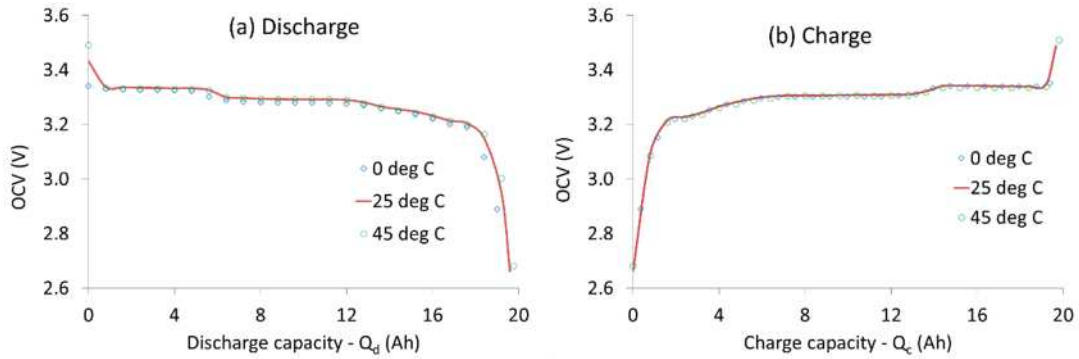

Figure 66: Change in (a) discharge OCV and (b) charge OCV with temperature

In this section, the theory developed implies that OCV will change with temperature, which will be maximum at higher and lower end of SoC and finally OCV will be lower with reduction of temperature at higher end of SoC. This finding does not agree with the previously published results; however, the possible reasons have been discussed. The test results generated using the test methodology developed as part of this thesis shows good accordance with the theory discussed in Section 2.3.

8.3.1.4 Charge-Discharge rate dependency of OCV

According to Equations (22) and (6), OCV is independent of charge-discharge rate used for each charge/discharge step of OCV test procedure, if an adequate rest period is applied. However, *Roscher et al.* reported that there is a change of OCV with the charge-discharge rate used, even after 8 hours of relaxation [124]. They have compared between 0.5C and 10C current and reported after 8 hours of relaxation charge OCV is significantly lower, and discharge OCV is significantly higher for

10C current compared to 0.5C results; however, no electrochemical explanation was offered.

The results of the tests performed with 4 % step size on the LFP cells (cell type 2 in Table 9) at 25 °C with three different C rates are shown in Figure 67. Following the theory, regardless of previously reported results, all the OCV points are in accordance regardless of their C rate, except when they have reached the end of discharge or charge (right hand side of both graphs). This variation could be due to two reasons, firstly, higher heat generation (temperature rise) associated with higher current, leading to increased battery capacity. Secondly, in the last step of discharge, the minimum discharge voltage will be reached earlier with higher current leading to a lower discharge capacity. However, further research is required to identify the exact mechanism.

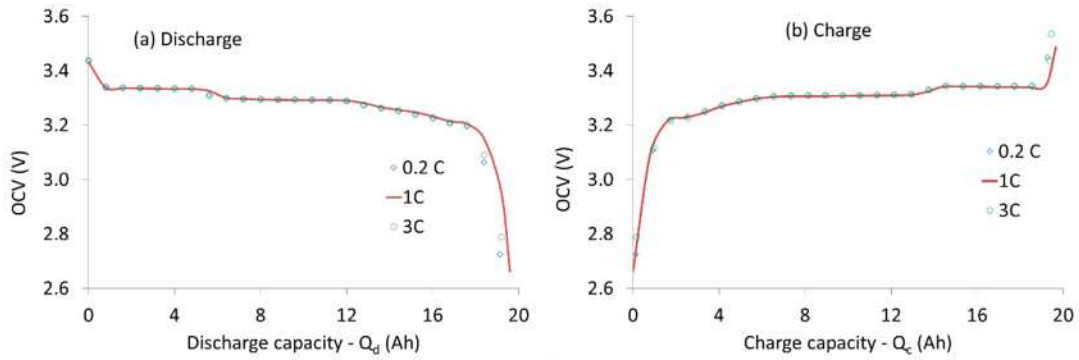

Figure 67: Rate dependency of (a) discharge (b) charge OCV.

Although the results presented in this section does not agree with the previously reported results [124], it is according to the theory of the origin of the OCV within a cell as explained in Section 2.3. This new knowledge will allow the use of any C rate

depending on the cell specification and test requirement for not only the OCV tests but also other tests where OCV is used.

8.3.2 Hysteresis assessment of cells

8.3.2.1 Erroneous hysteresis

In Section 4.3 the possible occurrence of an erroneous hysteretic behaviour was explained; Figure 68 demonstrates such an example. In the figure, the OCVs $\mathrm{OCV_c}$ and OCV_d of Cell 1 are plotted against the remaining capacity Q_r. Note that a 1C continuous discharge was performed to arrive at the 0 % point on the $\mathrm{OCV_c}$ curve while a 4% incremental discharge with rest was performed to arrive at the 0 % point on the $\mathrm{OCV_d}$ curve. The extra gain in capacity from the incremental discharge procedure implies that the remaining capacity ($Q_r(0)$ in Equation (18)) will be different from the continuous discharge. However, if this initial remaining capacity is assumed zero, as often done in literature [114, 120, 122], since the cell reached V_{min}, an incorrect offset between the $\mathrm{OCV_c}$ and $\mathrm{OCV_d}$ characteristic curves is introduced. Figure 68 incorrectly indicates the existence of hysteresis across the full remaining capacity range. Commonly, an average value of this $\mathrm{OCV_c}$ and OCV_d is used without any hysteresis data, as shown in Figure 3 in Ref. [116].

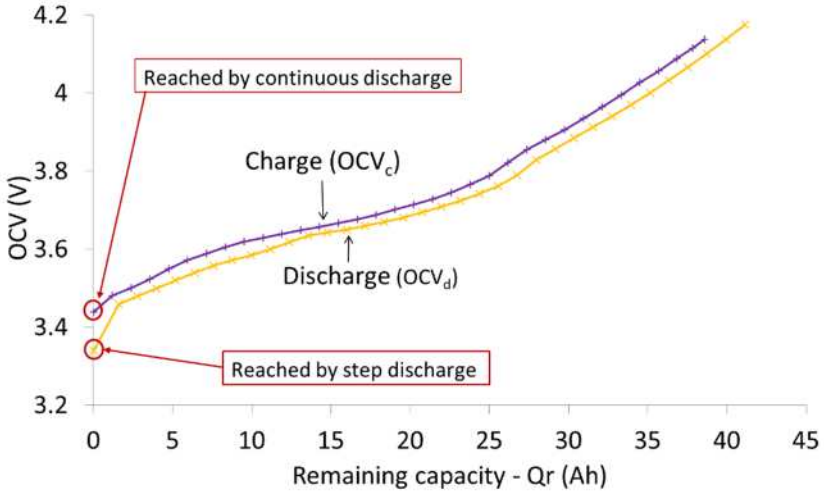

Figure 68: Plot of OCV_c and OCV_d with a misleading assessment of hysteresis when the initial remaining capacity is incorrectly assumed to be zero for cell 1.

8.3.2.2 OCV and hysteresis against SoC

Following the hysteresis characterisation procedure described in Section 8.2.2, Figure 69 demonstrates the OCV_c and OCV_d curves plotted against the extracted capacity Q_e. This approach, as explained earlier in this chapter, leads to a more accurate assessment of the level of hysteresis within the cell.

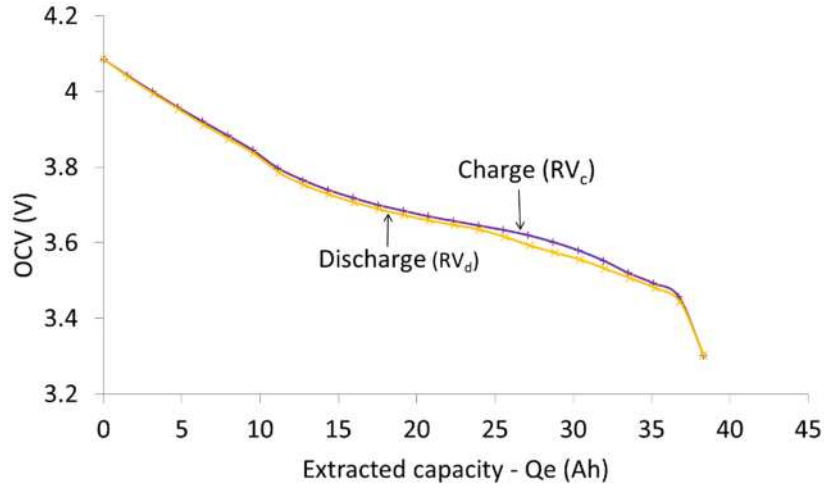

Figure 69: Open circuit voltage as a function of charge and discharge capacity with 4 % ΔQ_n step sizes when initial condition was matched for 40Ah NMC cell

In comparison to Figure 68, Figure 69 indicates that the level of hysteresis is not significant across the full extracted capacity range. Furthermore, from the test procedure an estimate of $Q_{e,max} = 38\text{Ah}$ for the cell maximum extracted capacity is obtained. This value can be used to calculate the SoC via Equation (25) with $Q_r(0)$ set to 38Ah.

The charge and discharge OCV curves against SoC for Cells 1-4 are shown in Figure 70 and the hysteresis voltage as a function of SOC is shown in Figure 71. Though the cells are discharged in uniform steps, the last OCV_d data point is decided when the cell reaches V_{min} for which the extracted capacity can be less than the step size. Similarly, during charge the capacity added when determining the last OCV_c data point can be different from the predefined step size. The measured OCV_d and OCV_c data points will therefore not be determined at the same SoC. As such, the OCV_c and OCV_d curves are linearly interpolated to a reference SoC spanning from 0 to 100 % in increments of 1 % SoC in order to calculate the hysteresis voltage as shown in Figure 71.

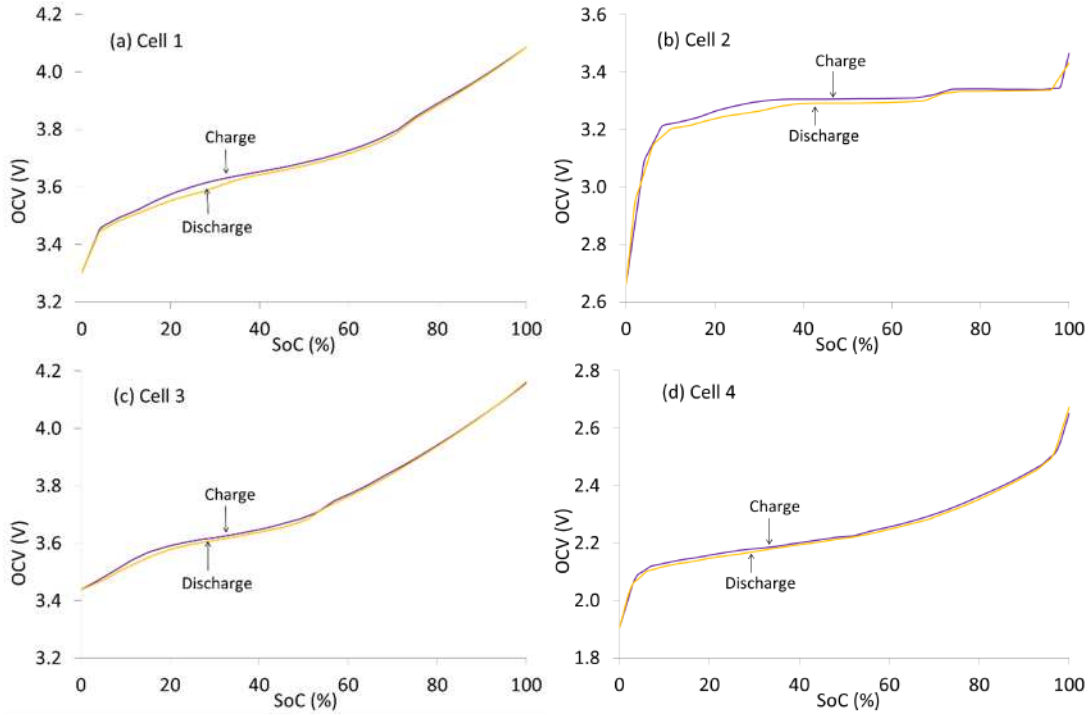

Figure 70: OCV_c and OCV_d against SoC for (a) 40 Ah NMC cell, (b) 20 Ah LFP cell, (c) 2.2 Ah NMC cell and (d) 13.4 Ah LTO cell.

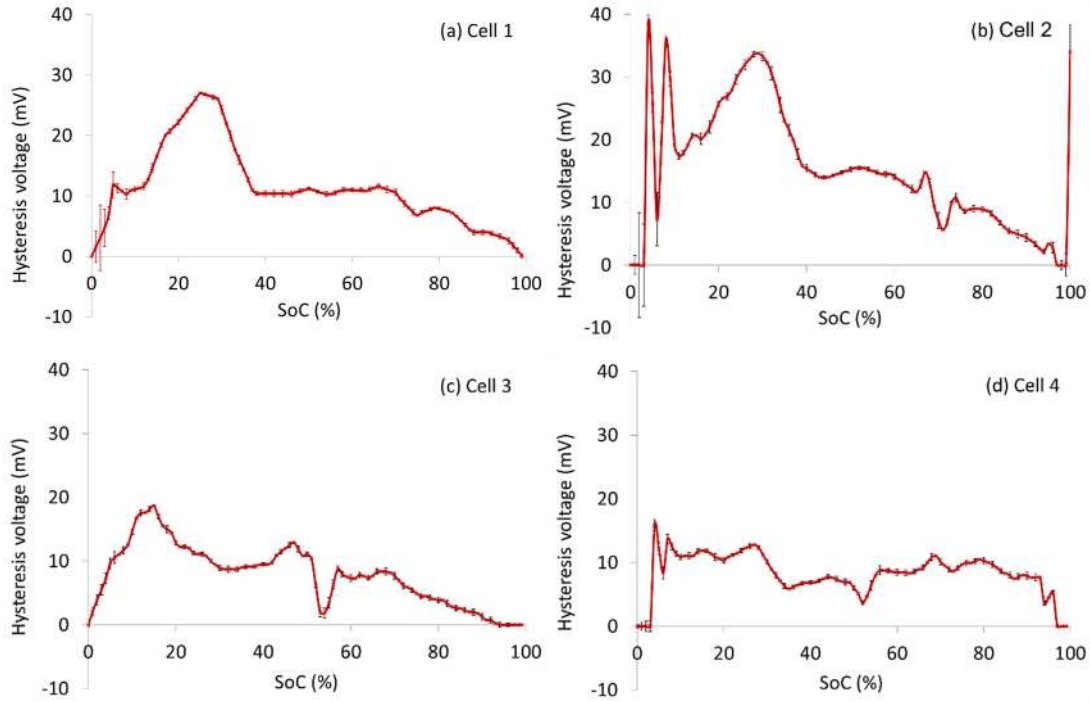

Figure 71: Hysteresis voltage vs SoC for (a) 40 Ah NMC cell, (b) 20 Ah LFP cell, (c) 2.2 Ah NMC cell and (d) 13.4 Ah LTO cell. Error bars shows standard error among cells tested.

Referring to Figure 71 (a), a hysteresis voltage of at least 10mV is present from 5 % to 70 % SoC and peaks to a maximum of 27mV at 25 % SoC. From 70 % SoC hysteresis starts to decrease until 100 % SoC. A similar hysteresis voltage was obtained for all the remaining Cell 2 and Cell 3 (Figure 71 (b) and (c)). Cell 4 showed comparatively lower but similar hysteresis voltage over entire SoC window. The maximum hysteresis and their corresponding SoC are shown in Table 11. In general, maximum hysteresis was found within the 5 % to 25 % SoC range of all the cells tested.

Table 11: Maximum hysteresis and corresponding SoC

Cell Type	Chemistry	Hysteresis voltage (mV)	Corresponding SoC (%)
1	NMC	27	25
2	LFP	38	5
3	NMC	19	15
4	NMC (LTO anode)	16	5

Cells 1 to 3 showed similar shape of hysteresis; and they have similar anode material (carbon). Whereas cell 4 which has LTO anode showed a little different shape of hysteresis voltage vs SoC graph. Therefore, hysteretic behaviour could be dependent on the anode material, which requires further research. However, the results presented in this section indicate that OCV hysteresis assessment should not only be restricted to Li-ion LFP chemistry active material batteries, but also to NMC and LTO batteries as well if the modelling error of a subsequent battery ECM is to be reduced.

8.3.2.3 Temperature dependency of hysteresis

Hysteresis voltage of LFP cell (cell 2) at different temperature is shown in Figure 72. Although the results at 25 °C and 45 °C are similar, at 0 °C the cell has significantly higher hysteresis. This phenomenon was not discussed by the researchers previously and Figure 72 shows a requirement of further research with a wider temperature range to match with operating temperature window of EVs. The interconnectedness of many particles with a non-monotonic chemical potential function as suggested by *Dreyer et al.* [127] could be affected by the temperature. More specifically, distributing the lithium ions to neighbouring particles and decreasing its chemical potential could be affected at lower temperature. If it is the case then reduction of OCV_d will be comparatively higher than OCV_c at low temperature, increasing hysteresis voltage. According to this hypothesis, as interconnectivity of many particles will be affected in a similar fashion at lower temperature, the shape of hysteresis voltage vs SoC is expected to be same, which was the case found in Figure 72. However, further research can validate the hypothesis.

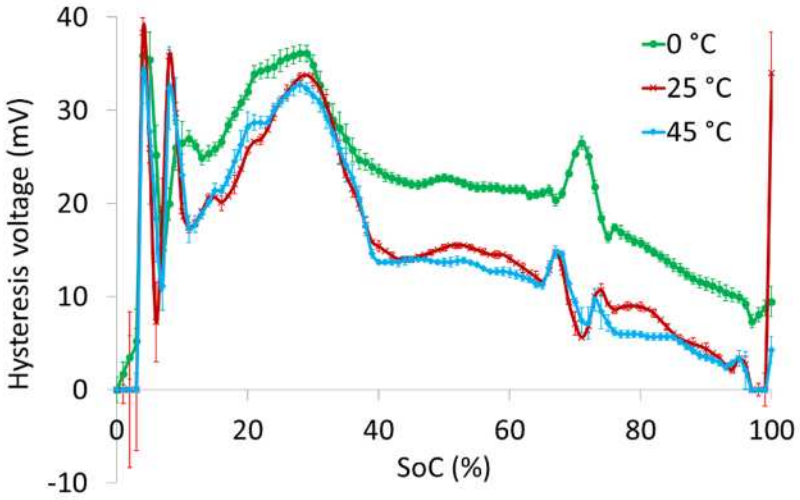

Figure 72: Change in hysteresis voltage with temperature. Error bars shows standard error among cells tested.

8.3.2.4 Discharge rate dependency of hysteresis

Figure 73 present the hysteresis voltage of LFP cell (cell 2) with different charge-discharge rates. Although hysteresis with 0.2C was ~4 mV higher than other 2 cases from 15 % SoC to 30 % SoC, however, for the remaining SoC they are within the cell to cell variation (error bars). The ~4 mV difference in hysteresis voltage in 15 % SoC window is not significant for any conclusive explanation of origin, therefore may require further investigation. Referring to the hysteresis voltage for the remaining 85 % SoC it could be considered as independent of charge-discharge rate. These results are in good accordance with the results presented and theory outlined in Section 2.3, Section 3.4.1 and Section 8.3.1.4.

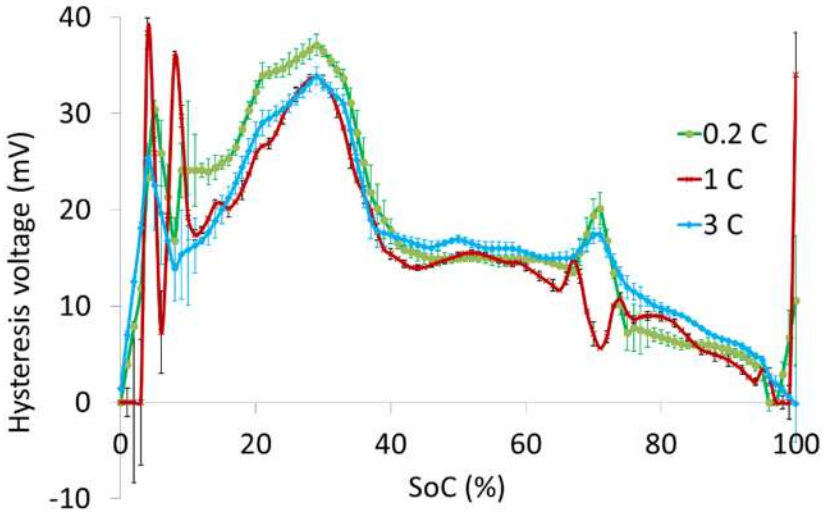

Figure 73: Change in hysteresis voltage with charge-discharge rate. Error bars shows standard error among cells tested.

8.3.3 OCV hysteresis and model simulation: a case study

A dynamic model for hysteresis was presented earlier in this chapter and an empirically determined hysteresis voltage as a function of SoC was presented. The model (Equation (29)) can now be simulated to evaluate the rest-voltage transition. Cell 1 (NMC) and its hysteresis voltage (Figure 70 (a) and Figure 71 (a)) are used as an example in the following section to illustrate the simulation.

To assess the hysteresis transition, a scenario is considered where the initial SoC is assumed to be at 30% and then the battery is fully charged to 100%, discharged to 10% and charged back to 30%. The corresponding current profile and SoC against time graph is shown in Figure 74. This scenario was selected to represent a typical EV usage window i.e. overnight charging, daily usages including recharge before travelling to base/home. In the absence of prior knowledge of a cell's charge/discharge history the initial hysteresis state is assumed zero ($h_0 = 0$) and the OCV for the initial SoC is the average value of $\mathrm{OCV_c}$ and OCV_d i.e. 3.610 V. Two cases are considered with regards to the hysteresis voltage $H(z_i)$. First, as often assumed in literature [119, 160], $H(z_i)$ is set to a constant and set equal to half the maximum hysteresis voltage, which for Cell 1 is $H(z_i) = 13.5\mathrm{mV}$. Secondly it is set equal to half the empirically determined hysteresis voltage (shown in Figure 71) and assumed to be a function of SoC. As stated for Equation (29), to set the transition rate K, OCV data points occurring in between the $\mathrm{OCV_c}$ and OCV_d curves are required. In the absence of intermediate OCV data the rate was set arbitrarily to a middling value $K = 50$ in the simulation.

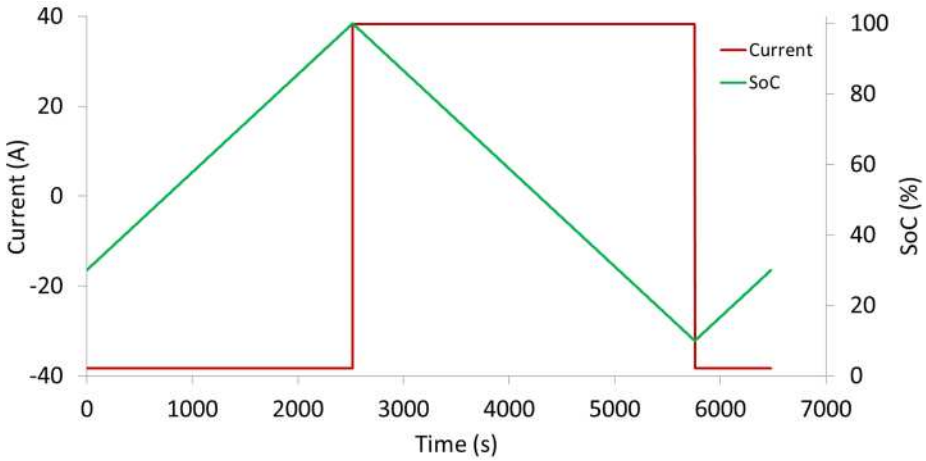

Figure 74: Simulated scenario for hysteresis transition. The battery model, starting from 30%, is fully charged, discharged to 10% and charged back to 30%.

Figure 75 demonstrate the outcome of the hysteresis model transition with the hysteresis voltage assumed a constant $H(z) = H_{max}$. Setting the hysteresis voltage to a constant the model overshoots both charge and discharge OCV. It is expected because of hysteresis voltage changes widely over the SoC range as shown in Figure 71. When hysteresis voltage is assumed to be a function of the SoC the model follows the empirically determined OCV_c and OCV_d characteristics, Figure 76.

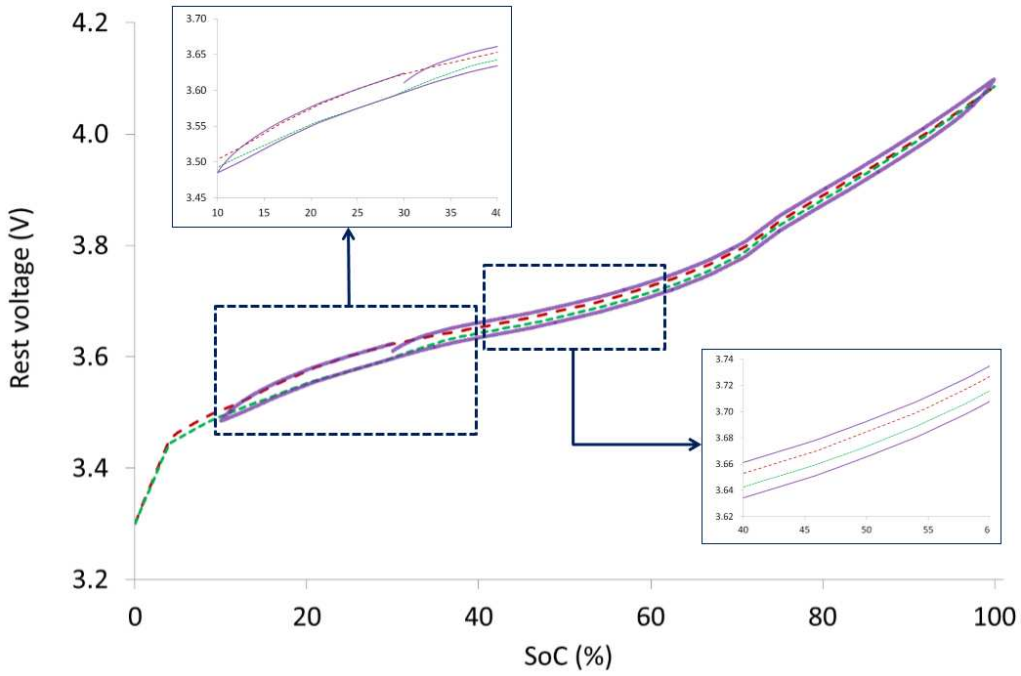

Figure 75: Hysteresis model transition with the hysteresis voltage assumed a constant $\boldsymbol{H(z) = H_{max}}$. The transition model can deviate from the $\mathbf{OCV_c}$ (red) and $\boldsymbol{OCV_d}$ (green) characteristic curves.

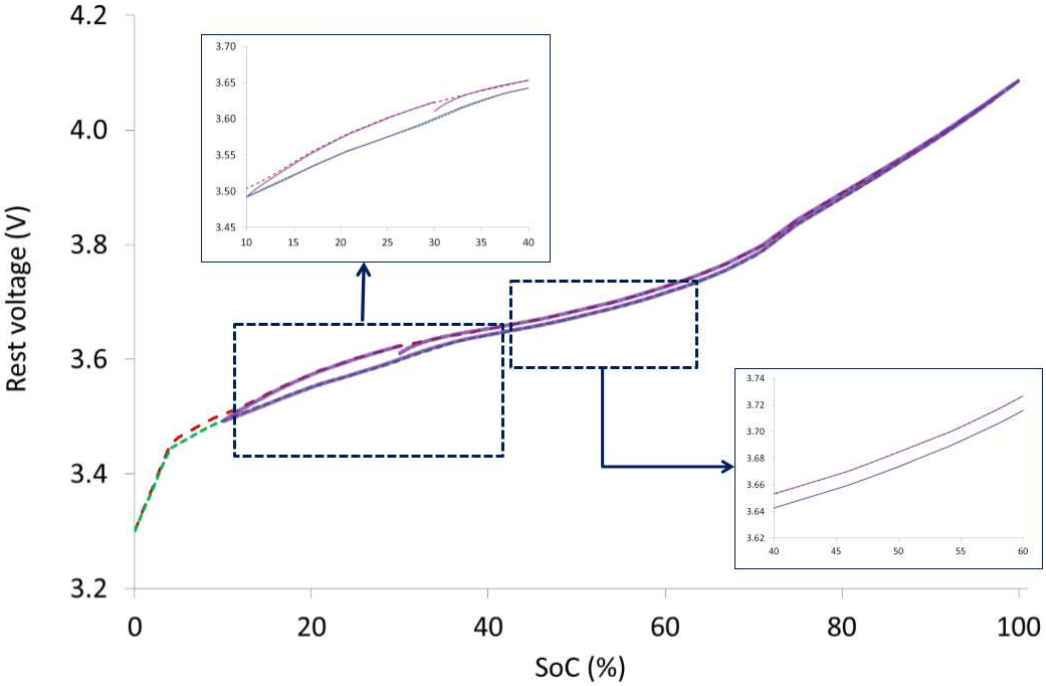

Figure 76: Hysteresis model transition with the hysteresis voltage $\boldsymbol{H(z)}$ assumed to be a function of SoC. The transition model follows the $\mathbf{OCV_c}$ (red) and $\boldsymbol{OCV_d}$ (green) more closely.

Better OCV estimation is achieved in the second case (Figure 76) compared to the first case (Figure 75) because of the accurate hysteresis voltage for any particular SoC point is incorporated to the model. Figure 77 shows the corresponding error between the model and the OCV_c and OCV_d curves as a function of time for the two cases. For Case 1, the error starts at 12mV but rapidly decreases and overshoots to an error magnitude of around 10mV and higher deviations (approximately 25mV) are observed when the current changes direction causing the model to transit immediately to the other curve. For Case 2, the OCV error again starts at 12mV and rapidly falls close to zero as the model transits towards the OCV_c curve and remains close to zero. The error deviates when the current changes direction causing the model to transit on to the OCV_d curve.

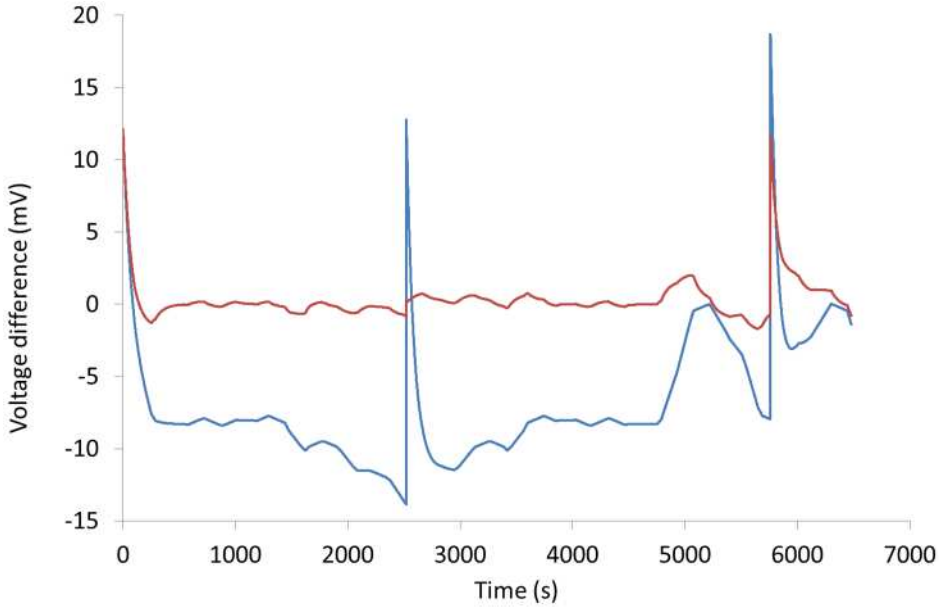

Figure 77: Voltage difference between transitioning OCV and $\boldsymbol{OCV_c}$ and $\boldsymbol{OCV_d}$ curves. Blue line: Case 1, constant hysteresis simulations; Red line: Case 2, adaptive hysteresis.

Work by earlier authors [119, 160] have assumed a constant hysteresis voltage and usually only for LFP batteries. In contrast, the empirically determined OCVs and hysteresis transition model presented here highlight that hysteresis assessment is not only restricted to LFP and to assume a constant hysteresis voltage over the full SoC will contribute towards an error when simulating the battery voltage. Figure 77 shows the improvement of OCV estimation can be achieved when hysteresis characterisation is performed and as per the methodology outlined in this thesis and incorporating that data into modelling. Therefore, the hysteresis voltage should be characterised as a function of SoC when modelling the OCV element of an ECM battery model and subsequent use in a BMS.

8.4 Chapter Conclusions

Researchers have been using step OCV test procedure to asses charge and discharge OCV of the Li-ion cell. The total discharge capacity in generally found to be increasing with the decrease in discharge step size (i.e. increase of number of step), which was not reported previously. The main cause of this capacity variation has been identified as the reduced polarization due to the additional rest steps in-between the discharge phase of the test. The effect of step size on the measured OCV_c and OCV_d plots is negligible, provided they are plotted vs capacity, not SoC as usually seen in literature.

In contrast to the recent literature the variation of OCV_c and OCV_d with temperature is found to be in accordance with the theory of origin of OCV. OCV was comparatively lower at low temperature over entire SoC, which was decreased to its

lowest at highest SoC. This new knowledge has a clear implication in BMS design for EVs operating wide range of temperatures.

Previously, it was reported that OCV changes with change in C rate, which is in contrast with the electrochemical origin of OCV. In this thesis, both OCV_c and OCV_d was found to be independent of charge-discharge rate used. These findings can reduce complexity of OCV estimation by a BMS.

Current OCV hysteresis test methodologies do not provide an accurate measure of hysteresis. Multiple reasons have been identified as the root cause, i.e. inadequate use of rest period, capacity variation with test procedure, offset of OCV_c and OCV_d plots. As part of this thesis a new test methodology has been proposed which will address the root causes and accurately assess OCV_c and OCV_d, subsequently, hysteresis.

Via the proposed methodology, the OCV and level of hysteresis of four Li-ion battery types were studied. In hysteresis assessment, not only LFP cells but also other three types of cells have shown hysteresis. The LFP cell (Cell 2) showed the highest level of hysteresis and the NMC cell with LTO anode (Cell 4) had the least level of hysteresis. In general, maximum hysteresis was present close to end of discharge (low SoC) for all the cells tested. The interaction of many particles with non-monotonic chemical potentials explains how hysteresis can occur in other Li-ion chemistries in addition to LFP. As not only LFP but also other battery chemistries are currently being considered for EVs, therefore this new knowledge will improve the BMS performance and subsequently performance of EVs.

It was found that hysteresis increases with decreasing temperature, keeping the shape of hysteresis vs SoC. It is due to the decrease of OCV_d with temperature is larger than OCV_c. However, as expected from theory, hysteresis is not affected by charge-discharge rate.

From the results obtained, a dynamic hysteresis model has been evaluated to provide an example of the enhancement can be achieved using the results generated following the methodology proposed in this thesis. The inclusion of the hysteresis voltage as a function of SoC, rather than a constant, shows how the Plett's model predicts the empirically determined $\mathrm{OCV_c}$ and OCV_d characteristics more accurately.

The methodology and results reported in this chapter demonstrate that careful consideration of the experimental methods, such as the charge/discharge procedure of a battery, is required to measure the OCV characteristics and allow subsequent assessment of hysteresis. The corresponding OCV characterisation methodology proposed here will lead to more consistent OCV curves within an acceptable experimental time and effort. Therefore, this methodology will be a useful reference for both industrial and academic researchers for further research with lithium-ion battery.

9. Discussion and Future Direction

9.1 Introduction

The proposed improvements in the area of capacity test, EIS test and OCV test as presented consecutively in Chapters 6, 7 and 8 will overall improve the consistency, accuracy and interpretation of battery characterisation test results. The contribution to knowledge include introducing a new parameter (relaxation period) into testing (EIS); including real world scenarios (e.g. current de-rating, drive cycle) into the test procedure (capacity test); and improving existing model performance with an updated parameter (hysteresis as a function of SoC). This chapter presents the overall discussion and significance (Section 9.2) of the new knowledge for academic and industrial research with Li-ion batteries and thus the future development of EV. Logical and natural extensions of this work are discussed and suggestions are made at the end of the chapter (Section 9.3).

9.2 Discussion

To predict instantaneous electrical performance of the battery pack, BMS use ECMs. The commonly used ECM of a Li-ion battery cell is shown in Figure 21. The discrete components (resistance, inductance and capacitance) of the equivalent circuit are commonly parameterised using EIS results; open circuit voltage, V_{OCV}, from OCV test results and finally capacity from capacity test results. Therefore, these three tests are important for ECM parameterisation, thus operation of BMS.

The anxiety of EV users over driving range is one of the main barriers to the widespread adoption of EV. One of the key tasks of BMS is to accurately estimate

remaining driving range (RDR) of the EV, related to the battery capacity. Researchers and development engineers have considered many ways to estimate RDR reliably and accurately. Conventionally the BMS has adopted capacity in Amp-hours (SoC) and translates the remaining capacity into RDR [116, 141, 142, 161]. Since vehicle speed is directly related to the power delivered to the wheels, and distance travelled is directly related to the energy, thus RDR is directly related to the remaining energy (SoE), not SoC. To recap, SoC indicate battery capacity in Amp-hour which is measured by coulomb counting ($\int_0^t i\ dt$), whereas SoE indicate battery capacity in Watt-hour, measured by counting power ($\int_0^t v * i\ dt$). One of the possible reasons of use of SoC is that SoC has been historically used for static energy storage devices (e.g. UPS using lead-acid battery) and the technique of SoC estimation is well established [116, 139, 140, 162]. However, in real world scenarios, the estimated range through Amp-hours has a discrepancy with actual driving range, increasing the range anxiety of the driver as reported in [14, 129, 130]. These authors reported the drop of driving range shown in EV dashboard is much higher than the actual distance travelled by the EV. Although this variation could be from a different source (e.g. driving behaviour as reported by *Birrell et. al.* [14]), use of SoC might be one of the main reasons. In Chapter 6 it has been shown through experimental evidence that existing real world discrepancy in RDR estimation in EV through SoC can be improved by using SoE instead of SoC. With reliable range estimation, the driver's range anxiety could be reduced and thus have more trust in the vehicle, therefore improving brand value. Use of SoE will be advantageous not only for automotive applications but also other applications like grid storage, requiring accurate measure of remaining energy. This proposed method (use of SoE) is different from the previous method (use of SoC) and thus new knowledge.

Providing the theoretical and experimental evidence, Figure 46 of this thesis presents total capacity in Watt-hour of a battery is linearly related to the average current of short-term cycling history of the battery, which was not reported in earlier literature. Figure 47 reports that the linear relationship is valid for not only constant current but also for dynamic duty cycles and in scenarios where current de-rating is employed. Short-term cycling history could be considered as current/power demand due to driving since the last full charge. Thus taking the average current of current/power demand (which is different among drivers due to individual's acceleration and braking behaviour), the range of a particular vehicle can be estimated more accurately. Previously *Birrell et. al.* reported range prediction accuracy is dependent on driving behaviour, 'more aggressive driving style lead to greater inaccuracies' [14]. This is possibly due to the fact that existing methodologies gave less importance to the driving behaviour and short-term history of current/power demand (e.g. since last full charge). As the new methodology proposed in this thesis accounts for average current of the duty cycle (which represent driving behaviour) to calculate driving range, thus RDR estimation is expected to improve. Moreover, for known routes it will achieve better estimation of energy consumption (further explained by *Padma Rajan* [163]), hence further accuracy of range estimation. In addition, as average current is considered, there will be no dramatic change in estimated range (as reported by *Birrell et. al.* for the existing technique) for high current/power demand for short durations like hill climbing, acceleration to join motorway, etc. thus reducing the fluctuation in range and hence driver's concern.

A battery pack's current/power de-rating toward the end of discharge is a commonly used technique to maximise battery capacity, and thus RDR e.g. Nissan Leaf limits

power transferred to the motor towards the end of driving range [164]. Lower electrode polarisation due to lower discharge current enables more capacity to be discharged before reaching minimum voltage limit; further explained in Chapter 2. It has been presented in this thesis that through de-rating though the capacity in Amp-hours can be maximised, however, capacity in Watt-hours cannot be maximised; due to irreversible Joule heating (I^2R loss), potentially explaining the discrepancy in range estimation in real world scenarios [14, 129, 130]. SoC is calculated using coulomb counting technique which is not dependent on Joule heating; however, SoE calculated from Watt-hours is directly affected by Joule heating (Equation (21)). Thus the de-rating technique will work effectively when employed with Watt-hours (SoE). Therefore, incorporating SoE into BMS, remaining range display on the dashboard of an EV could be modified for different driving pattern like city driving (Artemis Urban), motorway driving (Artemis Motorway). Implementing this will require BMS to gather vehicle's current/power demand continuously, enabling real-time update of estimated driving range.

The discrete components of the ECM are often considered as representing different electrochemical processes within the cell like pure Ohmic resistance, charge transfer resistance and double layer capacitance [50, 86, 89, 91, 92]. EIS allows each parameter to be identified individually, thus parameterising an ECM, therefore EIS is in widespread use for model parameterisation [62, 89, 92]. The discrete parameters also change with the change of electrochemical processes within the cell due to ageing. This makes EIS a popular choice for periodical characterisation test, as part of long duration ageing tests [58, 62, 83]. Although in extensive use, limited attention has been given towards understanding the effect of relaxation time prior to

performing an EIS measurement. The systematic variation of cell impedance as a function of relaxation period has been reported for the first time in this thesis. Thus when EIS is used without considering relaxation period the results are not comparable, potentially invalidating ageing results reported using EIS.

The change of charge transfer resistance and double layer capacitance in longer duration EIS tests (10 min to 15 hours) follows the exponential relationship (Figure 57); where, capacitance decreases and resistance increases due to mainly diffusion within the electrolyte and solid state diffusion of lithium atoms within the bulk of the materials. The relaxation is more pronounced at higher C rates (Figure 59) due to higher number of ion involvements, however it remains similar over the entire SoC range (Figure 58). On the other hand, relaxation becomes slower at lower temperatures and faster at higher temperatures (Figure 60) due to change in kinetics of ionic re-distribution. ECM parameterisation for low temperatures (-20°C to 0°C) has been done by *Momma et al.* [89] with EIS tests performed only after 2 h relaxation period and other researchers also done similar work with EIS tests performed after 1 to 3 hours of relaxation [62, 90, 99]. However, the results presented in this thesis indicate that at low temperatures even after three hours of relaxation EIS test results varies considerably, therefore the ECM parameterisation will be different. For example, when EIS test is performed after 1 hour of relaxation, Nyquist plot is smaller compared to the one recorded after 4 h or longer when the cell reaches equilibrium (Figure 60 (a)). When Nyquist plots are different, discrete parameters identified through curve fitting will be different. Consequently, ECM performance thus the performance of BMS at low temperatures will not be as good as at room temperature. Also, the ageing results presented by researchers using EIS

could be different as EIS tests was done only after 1 h of relaxation [58, 99] or without considering relaxation period [83, 95, 110]. For instance, when standardised relaxation period is not used, Nyquist plots could be different even at similar ageing state and could be same when ageing state is different, showing an apparent increase/decrease of ageing. For example, Figure 78 shows the change of EIS spectra as reported by *Zhang et al.[58]*. If a longer relaxation period was applied a bigger semicircle in Nyquist plot (as indicated with dotted line in Figure 78), thus higher R_{ct} and lower C_{dl} could have been observed (as shown in Section 7.3.2), thus higher ageing. This new knowledge indicates researchers using EIS as a measurement or diagnostic tool needs to standardise the relaxation period. The proposal made in this thesis i.e. standardised relaxation period (e.g. 4 hours) after removing electrical load will ensure comparative results are obtained.

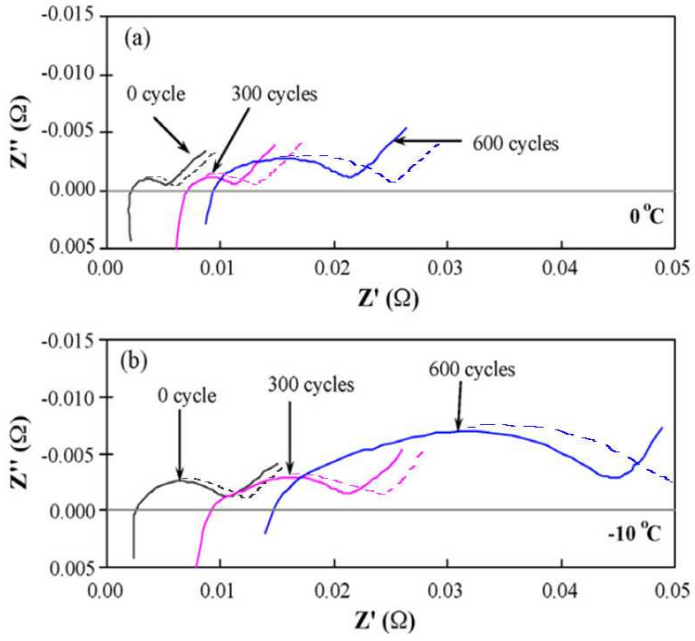

Figure 78: Impedance spectra of a cell at (a) 0 °C and (b) -10 °C at 70 % SOC at different ageing state as reported in [58], solid lines are as reported and dotted lines are prediction if a longer relaxation period was used to reach equilibrium.

This standardised relaxation period will also be applicable to the test scenarios where the cell needs to reach electrochemical equilibrium before a measurement/further testing (e.g. OCV test, pulse power characterisation (PPC) test). When the OCV test is done in steps (as done by researchers previously and in Chapter 8 in this thesis) cells are allowed to reach electrochemical equilibrium before taking an OCV measurement. This study confirms that 4 hours will be long enough for the cell to reach acceptable equilibrium during OCV test. For PPC tests short duration pulses (e.g. 10 second) are applied, separated by 10 minute to 1 hour of relaxation period [25-27, 97, 102]. To calculate internal resistance of the cell, cell voltage prior to the start of the pulse current which is considered to be OCV and end of pulse current are commonly used. This thesis has shown that 10 minutes to 1 hour is not long enough to reach electrochemical equilibrium. Hence, the pulses are not performed at equilibrium state and the OCV recorded at the beginning of the pulse is not a true representation of OCV. One example from the literature is shown in Figure 79, where *Ecker et al.* [83] reported voltage response to the pulse current. It is clear that the cell voltage was still relaxing, thus the cell did not reach equilibrium before the charge pulse started. This could be the root cause of the over estimation of cell resistance measured by PPC test compared to EIS test, reported by *Waag et al.* [62]. Therefore, the 4 hour relaxation period could be used to update the PPC test as well. This has wide reaching implication for the characterisation of Li-ion cells for both academic and industrial researchers.

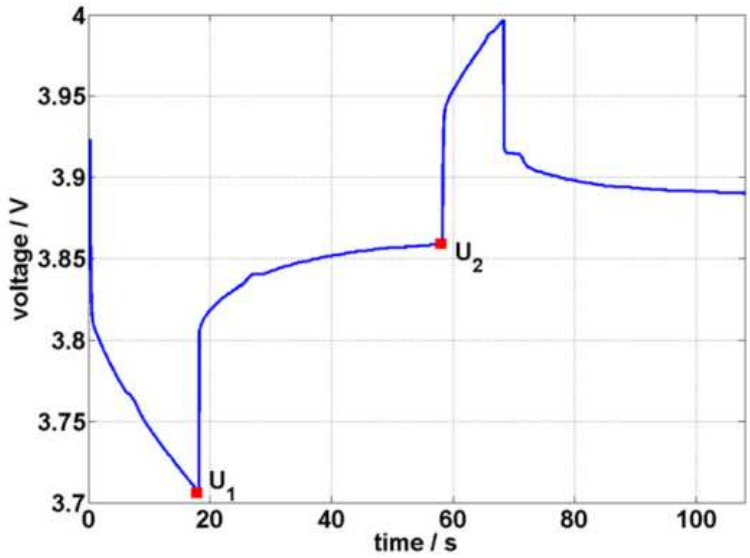

Figure 79: Voltage response to the high pulse power characterisation profile reported by *Ecker et al.* [83].

In addition to use of EIS test results to parameterise discrete components of ECM, it has been considered as an on-line measurement technique as part of BMS [55, 81, 82, 104]. However the relaxation period after removing an electrical load is of critical importance for these types of applications. In this thesis (Chapter 7) it has been shown that as a fast on-line measurement technique EIS is unreliable. This is because the Nyquist plot shows a spiral shape and changes considerably with the relaxation period of 0-10 min. The spiral shape disappears after a maximum 10 minutes of relaxation, see Figure 49. Before this study, there was no literature reporting this type of deviation of Nyquist plot from the commonly reported shapes. The spiral shape of Nyquist plots indicates dominating presence of inductive behaviour over capacitive at low frequency, which is in contrast to the previous knowledge of Li-ion cells. Therefore, fast change in current flow with drive cycle will be reflected by change in cell voltage. For the same reason when direction of current flow changes with regenerative charging within a drive cycle, batteries will

be charged with reduced efficiency compared to normal constant current charging where there is no intermediate discharge event. Due to this spiral shape, the value of charge transfer resistance and double layer capacitance becomes inconsistent, producing unreliable results when employed as part of BMS as a fast on-line measurement technique. Neither this inconsistency nor the dominating inductive behaviour of Li-ion cells was reported in literature. The results indicate a possible requirement of re-visiting cell balancing technique used by BMS [165-167]. Cell balancing is performed by taking account of cell voltage and is performed very fast (83-2000 Hz as reported by *Daowd et al.* [167] which could be several tens of kilohertz [168, 169]) with minimal relaxation period. As electrochemical process within the cell changes (thus the impedance) rapidly within short relaxation period, it is likely that cell voltage will be affected (fast change of cell voltage after a charge/discharge event is well known). Therefore, there is a possibility that cells are balanced with voltage which is changing rapidly, reducing performance of cell balancing system.

One conclusion was made that pure Ohmic resistance, R_o of the cell is independent of relaxation period for the timescales investigated; therefore, this can be used as an online measurement parameter. Recently *Raijmakers et al.* reported a technique to monitor cell temperature based on the frequency associated with R_o reading in Nyquist plot [55]. These types of measurements will therefore not be affected by relaxation of the cell. Also, the calculation of ageing using R_o of the EIS tests previously performed without considering relaxation period, as part of long duration ageing test is valid.

OCV is one of the key parameters of an ECM. An inaccuracy in OCV estimation within the BMS can be detrimental in many ways e.g. can lead to shift of operating SoC window of the battery pack, thus poses a safety risk. In this thesis it has been shown that OCV test procedures used by researchers to calculate cell OCV and thus hysteresis were erroneous due to lack of knowledge of defining the initial condition of the cell (0 % SoC) and change in cell capacity with test procedure. Also, limited research has been done with OCV hysteresis of different chemistry Li-ion cell, except LFP. In some instances researchers incorrectly assumed no hysteresis or a constant hysteresis across 0-100 % SoC [114, 117, 120]. A new OCV and OCV hysteresis test procedure is proposed in this thesis to acquire OCV and OCV hysteresis with better accuracy, reliability and repeatability. A measurable hysteresis was found for other cell chemistries in addition to LFP which has been shown to vary with SoC.

To measure a cell's OCV as a function of SoC researchers previously used a step OCV test procedure [115, 122-124]. Step OCV test is favoured over OCV test with low C rate (e.g. C/25). A low C rate such as C/25 captures some cell kinetic contributions and pure Ohmic resistance thus cannot truly be considered as an OCV. When cells are discharged in steps, depending on the step size, cell capacity varies, which has been shown in Table 10 in this thesis. This variation is due to the reduction of the electrode polarisation with smaller step size. When electrode polarisation is reduced, lithium can diffuse deeper into the electrode, enabling the electrode to accommodate more lithium ions, thus giving a higher capacity. The increase of capacity due to reduction in electrode polarisation is well known among researchers [92, 103], however never reported in conjunction with OCV tests. When

this capacity variation is not accounted for, while reporting OCV, an incorrect conclusion of OCV variation with step size of the OCV test procedure could be drawn, as shown in Figure 63. Although the capacity varies with step size, however when this capacity variation is addressed while analysing OCV data i.e. OCV is plotted versus capacity not SoC, use of different step sizes do not influence OCV measurement as shown in Figure 64 and Figure 65. Therefore, depending on the requirement OCV tests could be done with different step sizes if plotted against capacity, but not when plotted against SoC. For example, if high resolution of OCV curve is a requirement the test could be done with shorter step size (e.g. equivalent to 1 % SoC step), which will take a long time to complete as higher number of relaxation period needs to be allowed after each step. On the other hand, if a faster test duration is required, the test could be done with longer step size (e.g. equivalent to 10 % SoC step), which will have lower resolution. One interesting way of designing an OCV test could be use of variable step length. OCV of Li-ion cells have regions (see Figure 64) where OCV does not change much with capacity (e.g. 10 mV/Ah for LFP cell), and regions where change of OCV with capacity is high (e.g. 100 mV/Ah for LFP cell). Therefore, ideally lower resolution (longer step size) for flat regions and higher resolution (shorter step size) for sharp regions could be used for OCV test. Design of OCV test with variable step size has not been researched as part of this thesis; however it will be a natural extension.

The charge and discharge OCV measured via the proposed methodology, in Chapter 8, is in accordance with the theory of the origin of the OCV discussed in Section 2.3. This is in contrast to the previously published literature [124] which reported charge-discharge rate dependency of OCV. They suggested strong inhomogeneity among

the particles' lithium content contribute toward OCV variation with rate even after 8 hours of relaxation. However, according to the thermodynamic origin of OCV, at a particular temperature it is directly related to the proportion of active lithium within the electrodes [20, 170]. Therefore, when an adequate relaxation period is applied, OCV should be independent of charge-discharge rate. One possible reason of OCV variation with rate reported by Roscher *et al.* could be due to initial mismatch of SoC (there was no explanation how initial SoC was matched) from where cells were discharged (or charged) to reach target SoC. Therefore, even though SoC discharged or charged is same, due to initial mismatch the cell might not reach the target SoC. In contrast to the work by Roscher *et al.* results presented in this thesis shows OCV is independent of charge-discharge rates (0.2C, 1C and 3C) considered in this thesis. Therefore, when only work by Roscher *et al.* is considered, BMS require to incorporate immediate history of charge/discharge rate to calculate OCV. In contrast, this thesis confirms there is no requirement for considering previous charge discharge rate to calculate OCV. This is significant in two ways, firstly simplification of OCV estimation process (one less parameter to consider) and secondly accurate estimation of OCV.

A measurable hysteresis was found for other cell chemistries in addition to LFP which is known to vary with SoC. A certain level of OCV hysteresis in LFP cells has been reported in literature. However, The hysteresis of LFP cells was found to be 5-10 mV different compared to that of previously published results [119, 124, 171]. This might be due to the discrepancy in test procedure used previously (further explained in Chapter 8). A 5-10 mV inaccuracy in hysteresis is important because it will reduce OCV estimation accuracy by 5-10 mV which in turn will deteriorate

ECM performance and thus BMS operation. Despite the misleading assessment of hysteresis as shown in Figure 68 of this thesis, and hysteresis of load curves (charge-discharge voltage curve) as done by Bruce *et. al.* [39] and many other researchers, OCV hysteresis of other chemistry cells has been largely ignored. In Figure 70 and Figure 71 of this thesis it is reported that although LFP has highest level of hysteresis, other Li-ion cell chemistries also show a certain level of hysteresis which is lowest for the cells with LTO anode. Also, Figure 71 presented that the hysteresis voltage magnitude is not same over the entire capacity (SoC) range; it is highest for lower SoC. This new knowledge shows that hysteresis versus capacity (SoC) relationship should be used for OCV estimation, rather than assuming a fixed hysteresis value [119, 160].

A dynamic hysteresis model has been used in Section 8.3.3 to show how better OCV prediction accuracy can be achieved by a BMS when hysteresis versus capacity relationship is used. Previously for nickel metal hydride (NiMH) battery, *Verbrugge et al.* [172] shown better SoC estimation could be achieved when OCV hysteresis is taken into account in SoC estimation algorithm. Later *Hu et al.* [160] investigated 12 different types of models and proposed similar algorithm as proposed by *Verbrugge et al.* which includes hysteresis will be the best choice for LFP cells. Here in this thesis, Section 8.3.3 provides further evidence that BMS performance could be improved by using hysteresis versus capacity relationship, and importantly it is not limited to only LFP cells but also other Li-ion cell chemistries.

Furthermore, this thesis reported that hysteresis changes with temperature. A cell's OCV is a function of temperature due to the thermodynamic origin, as explained in

Section 2.3. Variation of charge and discharge OCV is not the same when temperature is lower or higher compared to room temperature, therefore hysteresis changes at low temperature, as shown in Figure 72. Although theory of the variation of OCV with temperature is known [20, 170], change of hysteresis with temperature has not been reported in the literature. This variation of hysteresis with temperature will add more complexity to the OCV estimation process as temperature of the battery needs to be taken in to account.

These contributions to knowledge will provide useful reference and guideline for both academic and industrial researchers. The results demonstrate improvement in accuracy and consistency could be achieved by modifying existing test procedures. Also it has been presented that different interpretation of the test data (e.g. OCV-capacity relationship instead of OCV-SoC) can lead to better estimation of vehicle performance and thus improve trust of the user/driver.

9.3 Future direction

1. The next logical extension of this work is to implement the linear relationship between total capacity in Watt-hours and average current of dynamic duty cycle reported in this thesis to estimate degradation of battery capacity and power capability. With ageing process, the battery capacity decreases and resistance increases [42, 43, 52, 59, 61]. Change in resistance causes the change of gradients of the plot shown in Figure 46 and Equation (22), and capacity reduction reflected as reduction of the value of the constant in Equation (22). Moreover, the relationship is validated at a single temperature

point (25 °C), which needs to be extended to the wide operating temperature range of EV.

2. This thesis proposed better estimation of RDR for duty cycle which was validated within a laboratory environment. However, this needs to be implemented within the BMS and validated in the real world. A comparison of real world performance with SoC will be a natural extension of this work before implementation in a commercial EV.

3. The spiral shape of Nyquist plots found in short-term EIS tests demands further attention. Further understanding of the electrochemical processes involved will reveal any profile of the change of this shape and enable removing inconsistency of the short timescale EIS results.

4. OCV hysteresis was found to be changing with temperature. Though the shape of hysteresis voltage vs SoC was similar, the amplitude of hysteresis voltage was increasing at lower temperatures. Further extension of this work with the operating temperature widow of an EV will reveal the relationship of hysteresis voltage vs temperature.

5. One natural extension of the work with capacity, EIS and OCV is to extend the work for aged cells. Although the electrochemical processes within Li-ion cells remain similar; however, with age, the extent of different electrochemical process changes and new electrochemical processes introduced (e.g. corrosion, cracking of pores). Therefore, validity and

applicability of the new knowledge presented within this thesis will need to be verified on aged cells. The increased knowledge and recommendations for modification of the standard tests allows ageing to be investigated in a more reproducible way.

10. Conclusions

In this chapter the overall conclusions of the research for capacity, OCV and EIS tests are reported. In the following paragraph, the gaps in literature followed by the proposed solutions with experimental evidence and finally contributions to knowledge are summarised.

The accurate estimation of the operation of a Li-ion battery pack within the automotive environment largely depends on battery management system (BMS) performance. Equivalent circuit models (ECM) are used by the BMS for its operation, which in turn are dependent on the characterisation test results. Characterisation tests such as capacity, OCV and EIS are of critical importance in defining performance of an ECM. EIS is commonly used to parameterise discrete components of an ECM. OCV test results define OCV, another key component of ECM. Capacity test results measure stored charge within the battery pack, equivalent to amount of gasoline in a fuel tank of an ICE vehicle. Test procedures for EIS, capacity and OCV tests exist. However, these test procedures were not designed specifically for automotive applications, e.g. do not reflect real world drive cycle of a vehicle. Therefore, when they were introduced to the automotive sector they were unable to provide adequate knowledge, accurately and repeatedly to the academic researchers and industrial design engineers. This is reflected by the reported deviation of the expected performance of the EVs introduced in recent years. This deviation of performance could be due to flaws e.g. inaccuracy and irreparability of test procedure or tests are unable to reflect real world operating conditions. In either way the test procedures require research attention. The research carried out as part of

this thesis reported how to improve consistency, accuracy and interpretation of characterisation test techniques for Li-ion battery cells for automotive application.

The existing capacity test procedure measure stored charge (Amp-hours). A vehicle is driven by the power transferred to the wheels, which is directly related to the stored energy, not only stored charge. It was demonstrated in this thesis that the measures of energy (Watt-hours) through capacity tests instead of the charge (Amp-hours) as per standard test are advantageous to provide accurate estimation of driving range of an EV.

The reported improvement of the capacity test methodology effectively includes the power de-rating technique and validation over drive cycle of the vehicle into the testing protocol. It is reported that through de-rating, battery capacity in Amp-hours can be maximised, however capacity in Watt-hours cannot. Irreversible loss of energy through Joule heating is identified as the main cause, which is not accounted in for the Amp-hours measure. The Joule heating increases with current amplitude, which reduces total Watt-hours of the pack linearly with the average current since the last full charge. Hence, two main contributions to knowledge reported in this thesis, related to the capacity testing are that capacity in Watt-hours is appropriate for automotive applications not Amp-hours, and total Watt-hours is linearly related to the average current of the duty cycle. These two contributions are validated for the actual drive cycle of a vehicle.

Despite previous extensive use of EIS to parameterise ECMs, ageing and electrode properties, for the first time this thesis reports that the time period between the

removal of an electrical load and an EIS measurement affects the results. Therefore, EIS results are not comparable when a standardised relaxation period is not applied, and ECM parameterisation becomes invalid when EIS test was performed before the cell reaches electrochemical equilibrium. The relaxation period is extended at lower temperature and after higher charge-discharge rate, however remains similar over the entire SoC. Two electrochemical processes, diffusion within the electrolyte and solid state diffusion of lithium within the bulk of materials are identified as the main cause of relaxation which changes at lower temperature and higher charge/discharge rate. It is concluded, based on the experiment of five commercially available cells, that the variation of EIS results falls within the experimental error after 4 hours of relaxation period, thus 4 hours can be used as standardised relaxation period.

In addition to ECM parameterisation, EIS has been considered for fast online measurement, integrated with a BMS. It is reported in this thesis that within a relaxation period of 0-10 min (which is in of importance for fast online measurement) the EIS result (Nyquist plot) shows a spiral shape which disappears after a maximum of 10min of relaxation. Due to this shape, the value of charge transfer resistance and capacitance become inconsistent. Before this research, there was no prior knowledge found in literature of this shape of EIS plot of Li-ion cells. It was concluded that the use of EIS as a fast online measurement technique is unreliable.

OCV is a fundamental parameter of ECM. OCV test procedures used previously do not consider the initial conditions of the cells and capacity variations that show a change in OCV, leading to an apparent increase in, or erroneous, hysteresis. A new

OCV and OCV hysteresis test methodology has been proposed to assess OCV and OCV hysteresis as part of this thesis. Using the proposed methodology, OCV and hysteresis voltage of different commercially available cells have been measured. The LFP cell showed the highest level of hysteresis and the NMC cell with LTO anode had the lowest level of hysteresis, although measurable. In general, maximum hysteresis was present at low SoC for all the cells tested. Before this research, there was no literature reporting OCV hysteresis of different chemistry cells and variation of hysteresis with SoC. The interaction of many particles with non-monotonic chemical potentials explains how hysteresis can occur in other Li-ion chemistries in addition to LFP. The proposed methodology will provide a guideline for OCV and OCV hysteresis characterisation for academic and industrial researchers. To consider an example, from the results obtained a dynamic hysteresis model has been evaluated. The inclusion of the hysteresis voltage as a function of SoC, rather than a constant, shows how the model predicts the empirically determined OCV characteristic more accurately. The results provide better understanding of SoC estimation of a Li-ion battery particularly for automotive applications.

Overall, the contributions of this thesis to the scientific community are:

- Better consistency through introducing a new parameter (e.g. relaxation period) into testing (EIS).
- Improved accuracy through including real world scenarios (e.g. current de-rating, drive cycle) into the test procedure (capacity test).
- Better interpretation of existing parameters (e.g. hysteresis as a function of SoC, not constant).

With the use of a case study to calculate OCV, it has been shown that these recommendations will improve performance of ECM, and thus not only EVs but also other Li-ion battery applications.

Reference

1. America's Climate Choices: Panel on Advancing the Science of Climate Change, National Research Council, *Advancing the Science of Climate Change*. 2010, USA: The National Academies Press.
2. Jakob, M. and J. Hilaire, *Climate science: Unburnable fossil-fuel reserves.* Nature, 2015. **517**(7533): p. 150-152.
3. McCarthy, J.E. and B.D. Yacobucci, *Cars, Trucks, and Climate: EPA Regulation of Greenhouse Gases from Mobile Sources*. 2014, Congressional Research Service
4. *Amending Regulation (EC) No 443/2009 to define the modalities for reaching the 2020 target to reduce CO2 emissions from new passenger cars*, in *Regulation (EU) No 333/2014*, The European Perlament and the Council of the European Union, Editor. 2014, Official Journal of the European Union.
5. *Corporate Average Fuel Economy for MY 2017-MY 2025 Passenger Cars and Light Trucks*. 2012, U.S. Department Of Transportation: Office of Regulatory Analysis and Evaluation, National Center for Statistics and Analysis.
6. Husain, I., *Electric and Hybrid Vehicles: Design Fundamentals*. 2 ed. 2011, New York: CRC Press.
7. Williams, J.L. *Oil price history and analysis*. WTRG Economics, May 2008; Available from: http://www.wtrg.com/prices.htm.
8. Trigg, T. and P. Telleen, *Global EV Outlook; Understanding the Electric Vehicle Landscape to 2020*. 2013, International Energy Agency.

9. Lukic, S.M., J. Cao, R.C. Bansal, F. Rodriguez, and A. Emadi, *Energy Storage Systems for Automotive Applications.* Industrial Electronics, IEEE Transactions on, 2008. **55**(6): p. 2258-2267.

10. Kalhammer, F.R., B.M. Kopf, D.H. Swan, V.P. Roan, and M.P. Walsh, *Status and Prospects for Zero Emissions Vehicle Technology*. 2007, State of California Air Resources Board: Sacramento, California.

11. *Directive 2006/66/Ec Of The European Parliament And Of The Council*, The European Parliament and The Council Of The European Union, 2006.

12. EDTA. *Electric drive vehicle sales figures (U.S. Market) - EV sales*. 2013 02/01/2014]; Available from: http://www.electricdrive.org/index.php?ht=d/sp/i/20952/pid/20952.

13. Hurst, D. and J. Gartner, *Global Forecasts for Light Duty Hybrid, Plug-in Hybrid and Battery Electric Vehicles: 2013-2020*. 2013.

14. Birrell, S.A., A. McGordon, and P.A. Jennings. *Defining the accuracy of real-world range estimations of an electric vehicle*. in *Intelligent Transportation Systems (ITSC), 2014 IEEE 17th International Conference on*. 2014.

15. *Real World Battery Capacity Loss*. 2015 [cited 22/07/2015]; Available from: http://www.electricvehiclewiki.com/Real_World_Battery_Capacity_Loss

16. Hyde, J. *GM recalling 8,000 Chevy Volts to prevent battery fires*. 2012 05 Jan 2012 [cited 2014 02 May 2014]; Available from: https://autos.yahoo.com/blogs/motoramic/gm-recalling-chevy-volts-prevent-battery-fires-164320241.html.

17. Smale, W. *Dreamliner: Boeing 'may never find battery fault cause'*. 2013 22 April 2013 [cited 2014 02 May 2015]; Available from: http://www.bbc.co.uk/news/business-22251756.

18. Blanco, S. *BYD e6 taxi catches fire in China after crash caused by drunk Nissan GT-R driver*. 2012 28 May 2012 [cited 2014 02 May 2015]; Available from: http://green.autoblog.com/2012/05/28/byd-e6-taxi-catches-fire-in-china-after-crash-caused-by-drunk-ni/.

19. EiG Ltd., *Product Specification for Rechargeable Lithium Ion Polymer Battery; Model : ePLB C020B*. 2009.

20. Linden, D. and T.B. Reddy, *Handbook of Batteries*. 3rd ed. 2002: McGraw-Hill.

21. U.S. Environmental Protection Agency, *Electronics Waste Management in the United States Through 2009*, Office of Resource Conservation and Recovery, Editor. 2011, U.S. Environmental Protection Agency.

22. *Plug-in car grant eligibility guidance*, U.S. Department for Transport, Editor. 2015, Office for Low Emission Vehicles, UK.

23. Energy, U.S.D.o., *Battery Test Manual for Plug In Hybrid Electric Vehicles*, V.T.P. Energy Efficiency and Renewable Energy, Editor. 2010: Idaho Operations Office.

24. Harold Haskins, V.B., Jon Christophersen, Ira Bloom, Gary Hunt, Ed Thomas, *Battery Technology Life Verification Test Manual*, U.S.D.o. Energy, Editor. 2005, Idaho National Laboratory, Transportation Technology Department: Idaho Falls, Idaho.

25. 12405-2:2012, B.I., *Electrically propelled road vehicles - Test specification for lithium-ion traction battery packs and systems; Part 2: High-energy applications*. 2012, British Standards Institution

26. 62660-1, I., *Secondary lithium-ion cells for the propulsion of electric road vehicles – Part 1: Performance testing*. 2012, International Electrotechnical Commission: Geneva, Switzerland.

27. ISO, *Electrically propelled road vehicles - Test specification for lithium-ion traction battery packs and systems*, in *Part 1: High-power applications*. 2011, International Organization for Standardization: Geneva, Switzerland.

28. Chung, J. and IEEE, *A Proposal for the IEEE EV LiB Cell Safety Standard.* 2013 International Conference on Connected Vehicles and Expo (Iccve), 2013: p. 437-442.

29. McDowall, J., *Integrating energy storage with wind power in weak electricity grids.* Journal of Power Sources, 2006. **162**(2): p. 959-964.

30. Scrosati, B. and J. Garche, *Lithium batteries: Status, prospects and future.* Journal of Power Sources, 2010. **195**(9): p. 2419-2430.

31. *Tesla Motors begins regular production of 2008 Tesla Roadster*. 2008, Tesla Motors.

32. *Production of 100% Electric, Zero-Emission Nissan LEAF begins at Oppama, Japan*. 2010, Nissan Motor Corporation.

33. Axsen, J., A. Burke, and K.S. Kurani, *Batteries for Plug-in Hybrid Electric Vehicles (PHEVs): Goals and the State of Technology circa 2008*. 2008, Institute of Transportation Studies: Davis, California.

34. Choi, S.S. and H.S. Lim, *Factors that affect cycle-life and possible degradation mechanisms of a Li-ion cell based on LiCoO2.* Journal of Power Sources, 2002. **111**(1): p. 130-136.

35. Wang, J., P. Liu, J. Hicks-Garner, E. Sherman, S. Soukiazian, M. Verbrugge, H. Tataria, J. Musser, and P. Finamore, *Cycle-life model for graphite-LiFePO4 cells.* Journal of Power Sources, 2011. **196**(8): p. 3942-3948.

36. Anderson, D.L., *An evaluation of current and future costs for lithium-ion batteries for use in electrified vehicle powertrains*, in *Nicholas School of the Environment*. 2009, Duke University. p. 44.

37. *Our guide to batteries*. 2012, Johnson Matthey Battery Systems.

38. Nishi, Y., *Lithium ion secondary batteries; past 10 years and the future.* Journal of Power Sources, 2001. **100**(1–2): p. 101-106.

39. G. Bruce, P., A. Robert Armstrong, and R. L. Gitzendanner, *New intercalation compounds for lithium batteries: layered LiMnO2.* Journal of Materials Chemistry, 1999. **9**(1): p. 193-198.

40. Zhang, D., B.S. Haran, A. Durairajan, R.E. White, Y. Podrazhansky, and B.N. Popov, *Studies on capacity fade of lithium-ion batteries.* Journal of Power Sources, 2000. **91**(2): p. 122-129.

41. Broussely, M., S. Herreyre, P. Biensan, P. Kasztejna, K. Nechev, and R.J. Staniewicz, *Aging mechanism in Li ion cells and calendar life predictions.* Journal of Power Sources, 2001. **97–98**(0): p. 13-21.

42. Broussely, M., P. Biensan, F. Bonhomme, P. Blanchard, S. Herreyre, K. Nechev, and R.J. Staniewicz, *Main aging mechanisms in Li ion batteries.* Journal of Power Sources, 2005. **146**(1–2): p. 90-96.

43. Vetter, J., P. Novák, M.R. Wagner, C. Veit, K.C. Möller, J.O. Besenhard, M. Winter, M. Wohlfahrt-Mehrens, C. Vogler, and A. Hammouche, *Ageing mechanisms in lithium-ion batteries.* Journal of Power Sources, 2005. **147**(1–2): p. 269-281.

44. Thackeray, M.M., C. Wolverton, and E.D. Isaacs, *Electrical energy storage for transportation-approaching the limits of, and going beyond, lithium-ion batteries.* Energy & Environmental Science, 2012. **5**(7): p. 7854-7863.

45. Ohzuku, T., A. Ueda, and N. Yamamoto, *Zero-Strain Insertion Material of Li[Li1/3Ti5/3]O4 for Rechargeable Lithium Cells.* Journal of The Electrochemical Society, 1995. **142**(5): p. 1431-1435.

46. Han, X.B., M.G. Ouyang, L.G. Lu, and J.Q. Li, *Cycle Life of Commercial Lithium-Ion Batteries with Lithium Titanium Oxide Anodes in Electric Vehicles.* Energies, 2014. **7**(8): p. 4895-4909.

47. Marcinek, M., J. Syzdek, M. Marczewski, M. Piszcz, L. Niedzicki, M. Kalita, A. Plewa-Marczewska, A. Bitner, P. Wieczorek, T. Trzeciak, M. Kasprzyk, P.Łężak, Z. Zukowska, A. Zalewska, and W. Wieczorek, *Electrolytes for Li-ion transport – Review.* Solid State Ionics, 2015. **276**: p. 107-126.

48. Arora, P. and Z. Zhang, *Battery Separators.* Chemical Reviews, 2004. **104**(10): p. 4419-4462.

49. Braithwaite, J.W., A. Gonzales, G. Nagasubramanian, S.J. Lucero, D.E. Peebles, J.A. Ohlhausen, and W.R. Cieslak, *Corrosion of Lithium-Ion Battery Current Collectors.* Journal of The Electrochemical Society, 1999. **146**(2): p. 448-456.

50. Pletcher, D., *A First Course in Electrode Processes*. 2009, Cambridge, UK: Royal Society of Chemistry.

51. Flandrois, S. and B. Simon, *Carbon materials for lithium-ion rechargeable batteries.* Carbon, 1999. **37**(2): p. 165-180.

52. Han, X., M. Ouyang, L. Lu, J. Li, Y. Zheng, and Z. Li, *A comparative study of commercial lithium ion battery cycle life in electrical vehicle: Aging mechanism identification.* Journal of Power Sources, 2014. **251**(0): p. 38-54.

53. Wu, M.-S., T.-L. Liao, Y.-Y. Wang, and C.-C. Wan, *Assessment of the Wettability of Porous Electrodes for Lithium-Ion Batteries.* Journal of Applied Electrochemistry, 2004. **34**(8): p. 797-805.

54. Thorat, I.V., D.E. Stephenson, N.A. Zacharias, K. Zaghib, J.N. Harb, and D.R. Wheeler, *Quantifying tortuosity in porous Li-ion battery materials.* Journal of Power Sources, 2009. **188**(2): p. 592-600.

55. Raijmakers, L.H.J., D.L. Danilov, J.P.M. van Lammeren, M.J.G. Lammers, and P.H.L. Notten, *Sensorless battery temperature measurements based on electrochemical impedance spectroscopy.* Journal of Power Sources, 2014. **247**(0): p. 539-544.

56. Bard, A.J. and L.R. Faulkner, *Electrochemical Methods*. 2nd ed. 2001: John Wiley & Sons, Inc.

57. Peled, E., *The Electrochemical Behavior of Alkali and Alkaline Earth Metals in Nonaqueous Battery Systems—The Solid Electrolyte Interphase Model.* Journal of The Electrochemical Society, 1979. **126**(12): p. 2047-2051.

58. Zhang, Y., C.-Y. Wang, and X. Tang, *Cycling degradation of an automotive LiFePO4 lithium-ion battery.* Journal of Power Sources, 2011. **196**(3): p. 1513-1520.

59. Wohlfahrt-Mehrens, M., C. Vogler, and J. Garche, *Aging mechanisms of lithium cathode materials.* Journal of Power Sources, 2004. **127**(1–2): p. 58-64.

60. Aurbach, D., E. Zinigrad, Y. Cohen, and H. Teller, *A short review of failure mechanisms of lithium metal and lithiated graphite anodes in liquid electrolyte solutions.* Solid State Ionics, 2002. **148**(3–4): p. 405-416.

61. Abraham, D.P., J. Liu, C.H. Chen, Y.E. Hyung, M. Stoll, N. Elsen, S. MacLaren, R. Twesten, R. Haasch, E. Sammann, I. Petrov, K. Amine, and G. Henriksen, *Diagnosis of power fade mechanisms in high-power lithium-ion cells.* Journal of Power Sources, 2003. **119–121**(0): p. 511-516.

62. Waag, W., S. Käbitz, and D.U. Sauer, *Experimental investigation of the lithium-ion battery impedance characteristic at various conditions and aging states and its influence on the application.* Applied Energy, 2013. **102**(0): p. 885-897.

63. Cho, E., J. Mun, O.B. Chae, O.M. Kwon, H.-T. Kim, J.H. Ryu, Y.G. Kim, and S.M. Oh, *Corrosion/passivation of aluminum current collector in bis(fluorosulfonyl)imide-based ionic liquid for lithium-ion batteries.* Electrochemistry Communications, 2012. **22**(0): p. 1-3.

64. Zhang, X., B. Winget, M. Doeff, J.W. Evans, and T.M. Devine, *Corrosion of Aluminum Current Collectors in Lithium-Ion Batteries with Electrolytes Containing LiPF6.* Journal of The Electrochemical Society, 2005. **152**(11): p. B448-B454.

65. GROOT, J., *State-of-Health Estimation of Li-ion Batteries: Cycle Life Test Methods*, in *Department of Energy and Environment*. 2012, Chalmers University Of Technology, Göteborg, Sweden.

66. Smart, M.C., B.V. Ratnakumar, J.F. Whitacre, L.D. Whitcanack, K.B. Chin, M.D. Rodriguez, D. Zhao, S.G. Greenbaum, and S. Surampudi, *Effect of Electrolyte Type upon the High-Temperature Resilience of Lithium-Ion Cells.* Journal of The Electrochemical Society, 2005. **152**(6): p. A1096-A1104.

67. Andersson, A.M., K. Edström, and J.O. Thomas, *Characterisation of the ambient and elevated temperature performance of a graphite electrode.* Journal of Power Sources, 1999. **81–82**(0): p. 8-12.

68. Ramadass, P., B. Haran, R. White, and B.N. Popov, *Capacity fade of Sony 18650 cells cycled at elevated temperatures: Part I. Cycling performance.* Journal of Power Sources, 2002. **112**(2): p. 606-613.

69. Huang, C.K., J.S. Sakamoto, J. Wolfenstine, and S. Surampudi, *The Limits of Low-Temperature Performance of Li-Ion Cells.* Journal of The Electrochemical Society, 2000. **147**(8): p. 2893-2896.

70. Zhang, S.S., K. Xu, and T.R. Jow, *Low temperature performance of graphite electrode in Li-ion cells.* Electrochimica Acta, 2002. **48**(3): p. 241-246.

71. Fan, J. and S. Tan, *Studies on Charging Lithium-Ion Cells at Low Temperatures.* Journal of The Electrochemical Society, 2006. **153**(6): p. A1081-A1092.

72. Savoye, F., P. Venet, M. Millet, and J. Groot, *Impact of Periodic Current Pulses on Li-Ion Battery Performance.* Industrial Electronics, IEEE Transactions on, 2012. **59**(9): p. 3481-3488.

73. Ji, Y., Y. Zhang, and C.-Y. Wang, *Li-Ion Cell Operation at Low Temperatures.* Journal of The Electrochemical Society, 2013. **160**(4): p. A636-A649.

74. Whittingham, M.S., *Inorganic nanomaterials for batteries.* Dalton Transactions, 2008(40): p. 5424-5431.

75. Nishizawa, M., R. Hashitani, T. Itoh, T. Matsue, and I. Uchida, *Measurements of Chemical Diffusion Coefficient of Lithium Ion in Graphitized Mesocarbon Microbeads Using a Microelectrode.* Electrochemical and Solid-State Letters, 1998. **1**(1): p. 10-12.

76. Gummow, R.J., A. de Kock, and M.M. Thackeray, *Improved capacity retention in rechargeable 4 V lithium/lithium-manganese oxide (spinel) cells.* Solid State Ionics, 1994. **69**(1): p. 59-67.

77. Chung, K.Y. and K.-B. Kim, *Investigations into capacity fading as a result of a Jahn–Teller distortion in 4 V LiMn2O4 thin film electrodes.* Electrochimica Acta, 2004. **49**(20): p. 3327-3337.

78. Cannarella, J. and C.B. Arnold, *Stress evolution and capacity fade in constrained lithium-ion pouch cells.* Journal of Power Sources, 2014. **245**(0): p. 745-751.

79. Peabody, C. and C.B. Arnold, *The role of mechanically induced separator creep in lithium-ion battery capacity fade.* Journal of Power Sources, 2011. **196**(19): p. 8147-8153.

80. Gomez, J., R. Nelson, E.E. Kalu, M.H. Weatherspoon, and J.P. Zheng, *Equivalent circuit model parameters of a high-power Li-ion battery: Thermal and state of charge effects.* Journal of Power Sources, 2011. **196**(10): p. 4826-4831.

81. Rodrigues, S., N. Munichandraiah, and A.K. Shukla, *AC impedance and state-of-charge analysis of a sealed lithium-ion rechargeable battery.* Journal of Solid State Electrochemistry, 1999. **3**(7-8): p. 397-405.

82. Sauvant-Moynot, V., J. Bernard, R. Mingant, A. Delaille, F. Mattera, S. Mailley, J.-L. Hognon, and F. Huet, *ALIDISSI, a Research Program to Evaluate Electrochemical Impedance Spectroscopy as a SoC and SoH Diagnosis Tool for Li-ion Batteries.* Oil Gas Sci. Technol. – Rev. IFP, 2010. **65**(1): p. 79-89.

83. Ecker, M., J.B. Gerschler, J. Vogel, S. Käbitz, F. Hust, P. Dechent, and D.U. Sauer, *Development of a lifetime prediction model for lithium-ion batteries based on extended accelerated aging test data.* Journal of Power Sources, 2012. **215**(0): p. 248-257.

84. Chan, H.L. and S. D. *A new battery model for use with battery energy storage systems and electric vehicles power systems*. in *Power Engineering Society Winter Meeting, 2000. IEEE*. 2000.

85. Andre, D., M. Meiler, K. Steiner, H. Walz, T. Soczka-Guth, and D.U. Sauer, *Characterization of high-power lithium-ion batteries by electrochemical impedance spectroscopy. II: Modelling.* Journal of Power Sources, 2011. **196**(12): p. 5349-5356.

86. Osaka, T., T. Momma, D. Mukoyama, and H. Nara, *Proposal of novel equivalent circuit for electrochemical impedance analysis of commercially available lithium ion battery.* Journal of Power Sources, 2012. **205**(0): p. 483-486.

87. Levi, M.D., G. Salitra, B. Markovsky, H. Teller, D. Aurbach, U. Heider, and L. Heider, *Solid-State Electrochemical Kinetics of Li-Ion Intercalation into $Li_{1-x}CoO_2$: Simultaneous Application of Electroanalytical Techniques SSCV, PITT, and EIS.* Journal of The Electrochemical Society, 1999. **146**(4): p. 1279-1289.

88. Schmidt, J.P., T. Chrobak, M. Ender, J. Illig, D. Klotz, and E. Ivers-Tiffée, *Studies on LiFePO4 as cathode material using impedance spectroscopy.* Journal of Power Sources, 2011. **196**(12): p. 5342-5348.

89. Momma, T., M. Matsunaga, D. Mukoyama, and T. Osaka, *Ac impedance analysis of lithium ion battery under temperature control.* Journal of Power Sources, 2012. **216**(0): p. 304-307.

90. Zhuang, Q.-C., T. Wei, L.-L. Du, Y.-L. Cui, L. Fang, and S.-G. Sun, *An Electrochemical Impedance Spectroscopic Study of the Electronic and Ionic Transport Properties of Spinel LiMn2O4.* The Journal of Physical Chemistry C, 2010. **114**(18): p. 8614-8621.

91. Barsoukov, E. and J.R. Macdonald, *Impedance Spectroscopy, Theory, Experiment, and Applications*. 2 ed. 2005, New Jersey: John Wiley & Sons.

92. Cho, H.-M., W.-S. Choi, J.-Y. Go, S.-E. Bae, and H.-C. Shin, *A study on time-dependent low temperature power performance of a lithium-ion battery.* Journal of Power Sources, 2012. **198**(0): p. 273-280.

93. Liao, L., P. Zuo, Y. Ma, X. Chen, Y. An, Y. Gao, and G. Yin, *Effects of temperature on charge/discharge behaviors of LiFePO4 cathode for Li-ion batteries.* Electrochimica Acta, 2012. **60**(0): p. 269-273.

94. Aurbach, D., B. Markovsky, M.D. Levi, E. Levi, A. Schechter, M. Moshkovich, and Y. Cohen, *New insights into the interactions between electrode materials and electrolyte solutions for advanced nonaqueous batteries.* Journal of Power Sources, 1999. **81–82**(0): p. 95-111.

95. Kassem, M., J. Bernard, R. Revel, S. Pélissier, F. Duclaud, and C. Delacourt, *Calendar aging of a graphite/LiFePO4 cell.* Journal of Power Sources, 2012. **208**(0): p. 296-305.

96. Bloom, I., B.W. Cole, J.J. Sohn, S.A. Jones, E.G. Polzin, V.S. Battaglia, G.L. Henriksen, C. Motloch, R. Richardson, T. Unkelhaeuser, D. Ingersoll, and H.L. Case, *An accelerated calendar and cycle life study of Li-ion cells.* Journal of Power Sources, 2001. **101**(2): p. 238-247.

97. SAC, *Cycle Life requirements and test methods of traction battery for electric vehicles*. 2012, Standardization Administration of China: China.

98. Ning, G., B. Haran, and B.N. Popov, *Capacity fade study of lithium-ion batteries cycled at high discharge rates.* Journal of Power Sources, 2003. **117**(1–2): p. 160-169.

99. Zhang, Y. and C.-Y. Wang, *Cycle-Life Characterization of Automotive Lithium-Ion Batteries with LiNiO2 Cathode.* Journal of The Electrochemical Society, 2009. **156**(7): p. A527-A535.

100. Zhang, Q., Q. Guo, and R.E. White, *A New Kinetic Equation for Intercalation Electrodes*. Journal of The Electrochemical Society, 2006. **153**(2): p. A301-A309.

101. IEC, *Secondary lithium-ion cells for the propulsion of electric road vehicles – Part 2: Reliability and abuse testing*. 2010, International Electrotechnical Commission: Geneva, Switzerland.

102. Energy, U.S.D.o., *Battery Test Manual for Plug In Hybrid Electric Vehicles*, V.T.P. Energy Efficiency and Renewable Energy, Editor. 2014: Idaho Operations Office.

103. Braun, P.V., J. Cho, J.H. Pikul, W.P. King, and H. Zhang, *High power rechargeable batteries.* Current Opinion in Solid State and Materials Science, 2012. **16**(4): p. 186-198.

104. Eddahech, A., O. Briat, N. Bertrand, J.-Y. Delétage, and J.-M. Vinassa, *Behavior and state-of-health monitoring of Li-ion batteries using impedance spectroscopy and recurrent neural networks.* International Journal of Electrical Power & Energy Systems, 2012. **42**(1): p. 487-494.

105. Choi, Y.-M. and S.-I. Pyun, *Effects of intercalation-induced stress on lithium transport through porous LiCoO2 electrode.* Solid State Ionics, 1997. **99**(3–4): p. 173-183.

106. Arora, P., B.N. Popov, and R.E. White, *Electrochemical Investigations of Cobalt-Doped $LiMn_2O_4$ as Cathode Material for Lithium-Ion Batteries.* Journal of The Electrochemical Society, 1998. **145**(3): p. 807-815.

107. Barsoukov, E., J.H. Kim, D.H. Kim, C.O. Yoon, and H. Lee, *Parametric analysis using impedance spectroscopy: relationship between material properties and battery performance.* Journal of New Materials for Electrochemical Systems, 2000. **3**: p. 303-310.

108. Kochowski, S. and K. Nitsch, *Description of the frequency behaviour of metal–SiO2–GaAs structure characteristics by electrical equivalent circuit with constant phase element.* Thin Solid Films, 2002. **415**(1–2): p. 133-137.

109. Seki, S., N. Kihira, Y. Mita, T. Kobayashi, K. Takei, T. Ikeya, H. Miyashiro, and N. Terada, *AC Impedance Study of High-Power Lithium-Ion Secondary Batteries—Effect of Battery Size.* Journal of The Electrochemical Society, 2011. **158**(2): p. A163-A166.

110. Zhang, Q. and R.E. White, *Calendar life study of Li-ion pouch cells.* Journal of Power Sources, 2007. **173**(2): p. 990-997.

111. Cho, H.-M., Y.J. Park, and H.-C. Shin, *Semiempirical Analysis of Time-Dependent Elementary Polarizations in Electrochemical Cells.* Journal of The Electrochemical Society, 2010. **157**(1): p. A8-A18.

112. Abraham, D.P., E.M. Reynolds, P.L. Schultz, A.N. Jansen, and D.W. Dees, *Temperature Dependence of Capacity and Impedance Data from Fresh and Aged High-Power Lithium-Ion Cells.* Journal of The Electrochemical Society, 2006. **153**(8): p. A1610-A1616.

113. Jensen, S.H., K. Engelbrecht, and C. Bernuy-Lopez, *Measurements of Electric Performance and Impedance of a 75 Ah NMC Lithium Battery Module.* Journal of The Electrochemical Society, 2012. **159**(6): p. A791-A797.

114. Huria, T., G. Ludovici, and G. Lutzemberger, *State of charge estimation of high power lithium iron phosphate cells.* Journal of Power Sources, 2014. **249**(0): p. 92-102.

115. Petzl, M. and M.A. Danzer, *Advancements in OCV Measurement and Analysis for Lithium-Ion Batteries.* Energy Conversion, IEEE Transactions on, 2013. **28**(3): p. 675-681.

116. Balasingam, B., G.V. Avvari, B. Pattipati, K.R. Pattipati, and Y. Bar-Shalom, *A robust approach to battery fuel gauging, part II: Real time capacity estimation.* Journal of Power Sources, 2014. **269**(0): p. 949-961.

117. Pattipati, B., B. Balasingam, G.V. Avvari, K.R. Pattipati, and Y. Bar-Shalom, *Open circuit voltage characterization of lithium-ion batteries.* Journal of Power Sources, 2014. **269**(0): p. 317-333.

118. Truchot, C., M. Dubarry, and B.Y. Liaw, *State-of-charge estimation and uncertainty for lithium-ion battery strings.* Applied Energy, 2014. **119**(0): p. 218-227.

119. Plett, G.L., *Extended Kalman filtering for battery management systems of LiPB-based HEV battery packs: Part 2. Modeling and identification.* Journal of Power Sources, 2004. **134**(2): p. 262-276.

120. Xing, Y., W. He, M. Pecht, and K.L. Tsui, *State of charge estimation of lithium-ion batteries using the open-circuit voltage at various ambient temperatures.* Applied Energy, 2014. **113**(0): p. 106-115.

121. Srinivasan, V. and J. Newman, *Existence of Path-Dependence in the LiFePO4 Electrode.* Electrochemical and Solid-State Letters, 2006. **9**(3): p. A110-A114.

122. Lu, L., X. Han, J. Li, J. Hua, and M. Ouyang, *A review on the key issues for lithium-ion battery management in electric vehicles.* Journal of Power Sources, 2013. **226**(0): p. 272-288.

123. Jonghoon, K., S. Gab-Su, C. Changyoon, C. Bo-Hyung, and L. Seongjun. *OCV hysteresis effect-based SOC estimation in extended Kalman filter algorithm for a LiFePO<inf>4</inf>/C cell*. in *Electric Vehicle Conference (IEVC), 2012 IEEE International*. 2012.

124. Roscher, M.A., O. Bohlen, and J. Vetter, *OCV Hysteresis in Li-Ion Batteries including Two-Phase Transition Materials.* International Journal of Electrochemistry, 2011. **2011**.

125. Fleckenstein, M., O. Bohlen, M.A. Roscher, and B. Bäker, *Current density and state of charge inhomogeneities in Li-ion battery cells with LiFePO4 as*

cathode material due to temperature gradients. Journal of Power Sources, 2011. **196**(10): p. 4769-4778.

126. Srinivasan, V., J.W. Weidner, and J. Newman, *Hysteresis during Cycling of Nickel Hydroxide Active Material.* Journal of The Electrochemical Society, 2001. **148**(9): p. A969-A980.

127. Dreyer, W., J. Jamnik, C. Guhlke, R. Huth, J. Moskon, and M. Gaberscek, *The thermodynamic origin of hysteresis in insertion batteries.* Nat Mater, 2010. **9**(5): p. 448-453.

128. Zhang, Y., W. Wang, Y. Kobayashi, and K. Shirai. *Remaining driving range estimation of electric vehicle*. in *Electric Vehicle Conference (IEVC), 2012 IEEE International*. 2012. IEEE.

129. Williams, T. *Real World Test: 2013 Nissan LEAF Range vs 2012 Nissan LEAF Range (w/Viideo).* 2013 01/06/2015]; Available from: http://insideevs.com/real-world-test-2013-nissan-leaf-range-vs-2012-nissan-leaf-range/.

130. Gordon-Bloomfield, N. *StaffCar Update: After 73,100 Miles, Our Nissan LEAF Loses its Second Capacity Bar*. 2015 01/06/2015]; Available from: https://transportevolved.com/2015/04/14/staffcar-update-after-73100-miles-our-nissan-leaf-loses-its-second-capacity-bar/.

131. Anritsu, *Battery Performance Test Solution for AT&T IOT*. 2009, www.anritsu.com.

132. Krein, P.T. *Battery Management for Maximum Performance in Plug-In Electric and Hybrid Vehicles*. in *Vehicle Power and Propulsion Conference, 2007. VPPC 2007. IEEE*. 2007.

133. Nyman, A., T.G. Zavalis, R. Elger, M. Behm, and G. Lindbergh, *Analysis of the Polarization in a Li-Ion Battery Cell by Numerical Simulations.* Journal of The Electrochemical Society, 2010. **157**(11): p. A1236-A1246.

134. Culcua, H., B. Verbruggeb, N. Omara, P.V.D. Bosscheb, and J.V. Mierloa, *Internal resistance of cells of lithium battery modules with FreedomCAR model*, in *EVS24*. 2009: Stavanger, Norway.

135. Kindermann, F., A. Noel, P. Keil, and A. Jossen. *Influence of Relaxation Time on EIS Measurements of Li-ion Batteries*. in *International Workshop on Impedance Spectroscopy*. 2013. Chemnitz, Germany.

136. Warner, J., *7 - Lithium-Ion Battery Packs for EVs,* in *Lithium-Ion Batteries*, G. Pistoia, Editor. 2014, Elsevier: Amsterdam. p. 127-150.

137. Gallagher, K.G. and P.A. Nelson, *6 - Manufacturing Costs of Batteries for Electric Vehicles*, in *Lithium-Ion Batteries*, G. Pistoia, Editor. 2014, Elsevier: Amsterdam. p. 97-126.

138. Tang, X., X. Mao, J. Lin, and B. Koch, *Li-ion Battery Parameter Estimation for State of Charge*, in *American Control Conference*. 2011: San Francisco, CA, USA.

139. Piller, S., M. Perrin, and A. Jossen, *Methods for state-of-charge determination and their applications.* Journal of Power Sources, 2001. **96**(1): p. 113-120.

140. Pop, V., H.J. Bergveld, P.H.L. Notten, and P.P.L. Regtien, *State-of-the-art of battery state-of-charge determination.* Measurement Science and Technology, 2005. **16**(12): p. R93.

141. Nenadic, N.G., H.E. Bussey, P.A. Ardis, and M.G. Thurston, *Estimation of State-of-Charge and Capacity of Used Lithium-Ion Cells.* International Journal of Prognostics and Health Management, 2014. **5 (2) 011**: p. 12.

142. Chau, K.T., K.C. Wu, and C.C. Chan, *A new battery capacity indicator for lithium-ion battery powered electric vehicles using adaptive neuro-fuzzy inference system.* Energy Conversion and Management, 2004. **45**(11–12): p. 1681-1692.

143. Crowell, J., *Power controller for managing arrays of smart battery packs*. 2005, Google Patents.

144. Farrington, R. and J. Rugh. *Impact of vehicle air-conditioning on fuel economy, tailpipe emissions, and electric vehicle range*. in *Earth Technologies Forum*. 2000. Washington, D.C.

145. Boriboonsomsin, K. and M. Barth, *Impacts of road grade on fuel consumption and carbon dioxide emissions evidenced by use of advanced navigation systems.* Transportation Research Record: Journal of the Transportation Research Board, 2009. **2139**(1): p. 21-30.

146. Rodgers, L., D. Frey, and E. Wilhelm. *Estimating an Electric Vehicle's "Distance to Empty" Using Both Past and Future Route Information*. in *ASME 2013 International Design Engineering Technical Conferences and Computers and Information in Engineering Conference*. 2013. American Society of Mechanical Engineers.

147. Oguchi, T. and M. Katakura, *New conceptual evaluation method of amount of exhaust emission gas on vehicular road traffic*, in *Sixth International Conference on Urban Transport and the Environment for the 21st Century*. 2000: Cambridge University, Cambridge, UK.

148. Wang, Y., C. Zhang, and Z. Chen, *A method for joint estimation of state-of-charge and available energy of LiFePO4 batteries.* Applied Energy, 2014. **135**(0): p. 81-87.

149. Liu, X., J. Wu, C. Zhang, and Z. Chen, *A method for state of energy estimation of lithium-ion batteries at dynamic currents and temperatures.* Journal of Power Sources, 2014. **270**(0): p. 151-157.

150. Barai, A., G.H. Chouchelamane, Y. Guo, A. McGordon, and P. Jennings, *A study on the impact of lithium-ion cell relaxation on electrochemical impedance spectroscopy.* Journal of Power Sources, 2015. **280**(0): p. 74-80.

151. Taylor, J., R. Ball, A. McGordon, K. Uddin, and J. Marco, *Sizing tool for rapid optimisation of pack configuration at early-stage automotive product development*, in *EVS28*. 2015: KINTEX, Goyang, Korea.

152. Gillespey, B.J., *Electric Vehicle State of Charge Indicator Integrated With Exterior Lamps*. 2014, Google Patents.

153. Frey, P.D.W., M.F. Eberhard, S.I. Kohn, M.S. Smith, and D.F. Lyons, *Charge state indicator for an electric vehicle*. 2012, Google Patents.

154. Bergveld, H.J., W.S. Kruijt, and P.H. Notten, *Battery management systems*. 2002: Springer.

155. Uddin, K., A. Picarelli, C. Lyness, N. Taylor, and J. Marco, *Acausal electro-thermal Li-ion battery models for automotive applications.* Energies, 2014. **7**(9): p. 5675-5700.

156. Barai, A., W.D. Widanalage, J. Marco, A. McGordon, and P. Jennings, *A study of the open circuit voltage characterization technique and hysteresis assessment of lithium-ion cells.* Journal of Power Sources (accepted), 2015.

157. Fuller, T.F., M. Doyle, and J. Newman, *Relaxation Phenomena in Lithium-Ion-Insertion Cells.* Journal of The Electrochemical Society, 1994. **141**(4): p. 982-990.

158. Kindermann, F.M., A. Noel, S.V. Erhard, and A. Jossen, *Long-term equalization effects in Li-ion batteries due to local state of charge inhomogeneities and their impact on impedance measurements.* Electrochimica Acta, 2015. **185**: p. 107-116.

159. Smith, K. and C.-Y. Wang, *Solid-state diffusion limitations on pulse operation of a lithium ion cell for hybrid electric vehicles.* Journal of Power Sources, 2006. **161**(1): p. 628-639.

160. Hu, X., S. Li, and H. Peng, *A comparative study of equivalent circuit models for Li-ion batteries.* Journal of Power Sources, 2012. **198**(0): p. 359-367.

161. Rahimi-Eichi, H. and M.-Y. Chow, *Big-Data Framework for Electric Vehicle Range Estimation*, in *40th Annual Conference of the IEEE Industrial Electronics Society*. 2014: Dallas, Texas.

162. Plett, G.L., *Extended Kalman filtering for battery management systems of LiPB-based HEV battery packs: Part 1. Background.* Journal of Power Sources, 2004. **134**(2): p. 252-261.

163. Rajan, B.V.P., *Plug in Hybrid Electric Vehicle Energy Management System for Real World Driving*, in *WMG*. 2014, University of Warwick.

164. Voelcker, J. *What Happens When the 2011 Nissan Leaf Battery Pack Runs Low?* 2010 30/05/2015]; Available from: http://www.greencarreports.com/news/1050685_what-happens-when-the-2011-nissan-leaf-battery-pack-runs-low.

165. Moore, S.W. and P.J. Schneider, *A review of cell equalization methods for lithium ion and lithium polymer battery systems*. 2001, SAE Technical Paper.

166. Barsukov, Y. and J. Qian, *Battery Power Management for Portable Devices*. 2013: Artech House.

167. Daowd, M., M. Antoine, N. Omar, P. Lataire, P. Van Den Bossche, and J. Van Mierlo, *Battery Management System—Balancing Modularization Based on a Single Switched Capacitor and Bi-Directional DC/DC Converter with the Auxiliary Battery*. Energies, 2014. **7**(5): p. 2897.

168. Lee, Y.-S. and C. Ming-Wang, *Intelligent control battery equalization for series connected lithium-ion battery strings.* Industrial Electronics, IEEE Transactions on, 2005. **52**(5): p. 1297-1307.

169. Uno, M. and K. Tanaka, *Influence of High-Frequency Charge-Discharge Cycling Induced by Cell Voltage Equalizers on the Life Performance of Lithium-Ion Cells.* Vehicular Technology, IEEE Transactions on, 2011. **60**(4): p. 1505-1515.

170. Nazri, G.A. and G. Pistoia, *Lithium Batteries Science and Technology*. 2003: Kluwer Academic, Dordrecht.

171. Pop, V., H.J. Bergveld, J.H.G. Op het Veld, P.P.L. Regtien, D. Danilov, and P.H.L. Notten, *Modeling Battery Behavior for Accurate State-of-Charge Indication.* Journal of The Electrochemical Society, 2006. **153**(11): p. A2013-A2022.

172. Verbrugge, M. and E. Tate, *Adaptive state of charge algorithm for nickel metal hydride batteries including hysteresis phenomena.* Journal of Power Sources, 2004. **126**(1–2): p. 236-249.